Electrical Engineering

Suhas Bhandare

Application of Lithium Niobate-based Integrated Optical Circuits to Optical Communication

PH.D. Dissertation

Paderborn, December 2003

DISSERTATION

ON

Application of Lithium Niobate-based Integrated Optical Circuits to Optical Communication

SUBMITTED IN PARTIAL FULFILLMENT OF THE
REQUIREMENTS FOR THE DEGREE OF
DOCTOR OF PHILOSOPHY
IN ELECTRICAL ENGINEERING
(DOKTOR-INGENIEUR)

TO

DEPARTMENT OF ELECTRICAL ENGINEERING
UNIVERSITY OF PADERBORN
WARBURGER STR. 100, 33098 PADERBORN
GERMANY

BY

M.Sc., M.Phil. Suhas Bhandare
from Pune, INDIA

Reviewers:
1. Prof. Dr. Reinhold Noè
2. Prof. Dr. Wolfgang Sohler

Date of Thesis Submission: June 10, 2003
Date of Defense Examination: December 3, 2003

Paderborn, December 2003
Diss. 14–196

Dedicated
To
My Parents,
My wife Kranti, and
My dearest kids Mrunmayi and Saumitra

Contents

List of Publications

(1) S. Bhandare and R. Noé, "Optimization of TE–TM Mode Converters on X–Cut, Y–Propagation $LiNbO_3$ used for PMD Compensation", *Proc. ECIO'01* Paderborn, Germany (2001), 172–174.

(2) D. Sandel, S. Bhandare, R. Noé, "Reciprocal Circular Birefringence in X–Cut, Z–Propagation $LiNbO_3$ Polarization Transformers", *Proc. ECIO'01* Paderborn, Germany, (2001), 193–196.

(3) S. Bhandare and R. Noé, "Optimization of TE–TM Mode Converters on X–Cut, Y–Propagation $LiNbO_3$ used for PMD Compensation", *J. Appl. Phys. B: Lasers and Optics* (Special Issue on Integrated Optics) **73** (2001), 481–483.

(4) S. Bhandare, R. Noé, and D. Sandel, "Origin of Reciprocal Circular Birefringence in X–Cut, Z–Propagation $LiNbO_3$ Polarization Transformers", *J. Appl. Phys. B: Lasers and Optics* (Special Issue on Integrated Optics) **73** (2001), 549–553.

(5) S. Bhandare, D. Sandel, R. Noè, H. Hermann, H. Suche, and W. Sohler, "Measurement of Differential Group Delay Profiles in Fibers and $LiNbO_3$ Distributed PMD Compensator", *Tech. Dig.: Symposium on Optical Fiber Measurements* NIST (Boulder) Colorado, USA (2002), 209–212.

(6) D. Sandel, V. Mirvoda, S. Bhandare, F. Wüst, and R. Noè, "Some Enabling Techniques for Polarization Mode Dispersion Compensation", *IEEE J. of Light. Technol.*, **21** (2003), 1198-1210.

(7) S. Bhandare, D. Sandel, R. Noè, R. Ricken, H. Suche, and W. Sohler, "$LiNbO_3$–based Integrated Optical Network Analyzer for Vectorial Structure Characterization of Fiber Bragg Gratings", *Proc. Int. Conf. on Fiber Optics and Photonics* Mumbai, India (2002), 97.

(8) S. Bhandare and R. Noé, "Pushing Distributed PMD Compensator Performance Towards Highest Bit Rates Using Lithium–Niobate–Tantalate or Lithium Tantalate Crystals", *Proc. ECIO'03* Prague, CZ (2003), 91–94.

(9) S. Bhandare, D. Sandel, R. Noè, R. Ricken, H. Suche, and W. Sohler, "$LiNbO_3$–based Integrated Optical Network Analyzer for Vectorial Structure Characterization of Fiber Bragg Gratings", *IEE Proc.: Circuits, Devices, and Systems* (Special Issue on Fiber Optics and Photonics) **150** (2003), 490–494.

ABSTRACT

A lithium niobate-based, integrated optical network analyzer for the vectorial structure characterization of optical fiber Bragg gratings is reported. Frequency-dependent complex reflectance Jones matrix is measured by interferometry and transformed into time domain. From the impulse response matrix, the vectorial grating structure is determined by inverse scattering. Local dichroic reflectivity and birefringence are derived from this data. Knowledge of the vectorial nature of the refractive index modulation depth and phase should allow an improvement of the ultra-violet (UV) light illumination process and to effectively correct the phase mask stitch errors by longitudinally selective UV light post-processing, in order to fabricate chirped and/or apodized gratings which require the highest fabrication accuracy.

Especially, for vectorial structure characterization, integrated optical circuit based on X-cut, Z-propagation lithium niobate was proposed and developed in-house. It consists of a single-mode 1x2 optical power splitter and is integrated with a set of 3 TE-pass polarizers, a set of 2 phase shifters, and a TE-TM mode converter on each arm of the power splitter. Topological details of this integrated optical circuit are given in the dissertation. This integrated optical circuit along with a 3x3 fiber coupler forms a Mach-Zehnder interferometer. A 3x3 fiber coupler with three photodiodes at its output was chosen because it allows the most accurate phase measurement. Real and imaginary parts of the frequency-dependent complex reflection coefficient are calculated from two linear combinations of three (three-phase) photocurrents. The integrated optic phase shifters allow digital phase shifting and perform AC rather than DC measurement in order to increase sensitivity. On-chip TE-pass polarizers maintain a reference polarization and ensure that only phase-modulated light with a single polarization enters the mode converter sections of this integrated optical circuit. The integrated optical TE-TM mode converters act as calibrated polarization transformers and are used to generate the required polarizations for vectorial measurement. The reflecting devices under test are connected to the measurement interferometer by means of an additional coupler. Measurement setup also includes a wavelength meter for frequency correction. A cleaved bare fiber end has a small reflectivity, which is independent of the frequency and polarization, is used for calibrating the measurement setup. A uniform optical fiber Bragg grating at 1548.25 nm with a reflectivity $> 95\%$ and a 0.2 nm bandwidth was characterized. From this the vectorial grating structure was obtained and these results are summarized in the dissertation.

TE–TM mode converters with endlessly adjustable coupling phases on the X-cut, Y-propagation lithium niobate are optimized by simulation studies for the highest electrooptic efficiency for distributed PMD compensation. Two-phase and three-phase TE–TM mode converters are compared, and the latter are found to have a slightly better electrooptic efficiency. If just a little differential group delay needs to be compensated then the compensation performance can be drastically improved if the compensator is realized in mixed ferroelectric crystals like lithium–niobate–tantalate where the birefringence can be tuned by varying the Ta content y in $LiNb_{1-y}Ta_yO_3$. A Ta content y of up to 0.5 is good to realize a PMD compensator for about 160 Gbit/s. This solution is particularly advisable at data

rates of 40 Gbit/s and beyond. The above in-house developed integrated optical network analyzer is also used to measure the frequency-dependent reduced Müller matrix of this in-house developed distributed PMD compensator. Such a reduced Müller matrix measurement allows to calculate the corresponding Jones matrix and hence the impulse response of the devices with polarization mode dispersion. From the latter, differential group delay profiles are determined by the inverse scattering technique. Some interesting DGD profiles are obtained and are summarized in the dissertation.

Chapter 1

Introduction

1.1 Background

The history of integrated optics began in 1969 with the paper published in Bell Systems Technical Journal [1] where S. E. Miller discussed the dream of Integrated Optical Circuits (IOC's) which would use photons instead of electrons. Today's high-speed electronics is possible due to technological advances in integrating several electronic components on to monolithic substrates in an IC form. Similarly, the future of optics could be seen in an integration of bulky optical components into complicated planner circuits which could perform various optical functions.

As in the optical fibers, light guiding in integrated optical waveguides is based on the phenomenon of total internal reflection. Light is confined to an area of high refractive index, which acts as *core*, with respect to its surroundings, called as *clad*. The integrated optics has not only the potential of generation, manipulation, and detection of optical waves but also has the capability to couple optical waves into and out of the integrated optical circuit's [2, 3].

The IOC's offers many significant advantages over their bulk optical counterparts, since their features are based on guided wave optics. There main advantages are as follows:

(1) Compact and light weight
(2) Stable alignment by integration
(3) Low operating voltages and short interaction lengths
(4) Easy control of guided waves
(5) High-speed operation
(6) Inherent parallel processing capability

The IOC's, in principle, consist of optical waveguides and waveguide-based devices. Passive optical devices includes optical power splitters and combiners [4], polarizers, wavelength division multiplexers and demultiplexers are developed for passive optical networks. The IOC's which could modulate the most important properties of light such as intensity, phase, polarization, and frequency are realized and are commercially available today as

intensity, phase, and polarization modulators, switches, and wavelength converters which utilizes either electrooptic or acoustooptic or thermooptic or nonlinear optic effects. The optically active IOC's such as waveguide amplifiers, lasers, and even the optical parametric oscillators have also been demonstrated very recently [5].

The materials used for realizing IOC's should have very low propagation losses at the operating wavelengths. Many kind of materials and the device fabrication techniques have been tried for realizing the integrated optical waveguides. The most important techniques include thin film deposition, ion exchange, thermal diffusion, ion implantation, and the epitaxial growth. The materials are chosen depending on whether the device is active or passive. If it is active then it further depends on which effect the device is based on. Based on design objectives, the material is chosen and, then, the most appropriate technique based on the waveguide specifications is selected for fabrication.

The principle materials for integrated optics are glass, lithium niobate, and gallium-arsenide. For glass based devices, ion exchange is the low cost technology. Ti in-diffusion is the most promising but expensive technology for lithium niobate based devices (a crystal with high electro-optic coefficients), while MBE and MOCVD is rather the most expensive technology for the devices which are based on gallium arsenide. The Table 1.1 summarizes the propagation losses and technology used for these three material systems.

Table 1.1: Materials for integrated optics

Material	Glass	Lithium Niobate	Gallium Arsenide
Technology	Ion-exchange CVD	Ti-Indiffusion Proton exchange	MBE MOCVD
Loss (dB/cm)	0.01	0.1	1

1.2 Motivation

The main objective of this entire work is to demonstrate the ability of the lithium niobate based integrated optical circuits to integrate very basic integrated optical components such as optical power splitters, polarizers, phase shifters, TE–TM mode converters etc. into one complex circuit which provides more functionality for optical instrumentation and latter, their applications to optical communication. Two different application of the lithium niobate-based integrated optical circuits that are demonstrated in this dissertation includes:

(1) An integrated optical network analyzer in X–cut, Z–propagation lithium niobate for vectorial structure characterization of optical fiber Bragg gratings

(2) An integrated optical polarization mode dispersion compensator in X–cut, Y–propagation lithium niobate for the polarization mode dispersion (PMD) compensation at 40 Gbit/s and beyond

1.2.1 An Integrated Optical Network Analyzer

Both microwave and optical networks are similar and consist of an assembly of components which are interconnected using waveguides, and, the signals are very narrowband quasi-monochromatic electromagnetic fields. Many microwave components have optical analogs and the list is growing every year. The most striking differences between them are that:

(1) there are only square-law detectors, i.e. the photodiodes
(2) the optical networks offer bandwidths orders of magnitude higher than the microwave networks
(3) the optical sources may have non-negligible linewidths which influences the measurement contrast
(4) the optical waveguides are dielectric in nature
(5) there are linear and nonlinear field-matter interactions such as *Rayleigh* and *Brillouin* scattering
(6) the common "single-mode" optical waveguides are in fact two-moded

In Table 1.2, the frequencies of the most popular bands used for optical network applications are listed.

Table 1.2: The frequencies of the optical carriers in three most popular optical bands

Wavelength (μm)	Frequency (THz)
0.85	353
1.31	229
1.55	194

The linewidths of several common optical sources are listed in Table 1.3 because this influences the signal-to-noise ratio.

Table 1.3: The linewidths and the coherence lengths of optical sources that are used in the optical network applications

Type of Source	Linewidth	Coherence Length
Light emitting diode	~ 20 THz	~ 15 μm
Superluminescent diode	~ 4 THz	~ 75 μm
Single mode laser diode	~ 1 GHz	~ 30 cm
Distributed feedback laser diode	~ 50 MHz	~ 6 m
External cavity laser diode	~ 50 KHz	~ 6 km

As has been mentioned in the above differences that the two propagating modes that the single-mode optical waveguide supports are nearly degenerate and differ mainly by their polarization. Most optical components are sensitive to the state of polarization, and, therefore, a full account of its evolution is very much essential in optical network analyses [6]. This implies that the optical network algebra is a matrix algebra. In particular, the transfer

function in optics becomes a transfer matrix, and the product of such transfer matrices is in general noncommutative.

We understand optical network analysis to be direct analogon of the electrical network analysis, which means that optical field transfer functions could be measured directly. It is suitable for characterizing the linear and time independent optical components such as Bragg gratings in fibers.

Fiber Bragg gratings are comparatively simple devices and in their most basic form consist of a periodic modulation of the index of refraction along the fiber core [7, 8]. There are various types of fiber Bragg gratings that differ by application and hence by refractive index modulation. Of great interest are chirped gratings for dispersion compensation which require the highest fabrication accuracy [9]. For polarization insensitive operation not only the desired refractive index modulation must be met precisely but the grating must also be free from birefringence and dichroism. The fabrication process has, therefore, to be optimized in all these respects. To what extent the specific Bragg grating design and the actual fabricated device correspond to each other has to be checked by appropriate measurements.

Various interferometric methods such as optical low-coherence interferometry, optical frequency-domain interferometry and even noninterferometric techniques which includes time-domain reflectometry or the one that rely on modulation could be denominated as optical network analysis. Especially, the noninterferometric techniques rely on modulation. In fact, any direct detection experiment with analog intensity modulation and an electrical network analyzer connected to the transmitter input and the receiver output yields the electrical transfer function from which magnitude and delay of the optical transfer function can be obtained. This scheme can be expanded to include different polarizations [10]. Of course, the sensitivity is limited to the direct-detection process. The phase of the optical transfer function could be accessible by integrating the group delay over frequency. This not only limits the accuracy but also does not allow the determination of correct phase relationship between transfer functions obtained from different polarizations.

Interferometric technique with fixed polarizations is the simplest, one-port form of optical network analysis [11]. Low-coherence interferometry directly yields the impulse response of a device with an excellent ~ 100 μm spatial resolution. In contrast, frequency-domain interferometry [12] which was used in this work, delivers the frequency-dependent complex reflection coefficients from which the impulse response is calculated. The laser tuning range limits spatial resolution, but large grating lengths may be investigated due to high coherence of a single-mode laser. Impulse response allows us to determine the complex coupling coefficients and hence longitudinal grating structure [13, 14]. Acquired knowledge about the vectorial nature of refractive index modulation depth and phase should allow for a correction of aberrations from the desired structure by effectively correcting the phase mask errors by longitudinally selective UV light post-processing [15, 16].

Therefore, a lithium niobate-based integrated optical network analyzer is proposed, designed, and built for longitudinal structure characterization of fiber Bragg gratings. The functionality of this in-house developed optical network analyzer is demonstrated:

(1) by measuring the vectorial grating structure of a uniform optical fiber Bragg grating under test [17] and

(2) by measuring differential group delay profiles of an integrated optical PMD compensator [18] which is introduced in the next subsection.

1.2.2 An Integrated Optical PMD Compensator

Polarization mode dispersion is caused by the noncircular fiber cores and poses a serious problem for transmitting 10 Gbit/s over older fiber and 40 Gbit/s over any type of fiber. It can be conveniently modelled as a concatenation of different differential group delay (DGD) sections connected by variable polarization transformers. It can be compensated if an appropriately oriented birefringence is added at the receiver side in reverse order [19]. Therefore, a perfect PMD compensator would consist of a large number of short DGD sections separated by variable polarization transformers. These polarization transformers would be adjusted so that the vectorial DGD profile of the PMD compensator would follow the DGD profile of the transmission line in reverse order. Implementation of such polarization transformers with an endlessly adjustable coupling phase was proposed many years ago by Heismann and Ulrich [20]. Since these polarization transformers require X-cut, Y-propagation lithium niobate; the natural birefringence (0.22 ps/mm) of this birefringent crystal cut can be used to compensate the DGD at the same time [21]. Since the function has already been demonstrated by R. Noé [22], the motive behind this work is to particularly optimize the electrode design for this type of integrated optical PMD compensator for the highest electro-optic efficiency by simulation studies [23]. This in-house developed integrated optical PMD compensator is characterized for different DGD profiles which were measured by the integrated optical network analyzer using inverse scattering technique [18]. The performance of this distributed PMD compensator can be pushed towards the highest bit rates if they are implemented in lithium–niobate–tantalate crystals. A Ta content y in $LiNb_{1-y}Ta_yO_3$ is good to realize a perfect PMD compensator at 160 Gbit/s [24].

1.3 Organization Of Thesis

The dissertation is organized into five chapters. Chapter 1 is an introduction. Chapter 2 explains the design of measurement setup and development of lithium niobate based integrated optical network analyzer.

Chapter 3 deals with the longitudinal structure characterization of fiber Bragg gratings by inverse scattering. It also emphasizes on the theory and experimentally obtained results on scalar as well as vectorial structure characterization of FBG.

Chapter 4 is devoted to design and development integrated optical polarization mode dispersion compensator whose different differential group delay profiles are determined by

inverse scattering technique using the above in-house developed integrated optical network analyzer.

Chapter 5 in short summarizes these two different application of lithium niobate-based integrated optical circuits to optical communication.

Chapter 2

Measurement Setup: Integrated Optical Network Analyzer

2.1 Measurement Setup

The measurement setup of our integrated optical network analyzer consist of optics and electronics. A 10 dB coupler is connected to a tunable laser in order to monitor the laser power. A 3 dB coupler splits the remaining power between two Mach-Zehnder Interferometers (MZI). The first MZI is a reference interferometer whose optical path length is adjusted to 0.5 m and acts as a high-resolution wavelength meter for frequency correction. The second MZI is a hybrid of the fiber- and integrated- optics and serves for measurement. It consist of an integrated optical network analyzer (ONWA) circuit based on X-cut, Z-propagation lithium niobate ($LiNbO_3$), and a 3x3 fiber coupler. The reflecting devices under test are connected to this MZI by means of an additional coupler. A 3x3 fiber coupler with 3 photodiodes at its outputs is used because it allows a more accurate phase measurement than a standard 2x2 coupler [25–28]. The real and imaginary parts of either frequency-dependent complex reflection coefficient or transmission coefficient of the device under test (DUT) are calculated from two linear combinations of the three-phase photocurrents obtained from the three photodiodes connected to the outputs of the respective 3x3 fiber couplers. Optical isolators are used to avoid any stray reflections from the photodiodes back into the measurement MZI.

The electronic hardware includes in-house developed 8-channel data acquisition system and 16-channel digital-to-analog converters. The data acquisition system consist of gain programmable transimpedance amplifiers, inverting voltage amplifiers for additional gain, integrators, and a high performance analog-to-digital converter (MAX 183) with 12-bit resolution for each channel. A 16-channel digital-to-analog converter uses high performance voltage output digital to analog converter (MAX 547) with 13-bit resolution with built-in high voltage amplifiers having an output voltage swing of ± 70 V. These are used to drive phase shifter and TE–to–TM mode converter electrodes under computer control. The in-house developed proportional-integral temperature controller is used to keep the

$LiNbO_3$-based IOC temperature constant. Figure 2.1 shows the measurement setup of an integrated optical network analyzer.

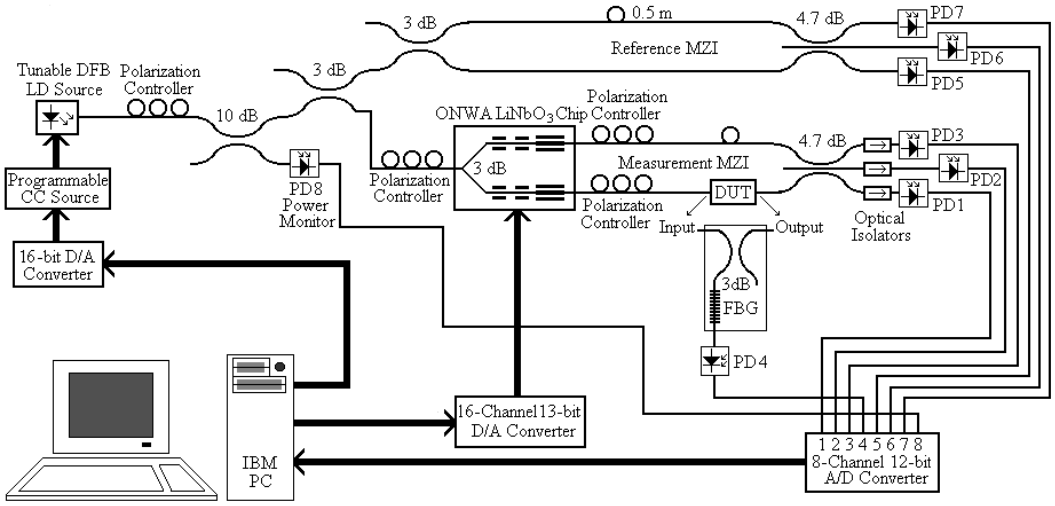

Figure 2.1: Measurement setup of an integrated optical network analyzer

2.2 The DFB Laser

In our transportable integrated optical network analyzer, a distributed feedback (DFB) laser diode is used as a tunable laser source. Of course, tunable twin–guide (TTG) laser diode can also be used. TTG has an advantage of having a higher tuning range say 4-5 nm as opposed to DFB laser, which could be tuned electronically over 100 GHz (0.8–1 nm) at 1550 nm . TTG laser require two currents to operate: one for pump and another for tuning. On the other hand DFB laser needs only pump current to operate. Only 50 GHz tuning range is used around the center wavelength of the Bragg grating, λ_B, in order to keep the measurement time short. Of course, thermal tuning is also possible to some extent. Figure 2.2 shows power and wavelength tuning characteristic response of the DFB laser diode at 1548 nm as a function of pump current.

This DFB laser diode is driven by the programmable constant current source which is under computer control. It uses high-performance 16-bit digital-to-analog converter from Analog Devices (AD669). Advantage of this technique is that one can have very high-resolution wavelength steps within the linewidth of the single-mode DFB laser diode and at the same time it allows us to do high-speed measurements, the major advantage of using electronic tuning. This high-speed measurement is a key to the success in such interferometric measurements where thermal noise in fiber limits the signal-to-noise ratio and the measurement accuracy.

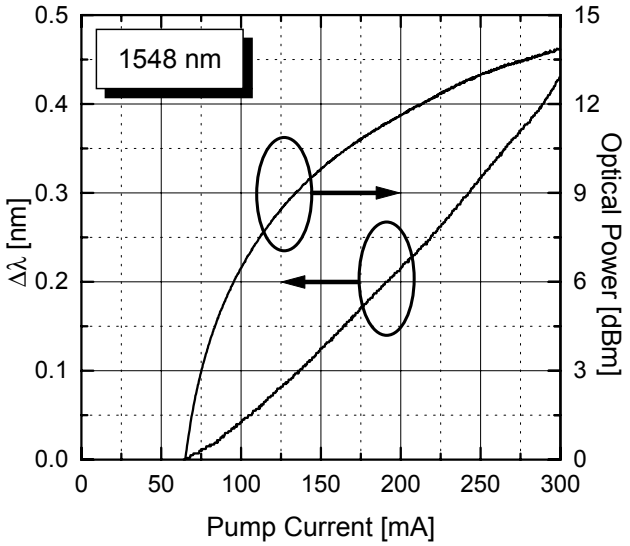

Figure 2.2: Power and tuning characteristic response of DFB LASER at 1548 nm

2.3 Design and Development of $LiNbO_3$-based IOC

The electrooptic control of guided modes is performed by the use of ferroelectric crystals such as lithium niobate and lithium tantalate. Lithium niobate is certainly one of the most important material exhibiting the largest Pockel's effect. It is very often used in integrated optics to implement intensity, phase, and polarization modulators and switches. A detailed study of it is thus necessary. It belongs to a crystalline class 3m (noncentrosymmetric) and has hexagonally closed packed crystal structure. It is a negative uniaxial crystal having extraordinary refractive index n_{e} for the light which is polarized along its optic axis and ordinary refractive index n_{o} for the light which is polarized along both the axes which are perpendicular to the optic axis.

Waveguide Fabrication

Three different techniques have been used to form waveguides in lithium niobate. Initially, waveguides are formed by thermal outdiffusion of Li_2O which results in an increased refractive index for the extraordinary index n_{e}. In addition to being limited to guiding light in only one polarization, achievable index change is very small and therefore provides waveguide modes whose confinement is relatively weak. In addition, channel waveguides cannot be formed conveniently except by etching ridge waveguides. These problems can be overcome using waveguides created by indiffusion of a dopant – almost exclusively titanium – to raise the refractive index. More recently, waveguides have been formed by an exchange process similar to that used for glass substrates. More specific is the proton exchange using benzoic acid.

Based upon the published results, titanium indiffused waveguides are currently preferred for general device development. This has become a well known and the most standardized technology in last two decades. One major advantage is that it can guide both polarizations: ordinary and extraordinary. The fabrication of titanium indiffused waveguides is quite straightforward. The titanium metal film is deposited onto optical grade lithium niobate substrates using electron-beam evaporation since the melting point of Ti is as high as $1725°$C. This metal film is patterned by photolithography followed by wet etching of Ti through positive phtotoresist to get Ti stripes of width equal to 7 μm. These Ti stripes are diffused thermally into lithium niobate at $1060°$C for about 8 hours in moist argon ambient. Cool down after diffusion is performed in oxygen to allow reoxidation of the crystal to compensate for the oxygen loss during diffusion. The water vapor treatment was initially employed to reduce the photorefractive effect but later it was found out that it also helps to reduce Li_2O outdiffusion which can cause unwanted planar guiding for the extraordinary polarization. Steadily this technique is mastered to fabricate very high quality Ti-indiffused channel waveguides in lithium niobate with propagation losses as low as 0.1 dB/cm.

Post-Waveguide Processing

If an electrode is to be placed on top of the waveguide, an intermediate buffer layer is needed to reduce propagation losses for TM-polarized modes due to direct metal cladding. SiO_2 is frequently employed. 0.2 μm thick layer of SiO_2 usually eliminates the measurable loading loss.

The choice of electrode material depends on the application. For relatively low-speed application (modulation frequencies below 100 MHz), an evaporated aluminum electrode (~ 0.5 μm thick), with a flash of chrome for adhesion, is sufficient. Initially, aluminum was employed. Sometimes, it used to get converted to colorless aluminum oxide due to heating. On the other hand, the most preferred material for very-high-speed devices is the gold. Gold is a noble metal and has noble properties. Therefore, gold was used in the fabrication of electrodes, with a flash of titanium for adhesion.

The substrate endface is prepared for either end-fire lens coupling or fiber butt-coupling by careful lapping and polishing. To eliminate Fresnel back reflections, multilayer anti-reflection coating made of series of quarter wave optical thickness, or QWOT for short, of SiO_2 and TiO_2 were used on the first IOC which was fiber pigtailed and packaged with straight end faces. This antireflection coating were not of very good quality, and, therefore, this used to introduce undesirable Fabry-Perot noise into measurement system. When this IOC was particulary used to evaluate the cleaved bare fiber end, which has very small reflectivity, the Fresnel back reflections became very critical. In fact, it was not possible to characterize the cleaved bare fiber end. Therefore, the next IOC was fiber pigtailed and packaged with angled endfaces so as to reduce Fresnel back reflections. This has indeed improved the overall performance of the integrated optical network analyzer.

Electro-Optic Effect

The linear electrooptic (*Pockel's effect*) effect, which is the basis for active waveguide device control, provides a change in the refractive index which is proportional to the applied electrostatic field. A voltage V applied to the electrodes placed over or alongside the waveguide, creates an internal electric field of approximate magnitude $|E| \simeq V/G$, G being the gap between the electrodes. Since the Pockel's effect is found in crystals without an inversion symmetry (noncentrosymmetric), such as lithium niobate, the sign of the induced refractive index change depends on the polarity of the voltage applied to it. On other hand, in a centrosymmetric crystals, linear electrooptic effect does not exist, while quadratic electrooptic effect (*Kerr effect*) is observed where the induced refractive index change is proportional to the square of the applied electric field intensity.

The equation of the index ellipsoid in the presence of an applied electric field can be written as

$$\begin{aligned}(\frac{1}{n_x^2} + r_{1j}E_j)x^2 + (\frac{1}{n_y^2} + r_{2j}E_j)y^2 + (\frac{1}{n_z^2} + r_{3j}E_j)z^2 \\ +2yzr_{4j}E_j + 2xzr_{5j}E_j + 2xyr_{6j}E_j = 1\end{aligned} \tag{2.1}$$

where E_j ($j = 1, 2, 3$) is a component of the applied electric field and summation over repeated indices j is assumed. Here 1, 2, and 3 corresponds to the principal dielectric axes x, y, z and n_x, n_y, n_z are the principal refractive indices. This new index ellipsoid reduces to the unperturbed index ellipsoid when $E_j = 0$. In general, principal axes of the perturbed ellipsoid do not coincide with the unperturbed axes (x, y, z). A new set of principal axes can always be found out by a coordinate rotation, which is know as principal-axis transformation of a quadratic form. The dimensions and orientation of the index ellipsoid (2.1) are, of course, dependent on the direction of the applied electrostatic field as well as 18 matrix elements r_{ij}. The linear change in the coefficients of the index ellipsoid due to applied electric field E_j along the principal axes is

$$(\Delta n)_i = -\frac{n^3}{2}\sum_{j=1}^{j=3} r_{ij}E_j, \tag{2.2}$$

where $i = 1, 2, \ldots, 6$ and r_{ij} is the 6×3 electrooptic tensor. The form, but not the magnitude, of the electrooptic tensor r_{ij} can be derived from symmetry considerations, which dictate which of the 18 electrooptic coefficients r_{ij} are zero, as well as the relationships that exist between the remaining coefficients. For lithium niobate, the coefficients of the electrooptic tensor r_{ij} are in the form

$$\begin{pmatrix} 0 & -r_{22} & r_{13} \\ 0 & r_{22} & r_{13} \\ 0 & 0 & r_{33} \\ 0 & r_{51} & 0 \\ r_{51} & 0 & 0 \\ -r_{22} & 0 & 0 \end{pmatrix} \tag{2.3}$$

The Table 2.1 tabulates the values of the r_{ij} coefficients which are not zero for the lithium niobate.

Table 2.1: Values of the electrooptic coefficients for lithium niobate

r_{ij} coefficients	Low-frequency value	High-frequency value
r_{33}	30.9 pm/V	30.8 pm/V
r_{51}	32.6 pm/V	28 pm/V
r_{13}	9.6 pm/V	8.6 pm/V
r_{22}	6.8 pm/V	3.4 pm/V

By inserting the electrooptic tensor r_{ij}, the values of Δn can be written as the elements of a symmetric 3×3 matrix. For lithium niobate

$$(\Delta n)_{ij} = -\frac{n^3}{2} \begin{pmatrix} -r_{22}E_y + r_{13}E_z & -r_{22}E_x & r_{51}E_x \\ -r_{22}E_x & r_{22}E_y + r_{13}E_z & r_{51}E_y \\ r_{51}E_x & r_{51}E_y & r_{33}E_z \end{pmatrix} \tag{2.4}$$

where n is either the ordinary index n_{o} or the extraordinary index n_{e} value. By carefully looking at the above electrooptic tensor of lithium niobate, certain useful conclusions can be drawn [29]:

> [1] r_{11}, r_{21}, r_{31}, r_{41} are all zero. There will be no stretching of the index ellipsoid along the principle axes under applied electrostatic field E_x.
> [2] r_{43}, r_{53}, r_{63} are all zero. There will be no stretching of the index ellipsoid along the principle axes under applied electrostatic field E_z.
> [3] An applied electric field E_y will cause both stretching along the principal-axes as well as the rotation of the index ellipsoid cross-section in the YZ-plane.

Perturbation of the index ellipsoid due to electrooptic effect depends on the relative orientation of the polarization state of the input optical signal, the axis of propagation, the crystal cut, and the magnitude and direction or sign of the applied electrostatic field. Utilization of the diagonal elements 11, 22, and 33 of the perturbed refractive index matrix results in an index change and therefore, a phase change, for an incident optical field polarized along the crystallographic x-, y- and z-axes, respectively. The diagonal elements causes an index change, which are essential for modulators and switches, for the optical field polarized along the crystallographic j-axis, for the given electric field which is applied in the appropriate direction. The off-diagonal elements, on the other hand, represent an electrooptically induced mode mixing or conversion between the otherwise orthogonal polarization components. It represents a rotation of the index ellipsoid that causes a mode coupling which is proportional to the relevant electrooptic coefficient due to the application of electrostatic fields. Utilization of off-diagonal electrooptic elements is necessary to induce polarization change in Ti:$LiNbO_3$ waveguides, i.e. TE–TM mode converters.

Design Considerations: 1x2 Optical Power Splitter

Single-mode 1x2 optical power splitter is realized in X-cut, Z-propagation $LiNbO_3$ using standard Ti-indiffused waveguide technology [30–33]. Scaling laws for the design of such waveguide based components are derived in [34]. Waveguides are fabricated by in-diffusing ~ 100 nm thick, 7 μm wide, Ti-stripes for 7.5 hours in the moist argon ambient at 1060° C. Waveguides propagation losses are measured using the Low-Finesse Method [35] and are of the order of ≈ 0.1 dB/cm for both TE and TM polarized modes. Power splitting uniformity of this 3 dB power splitter is within ≈ 0.5 dB for the TE-polarized modes.

2.3.1 Polarizer

A linear polarizer is an optical device, birefringent or not, that only transmits one linear state of polarization and suppresses any transmission of the orthogonal state of polarization. This is of course the definition of an ideal polarizer; a real component always lets through a fraction of the orthogonal state. An extinction ratio must therefore be defined in order to characterize such components. A linear analyzer is fundamentally identical to a linear polarizer. Its particular name stems from the fact that it enables the emerging state of polarization to be analyzed.

These devices are characterized by a Jones matrix $\mathbf{J}_\mathrm{P}$ which is expressed with respect to a reference coordinate system Oxy. If the phase factor, which simply renders the propagation of the light in the material medium making up the device, is not taken into account, the Jones matrices $\mathbf{J}_{\mathrm{P}_x}$ and $\mathbf{J}_{\mathrm{P}_y}$ of the polarizers whose principal axes are respectively the axes Ox and Oy are given by:

$$\mathbf{J}_{\mathrm{P}_x} = \begin{pmatrix} 1 & 0 \\ 0 & 0 \end{pmatrix} \qquad \mathbf{J}_{\mathrm{P}_y} = \begin{pmatrix} 0 & 0 \\ 0 & 1 \end{pmatrix} \tag{2.5}$$

From a mathematical point of view, the Jones matrices of the polarizers are the matrices associated with projection operators ($\mathbf{J}_\mathrm{P}^2 = \mathbf{J}_\mathrm{P}$) whose eigenvalues are 1 and 0. An important property of projection operation is that the intensity transmitted by a polarizer is always less than or at best equal to the incident intensity it receives. The Jones matrices of linear polarizers cannot be associated with unitary transformation because $\det(\mathbf{J}_\mathrm{P}) = 0$.

Let us consider a linear polarizer whose principal axis is the axis Ox. Whenever this polarizer is turning in front of the a linearly polarized light having an intensity of 1, its transmission T varies between two values, T_max and T_min, according to relation

$$T = (T_\mathrm{max} - T_\mathrm{min}) \cos^2 \theta + T_\mathrm{min} \tag{2.6}$$

where θ is the angle between the axis Ox and the azimuth of the polarized light. This law of transmission is known as Malus' law.

In the case of an ideal polarizer, T_min is equal to 0 and T_max is equal to 1, according to Malus' law. However, the imperfection of the device and the presence of the parasitic

light imply that Malus' law is only partially obeyed. As a general rule, the principal transmissions ($\theta = 0$ and $\theta = \pi/2$) $T_{\max}$ and $T_{\min}$ fulfill the relation: $T_{\min} \ll T_{\max}$ and the polarization extinction ratio (PER) is defined as

$$\mathrm{PER} = \frac{T_{\max}}{T_{\min}}. \tag{2.7}$$

The value of $T_{\max}$ depends on the nature of the material and also on the physical polarizing effect used by the polarizer. There are several physical effects that allow polarizers to be made. Among these metallic thin film polarizer that suppresses the TM-polarized mode by a suitable dielectric/metal overlay due to the resonant coupling with a surface plasmon mode offers the best compatibility with fabrication process of Ti:$LiNbO_3$ waveguide-based devices and is a promising option for guided wave optics.

The general principle upon which polarizers in isotropic waveguides are built is based on a greater loss of a given state (TE- or TM-polarized) with reference to the other during propagation. The loss of power is not due to a dichroic phenomenon, but to the inability of a mode to propagate. We know that a mode can only propagate if its normalized frequency V is larger than its cut-off frequency. The separation of the two fundamental modes TE_0 and TM_0 may be done by using a guiding structure containing, for instance, a metal.

Polarizers are used to set a reference polarization and to ensure that phase modulated light having a single polarization enters the mode converter sections of the IOC. This indeed suppress the second undesired polarization mode, if any, from being interfered in 3x3 fused fiber coupler in order to do polarization resolved grating characterization. It is easy to fabricate TE-pass polarizers than TM-pass polarizers and, therefore, TE-pass metal-clad polarizers based on the surface plasmon effect are used to suppress the TM-polarized mode in Ti in-diffused $LiNbO_3$ waveguides.

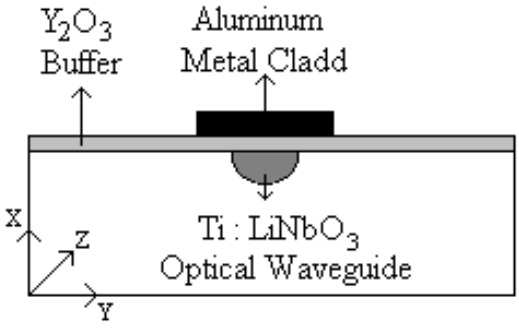

Figure 2.3: Cross section of a metal-clad polarizer on X-cut, Z-propagation Ti:$LiNbO_3$ optical waveguide

Device structure

Figure 2.3 shows the cross section of polarizer based on X-cut, Z-propagation lithium niobate using the thin metals films. It simply consist of metal-cladded optical waveguide but with a intermediate dielectric buffer layer of right thickness and dielectric constant to enhance the extinction of the TM-polarized mode due to the resonant coupling with a surface plasmon mode and to reduce the excess propagation losses for the TE-polarized mode.

Principle of Operation

Metal behaves as a high loss dielectric material with a '-'ve dielectric constant over the entire frequency range of light, because the inertial effect of the carriers (electrons) inside the metal becomes dominant when the frequency exceeds the plasma frequency of the metal itself. Therefore, metal cladding on top of the optical waveguide provides significant attenuation to the TM-polarized modes. This results from the fact that the TM-polarized mode penetrates more deeply into metal than does the TE-polarized mode. Metal-clad waveguide exhibits complex propagation constant for the TM-polarized modes and real propagation constant for the TE-polarized modes. TM-polarized mode is highly attenuated while TE-polarized mode pass through the polarizer.

For the design of metal-clad polarizers, it is essential to use an intermediate dielectric buffer layer with a right dielectric constant and a right thickness between the cladding metal and the waveguide; and this layer helps to fulfil the phase matching condition between the TM-polarized mode and the surface plasmon mode. An attenuation coefficient is at it's peak value and can be as high as ~ 100 dB/cm. This completely blocks the TM-polarized mode and passes TE-polarized mode without a significant attenuation.

Design Considerations

Aluminum is a natural choice as a cladding metal since it has a large '-'ve dielectric constant ($-114-j37$) and due to the ease of fabrication. There are several choices of buffer materials including Si_3N_4($n_b \sim 1.89$), Ta_2O_5($n_b \sim 2.1$), and Y_2O_3($n_b \sim 1.795$), MgO($n_b \sim 1.75$), Nb_2O_5 ($n_b \sim 1.95$) etc. These materials are chosen on the basis that they have a high refractive index at 1.55 μm wavelength and is comparable to that of the lithium niobate refractive index of 2.2.

Stock [36] realized TE-pass polarizers on Ti:$LiNbO_3$ waveguides with > 55 dB of PER using Au, Al, and Ti metal cladding at 780 nm wavelength and has used MgO as a buffer material. Thyagarajan et al [37] has done numerical modelling of single-mode metal-clad graded-index waveguides with a dielectric buffer layer of Y_2O_3. Čtyroký and Henning [38] have realized 2 mm long TE-pass polarizer at 1.3 μm using 45 nm thick Si_3N_4 and 200 nm thick Al with an extinction ratio > 35 dB. We want to have TE-pass polarizers at 1.55 μm wavelength and this wavelength is nearer to the polarizers realized by Čtyroký at 1.3 μm, and therefore, it was planned to use the Si_3N_4 as buffer layer and aluminum as a cladding

metal with a layer thicknesses of 20–30 nm and 500 nm, respectively. The silicon nitride is an ideal choice since it is the most stable material from technological and physical point of view. It is decided to optimize the buffer thickness for a 3 mm long and 50 μm wide polarizer so that it at least gives 10 dB extinction ratio for TM-polarized modes as compared to TE-polarized modes.

Realization and Characterization

Initially, in the development of this integrated optical network analyzer circuit, the near-Z-axis propagation was used to cancel the modal birefringence of the Ti-indiffused optical channel waveguides in X-cut, Z-propagation $LiNbO_3$ in order to make on-chip polarization transformers more efficient. But this off-axis propagation makes these TE-pass polarizers nonideal. This is because the TM-polarized mode is regenerated in the waveguide after the polarizer. This regenerated TM-polarized mode effectively degrades the PER of TE-pass polarizers. Details of this phenomenon are explained in Section 2.3.4. Therefore, it was decided to fabricate several polarizers on the X-cut, Z-propagation Ti:$LiNbO_3$ straight channel waveguides with varying buffer materials and thicknesses in order to optimize the PER. Thickness of Al was chosen to be sufficiently thick (500 nm) to have a higher attenuation coefficient for a 3 mm long polarizers. Polarization extinction ratio is measured for these metal-clad polarizers using a pair of Glan-Thompson polarizers having an extinction ratio > 55 dB. The measured results of the PER for various buffer materials and thicknesses are summarized in Table 2.2.

Table 2.2: PER of TE-pass polarizers for various buffer materials

Material	Thickness	Length	PER	Problems
no buffer	0 nm	1.5 mm	3 dB/mm	Poor PER
Si_3N_4	30 nm	4 mm	2.75 dB/mm	In technology
Ta_2O_5	35 nm	4 mm	2.50 dB/mm	Poor PER
Y_2O_3	27 nm	3.8 mm	9.5 dB/mm	Good PER

Unfortunately polarizers did not work satisfactorily, even after several trials with Si_3N_4. Main problem was in the fabrication of stoichiometric Si_3N_4 buffer layer. Next highest refractive-index material Ta_2O_5 was tried but performance was more or less the same. Next obvious and possible choice was to use Y_2O_3 as a buffer material. Y_2O_3 based polarizers fortunately worked with an extinction ratio of 9.5 dB/mm. It is very difficult to fabricate polarizers with very good repeatability because of the stringent requirement on the uniformity of the buffer thickness, buffer stoichiometry and hence on the buffer refractive index. These parameters are very difficult to control during the fabrication of buffer layer and of course the buffer layer plays a key role in the realization of integrated optic metal-clad polarizers with a very high extinction ratio.

Conclusion

The yttrium oxide based metal-clad polarizers giving PER of $\approx$ 30 dB for 3 mm long polarizers with 27 nm thick Y_2O_3 and 500 nm thick aluminum were optimized for our application.

2.3.2 Phase Modulator

Perhaps, the simplest waveguide electrooptic device is the phase modulator where electro-optically induced refractive index change causes a phase shift in the guided light. Figure 2.4 shows the Ti:$LiNbO_3$ waveguide based phase modulator with an applied voltage, V_π, as defined later, is used to characterize the phase modulators.

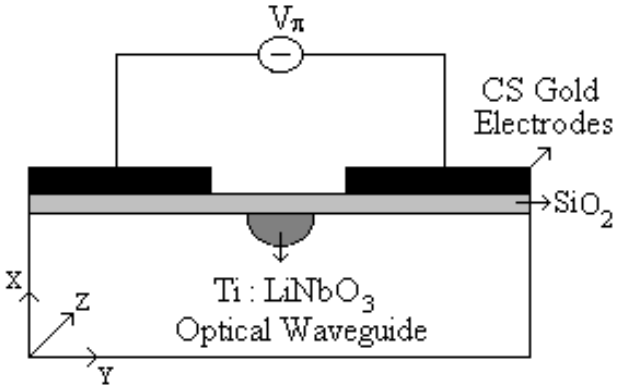

Figure 2.4: Cross section of phase modulator on X-cut, Z-propagation $LiNbO_3$ with an applied voltage V_π

Device Structure

Phase modulator simply consist of a Ti in-diffused optical channel waveguide placed in between the set of uniform electrodes of length, L, separated by a gap, G. The horizontal y-directed electrostatic field (E_y) is produced by applying a voltage, V, across a gap, G, of uniform electrodes which gives rise to the local electrooptically induced index change and hence a corresponding phase change.

Principle of Operation

The local electrooptically induced refractive index change for this particular crystal cut and propagation direction is given by

$$\Delta n_{22} = -\frac{n_o^3}{2} r_{22} E_y. \tag{2.8}$$

However, neither the applied electrostatic field nor the optical field is uniform. It is convenient to model the effective applied electrostatic field inside the waveguide by that of a simple parallel plate capacitor as in the bulk case modulator where the lithium niobate crystal is sandwiched between two electrodes and both optical and electrostatic fields are assumed to be uniform. The correction factor from this simple model is given by the field overlap integral Γ. The effective electrooptically induced refractive index change is given by

$$\Delta n_{22}(V) = -\frac{n_{\mathrm{o}}^3 r_{22}}{2}\frac{V}{G}\Gamma, \tag{2.9}$$

where n_{o} is the ordinary refractive index of $LiNbO_3$, an interelectrode gap G, and Γ is the overlap integral between the applied electrostatic field and the optical mode. The quantity Γ is given by

$$\Gamma = \frac{G}{V}\frac{\int\int |\mathbf{E}_o(x,y)|^2 \mathbf{E}_y(x,y,z)dxdy}{\int\int |\mathbf{E}_o(x,y)|^2 dxdy}. \tag{2.10}$$

The total phase shift over the interaction length L is then

$$\phi = \Delta\beta L = -\frac{\pi n_{\mathrm{o}}^3 r_{22}}{\lambda}\frac{V}{G}L\Gamma. \tag{2.11}$$

Phase modulators are generally characterized by the voltage V_π which is defined as the voltage required to obtain a phase shift of π rad. However, voltage–length product is more useful to compare the performance of different phase modulators and is defined as

$$V_\pi L = \frac{\lambda G}{\pi n_{\mathrm{o}}^3 r_{22}\Gamma}. \tag{2.12}$$

Phase modulator is generally represented by a Jones matrix,

$$\mathbf{J}_{\mathrm{PS}} = \begin{pmatrix} e^{\jmath\frac{\phi}{2}} & 0 \\ 0 & e^{-\jmath\frac{\phi}{2}} \end{pmatrix}. \tag{2.13}$$

It is simply modelled as a retarder with a phase angle ϕ given by (2.11). It is very important to note that, the Jones matrices of phase modulators are unitary matrices i.e. the product $JJ^\dagger = I$. Mathematically speaking, the polarization transformation done by the phase modulator is a unitary transformation. The norm and orthogonality of the vectors representing the incident states of polarization are thus conserved when the device is passed i.e. the emerging state of polarization is same as the the incident state of polarization.

Design Considerations

Ordinary refractive index of the $LiNbO_3$, n_{o}, equals 2.2125 at $\lambda = 1.55$ μm. Relevant electrooptic coefficient, r_{22}, is 6.8 pm/V. Length and gap of phase modulator electrodes are 15 mm and 15 μm, respectively. The unknown optical and electrostatic field overlap

integral factor, Γ, is used in the calculation of ϕ and hence the voltage V_π, which characterizes the phase modulators. Once the overlap integral factor, Γ, is known, the voltage, V_π, required to give a phase shift of π rad using this retarder can be calculated.

Electrostatic field E_y is only required to compute the field overlap integral factor, Γ, as defined by Kim and Ramaswamy [39] in (2.10). Software based on the Point Matching Method (PMM) formulated by Marcuse [40] is developed in Borland C++ to calculate the electrostatic fields in the $LiNbO_3$. PMM is described in Appendix A. Optical mode is assumed to Gaussian and Hermite-Gaussian along the width and depth of the single-mode Ti in-diffused optical waveguide in $LiNbO_3$ with mode field diameters matched to our experimental values. These experimental values of MFD are used to generate polarization dependent optical intensity profiles for evaluating the field overlap integrals. Appendix B gives details of this.

TE-polarized optical mode with full-width-half-maximum of $7\ \mu\mathrm{m}$ and $4\ \mu\mathrm{m}$ along the width and depth of the Ti in-diffused waveguide is assumed in the simulation. $0.3\ \mu\mathrm{m}$ thick buffer layer of SiO_2 is used to eliminate the measurable loading looses, due to metal cladding, especially for the mode converter electrodes. Phase modulator electrodes has width of $100\ \mu\mathrm{m}$. If the interelectrode gap, $G = 15\ \mu\mathrm{m}$, then $\Gamma \approx 0.51$. Voltage $V_\pi \approx 40\ \mathrm{V}$ for 15 mm long electrodes.

Realization and Characterization

Realized phase modulators could be conveniently characterized for the measurement of voltage V_π using the Fabry-Perot technique. Low–Finesse Method proposed by Regener and Sohler [35] for the measurement of propagation losses in optical waveguides is also based on the Fabry-Perot technique, where the optical straight channel waveguide with its end faces polished perpendicular to the waveguide axis forms a optical resonator (Fabry-Perot etalon). The transmitted intensity of the resonator varies periodically with the optical phase difference, ϕ, which can be tuned by the temperature for simplicity, or, in principle, it can also be tuned by means of an applied electrostatic field. For this particular measurement, it is necessary to use single frequency laser otherwise it is difficult to monitor the interference fringes. Phase modulator is used to tune the Fabry-Perot cavity and is driven by a triangular wave obtained from the signal generator. The output intensity is monitored using the photodiode and an oscilloscope. It is to be ensured that either the two maxima or two minima of the Fabry-Perot fringes are within the single ramp, either going up or down. Voltage difference between these two points on ramp corresponding to these two maxima or minima directly yields the voltage V_π.

Figure 2.5 shows the response of the phase modulator's output intensity for the given input voltage. As it can be seen from the graph, $V_\pi = 40.0$ V and this agrees very well with the theoretically estimated value of V_π. Phase modulator with 20 mm long electrodes is also fabricated to verify the voltage-length product. $V_\pi = 30.0$ V for this phase modulator. Therefore, the voltage-length product ($V_\pi \times L$) equals 60 V-cm for both the devices and is found to be a constant.

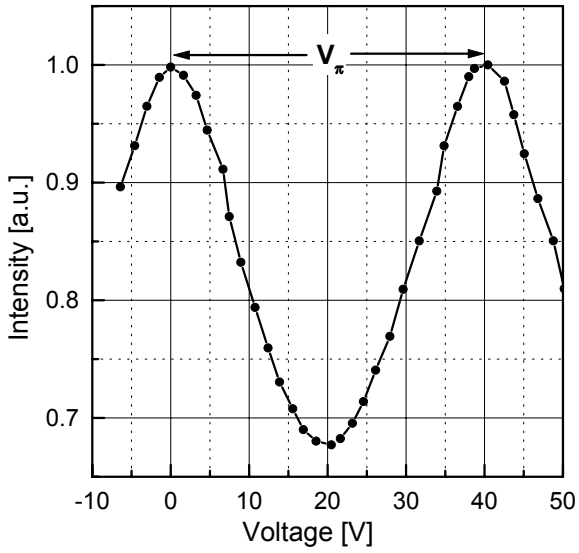

Figure 2.5: Characteristic response of the phase shifter as a function of input voltage

Conclusion

15 mm long phaser modulator with a gap of 15 μm is realized and characterized for the voltage V_π ($= 40.0$ V) using the Fabry-Perot technique. Voltage-length product equals 60 V-cm for this device and is found to be a constant.

2.3.3 TE↔TM Mode Converter

An electrooptic polarization transformer or converter is a compact device that can provide an electrical control over the polarization state and can be expected to serve a variety of useful functions. Such devices have been demonstrated with Ti:$LiNbO_3$ waveguides. Optical polarization state can be defined in a number of bases, for our purpose it is convenient to define the polarization state in terms of the polarization angle, θ and the phase angle ϕ. The normalized TE and TM amplitudes can be written as

$$\begin{pmatrix} A_{\mathrm{TE}} \\ A_{\mathrm{TM}} \end{pmatrix} = \begin{pmatrix} \cos\theta \\ e^{\jmath\phi}\sin\theta \end{pmatrix}, \tag{2.14}$$

where θ specifies the relative TE/TM amplitudes while ϕ is the phase difference between the TE and TM components. Light is linearly polarized at angle θ if $\phi = 0$; $\theta = 0$ represent purely TE polarized, while $\theta = \pi/2$ is purely TM. Right circularly polarized light, for example, is represented by $\theta = \pi/4$ and $\phi = \pi/2$. In passive Ti:$LiNbO_3$ waveguides, light that is linearly polarized along a principal axis has its polarization maintained for propagation along a principal axis. Thus, for example, light incident as TE (TM) polarization to waveguides in z (or x, or y)-cut lithium niobate exits in the same state.

In order to implement broadband TE↔TM mode converters, a natural and the best choice is to use X-cut, Z-propagation $LiNbO_3$ crystal [41–44]. Advantage of this particular crystal cut is that one is free from the material birefringence and can obviously make use of the wavelength independent uniform electrodes to perform mode conversion. Moreover, they feature a high optical damage threshold, low temperature dependence and hence little DC drift as demonstrated by Taniyavaran [45, 46].

Device Structure

Figure 2.6 shows the cross section of uniform electrodes of length L used for the implementation of broadband TE↔TM mode converters on X-cut, Z-propagation $LiNbO_3$ with the applied voltages. A center electrode of width, W, is directly placed on top of the Ti in-diffused optical channel waveguide, which may or may not be grounded. Side electrodes are separated by gap, G, and are sometimes segmented for the implementation of several electrooptic waveplates.

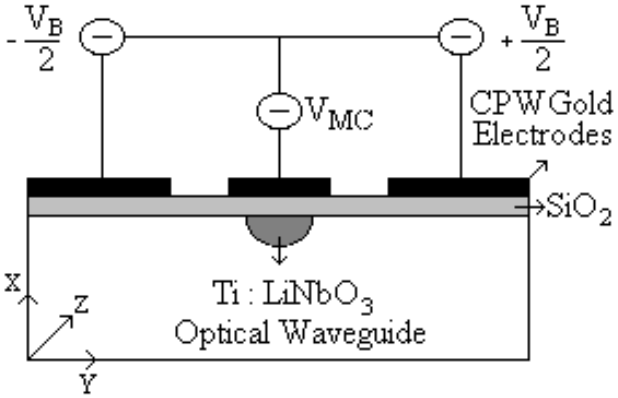

Figure 2.6: Cross-section of TE–TM mode converter on X-Cut, Z-propagation $LiNbO_3$ with an applied voltages for compensating modal birefringence and mode conversion

Principle of Operation

If the voltages $\pm(V_B/2)$ and V_{MC} are applied to two side electrodes and the center electrode of the mode converter, respectively, then its Jones matrix is given by

$$J_{MC} = \begin{pmatrix} \cos\psi + \jmath\cos\gamma\sin\psi & \jmath\sin\gamma\sin\psi \\ \jmath\sin\gamma\sin\psi & \cos\psi - \jmath\cos\gamma\sin\psi \end{pmatrix}. \tag{2.15}$$

The electrostatic field along y-axis (horizontal field), E_y, generated by applying the bias voltage V_B to two side electrodes compensates for the modal birefringence by additionally providing the electrooptically induced phase shifts between the TE and TM polarized modes via r_{12} $(= -r_{22})$ and r_{22} coefficients, and $r_{22} = 6.8$ pm/V. The electrostatic field

along x-axis (vertical field), E_x, generated by applying a voltage $V_{\rm MC}$ to central electrode leads to electrooptically induced TE–TM mode conversion via r_{61} ($= -r_{22}$) coefficient. $\psi = \sqrt{\kappa^2 + \delta^2}L$, $\tan\gamma = \kappa/\delta$, κ is the coupling constant, and δ is the phase mismatch parameter between TE and TM polarized modes, and L is the length of mode converter electrodes. κ and δ are expressed as $\kappa = \pi n_{\rm o}^3 r_{61} E_x \Gamma/\lambda$ and $\delta = (\Delta\beta)/2 + \delta'$, where $\delta' = \pi n_{\rm o}^3 r_{22} E_y \Gamma/\lambda$. $\Delta\beta$ is the modal birefringence and δ' is the difference in the propagation constants of the TE and TM polarized modes induced by the external electric field to compensate for $\Delta\beta/2$.

Ti in-diffused waveguide sees the ordinary refractive index $n_{\rm o}$ in both the x (or y)-direction, since the waveguide is fabricated on X-cut, Z-propagation $LiNbO_3$. Ideally, the waveguide is isotropic. However, the residual TE–TM waveguide birefringence (also known as modal birefringence) is found to be harmful for the operation of some of the devices such as mode converters. Order of this modal birefringence is $\Delta n \approx 1.0 \times 10^{-4}$ at $1.55\ \mu$m wavelength and hence $\Delta\beta$ ($= (2\pi/\lambda)\Delta n$) is of the order of 4–5 rad/cm. This residual modal birefringence, in fact, ruins the phase matching condition between the two polarization modes and therefore limits the efficiency of TE↔TM mode conversion.

One option is to use near-Z-axis propagation, say at an angle of 2° to regain the phase matching condition [47]. This happens in Ti in-diffused channel waveguides because the effective index for a TE-polarized mode, $N_{\rm TE}$, is greater than that of a TM mode, $N_{\rm TM}$. Rotation of propagation direction in the YZ-plane at an angle θ lowers the value of $N_{\rm TE}$ to

$$\begin{aligned} N_{\rm TE}(\theta) &\simeq \frac{n_{\rm o} n_{\rm e}}{\sqrt{n_{\rm e}^2 \cos^2\theta + n_{\rm o}^2 \sin^2\theta}}, \\ N_{\rm TM}(\theta) &\simeq n_{\rm o} \end{aligned} \tag{2.16}$$

while leaving $N_{\rm TM}$ unchanged. Second option is to apply high bias voltages to two side electrodes to compensate for $\Delta\beta$ [48], as explained above.

Using the coupled mode theory, one can immediately write the expressions for the power in TE and TM polarization modes as

$$\begin{aligned} P_{\rm TE} &= 1 - \frac{\kappa^2}{\kappa^2 + \delta^2} \sin^2(\sqrt{\kappa^2 + \delta^2}L) \\ P_{\rm TM} &= \frac{\kappa^2}{\kappa^2 + \delta^2} \sin^2(\sqrt{\kappa^2 + \delta^2}L) \end{aligned} . \tag{2.17}$$

For complete TE to TM mode conversion, boundary condition becomes $P_{\rm TE} = 0$ and $P_{\rm TM} = 1$ for the given TE input. If $\delta = 0$, then this boundary condition simplifies to $\sin^2(\kappa L) = 1$. The voltage required for full TE to TM mode conversion and vice-versa which characterizes the mode converters is given by

$$V_{\rm MC} = \frac{\lambda G}{2 n_{\rm o}^3 r_{61} \Gamma L}. \tag{2.18}$$

Design Consideration

Ordinary refractive index of $LiNbO_3$, n_o, equals 2.2125 at $\lambda = 1.55\ \mu\mathrm{m}$. The relevant electrooptic coefficient $r_{61} = -r_{22} = -6.8$ pm/V. The only unknown field overlap integral factor Γ is used in calculation of coupling constant κ and hence in the calculation of voltage required for full mode conversion, V_{MC}.

Mode converters with $25\ \mathrm{mm}$ long electrodes, $10\ \mu\mathrm{m}$ wide central electrode, and an interelectrode gap of 6 and 8 $\mu\mathrm{m}$ are designed. The electrostatic field, E_x, is calculated using the PMM to calculate the unknown field overlap integral factor, Γ. In the simulation, same parameters for FWHM of the TE-polarized optical mode were used. Table 2.3 summarizes the simulation results for the calculation of overlap integral factor Γ and V_{MC} for 25 mm long mode converters with different interelectrode gaps.

Table 2.3: Simulation results for the calculation of Γ and V_{MC}

G_{MC} [μm]	Γ	V_{MC} [V]
6	≈ 0.26	9.75
8	≈ 0.33	10.25

Realization and Characterization

Therefore, two devices each having a 25 mm long electrooptic mode converter as shown in Figure 2.6, with a center electrode width of $10\ \mu\mathrm{m}$, gap of $6\ \mu\mathrm{m}$, and $0.3\ \mu\mathrm{m}$ thick buffer layer of SiO_2 were fabricated in house. The first device used 2° off-axis propagation to cancel the modal birefringence, with a device length of ≈ 47 mm and the second device used principal axis propagation.

No operational voltages were applied to the mode converter on the first device. This device by default gave $> 8\ \%$ TE to TM static mode conversion for pure input TE mode at 1550 nm. Very similar results were also reported in [47, 49]. This phenomenon was later found to be length–dependent.

The second device needed bias voltages to operate as it needs to cancel the modal or TE–TM waveguide birefringence. When no voltages were applied either to compensate for the modal birefringence or to operate the mode converter, there was no static TE–TM polarization mode conversion, as was observed in the first device. Bias voltages which were applied to the two side electrodes were varied so as to maintain zero waveguide birefringence and to obtain the smallest possible voltage required for full TE to TM mode conversion. This phase matching condition must be fulfilled in addition to mode coupling due to the principal axis rotation of the index ellipsoid in order to reach $100\ \%$ mode conversion. Bias voltages were $\pm V_B/2 = \pm 38$ V. The voltage required for full TE to TM mode conversion was $V_{MC} = 9.75$ V, as seen from the mode converter switching curves shown in Figure 2.7 and it agrees well with the theoretically estimated value of 9.75 V. When the mode conversion voltage was switched off (remember that the bias voltages were still switched on) the device gave $> 5\ \%$ TE to TM static polarization mode conversion for the

input TE mode. When the bias voltages were varied, the coupling was found to vary and it was found that this time static mode coupling was dependent on the electrostatic field strengths which were used to compensate the modal birefringence. When bias voltages were also switched off the entire power was present in the input TE mode as expected.

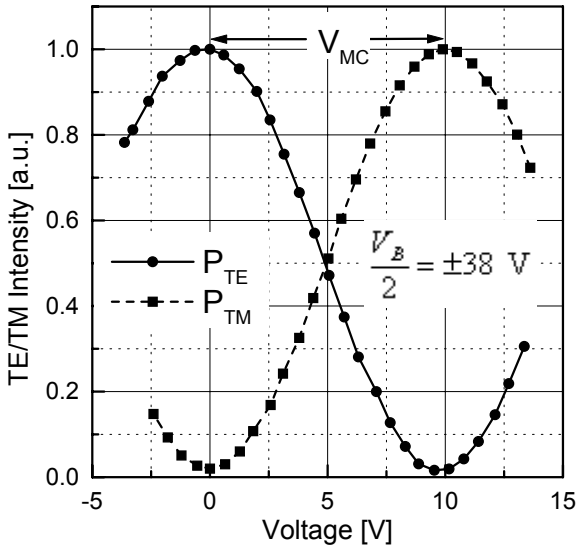

Figure 2.7: Characteristic response of the mode converter as a function of input voltage

Result Discussion

These experiments confirms that there is a change in the state of polarization of light and this was interpreted as a rotation of the polarization plane [50]. After compensating the modal birefringence which is linear, the circular birefringence may become the next hurdle to make mode converters ideal. This may be called as a form of static polarization mode coupling and is observed in both devices using either off-axis or principal-axis propagation. In the off-axis case, static mode coupling is length-dependent and in the principal-axis case it depends on the applied electrostatic field strengths which were used to compensate the modal birefringence. Both experiments reveal that there exists a phenomenon of static polarization mode conversion.

A symmetric 3x3 dielectric tensor generally characterizes the optical properties of anisotropic crystals such as $LiNbO_3$ and is given by

$$\varepsilon(0) = \begin{pmatrix} \varepsilon_{11} & 0 & 0 \\ 0 & \varepsilon_{22} & 0 \\ 0 & 0 & \varepsilon_{33} \end{pmatrix}. \tag{2.19}$$

In the off-axis propagation case, we rotate the direction of propagation in the YZ-plane about the X-axis in order to compensate for the modal birefringence. So the off-diagonal

terms involving Y and Z components of electromagnetic fields are responsible for this static mode coupling. To find these off-diagonal terms, one needs to carry out the simple coordinate transformation $R(\theta)\varepsilon(0)R(-\theta)$ using a rotation matrix

$$R(\theta) = \begin{pmatrix} 1 & 0 & 0 \\ 0 & \cos\theta & -\sin\theta \\ 0 & \sin\theta & \cos\theta \end{pmatrix}, \tag{2.20}$$

where $\theta = 2^\circ$. The rotated dielectric tensor is given by

$$\varepsilon(\theta) = \begin{pmatrix} \varepsilon_{11} & 0 & 0 \\ 0 & \varepsilon_{22}\cos^2\theta + \varepsilon_{33}\sin^2\theta & (\varepsilon_{22} - \varepsilon_{33})\cos\theta\sin\theta \\ 0 & (\varepsilon_{22} - \varepsilon_{33})\cos\theta\sin\theta & \varepsilon_{22}\sin^2\theta + \varepsilon_{33}\cos^2\theta \end{pmatrix}. \tag{2.21}$$

The perturbation is $\Delta\varepsilon = (\varepsilon_{22} - \varepsilon_{33})\cos\theta\sin\theta$. The input is TE mode with electric field distribution (0, E_y, 0) and the output is the TM mode with electric field distribution (E_x, 0, E_z). Once we know $\Delta\varepsilon$, we can immediately calculate the coupling coefficient

$$\kappa = \kappa^t_{\mu,\nu} + \kappa^z_{\mu,\nu}, \tag{2.22}$$

which characterizes this static polarization mode coupling, where μ and ν are TE and TM polarized modes involved in the coupling process, respectively. The tangential coupling coefficient $\kappa^t_{\mu,\nu}$ is zero. The longitudinal coupling coefficient $\kappa^z_{\mu,\nu}$ is found to be responsible for this type of static mode coupling. This is the **rare case** of transverse–longitudinal coupling and the power is coupled to the output TM mode from the input TE mode via longitudinal component E_z of the TM mode. Equation (46) in [51] tells which of the electromagnetic field components are involved in the coupling process if we insert our dielectric tensor given in (2.21) having off-diagonal terms. The coupling coefficient $\kappa^z_{\mu,\nu}$ is

$$\kappa^z_{\mu,\nu} = \frac{\omega\varepsilon_0}{4}\int \mathbf{E}^{\mathbf{t}\dagger}_{\boldsymbol{\mu}}\Delta\varepsilon(x, y, z)\mathbf{E}^{\mathbf{z}}_{\boldsymbol{\nu}}dxdy, \tag{2.23}$$

which is formally derived by Marcuse in [51]. Above equation simplifies to

$$\begin{aligned} \kappa = \kappa^z_{\mu,\nu} &= \frac{\omega\varepsilon_0}{4}\Delta\varepsilon\tau \\ \tau &= \int \mathbf{E}^{\mathbf{t}\dagger}_{\boldsymbol{\mu}}\mathbf{E}^{\mathbf{z}}_{\boldsymbol{\nu}}dxdy \end{aligned}. \tag{2.24}$$

In the simplified case of pure TM mode the $\mathbf{E_Z}$ component is $\partial\mathbf{E_x}/\partial x$. The normalized field overlap integral, τ, as defined in (2.24) between the transverse component of TE mode and the longitudinal component of TM mode is not zero. Once we know κ, we can quickly calculate the power in TE and TM modes as $P_{\mathrm{TE}} = \cos^2\kappa L$ and $P_{\mathrm{TM}} = \sin^2\kappa L$, respectively using the well known "Coupled Mode Theory", assuming that there is no residual modal birefringence. L is the length of the IOC in the off-axis propagation case or the mode converter electrode length in the principal-axis propagation case. Remember that

there is a phase shift of $\pi/2$ between the transverse and the longitudinal components and hence the coupling coefficient κ is not real as in the case of transverse–transverse coupling, but it is imaginary in the case of transverse–longitudinal coupling.

For example, $\Delta\varepsilon = 0.0024$, $\tau = 0.248$, and $\kappa = 595.2\ \mathrm{m}^{-1}$ is obtained for $n_\mathrm{o} = \sqrt{\varepsilon_{11}} = \sqrt{\varepsilon_{22}} = 2.2125$ and $n_\mathrm{e} = \sqrt{\varepsilon_{33}} = 2.1446$ at $\lambda = 1550$ nm, $\theta = 2°$, and $L = 47$ mm. The respective power in TE and TM mode comes out to be 0.9128 and 0.0872. This well confirms the experimental results of 9–10 % static mode coupling that occurs between the TE and TM modes in the off-axis propagation case.

For the principal-axis propagation case, we use the basic equation of index ellipsoid

$$(\frac{1}{n_x^2} - r_{22}E_y^e)X^2 + (\frac{1}{n_y^2} + r_{22}E_y^e)Y^2 + (\frac{Z^2}{n_z^2}) + 2r_{51}E_y^eYZ = 1 \tag{2.25}$$

under the applied electrostatic field. The electric field is applied along Y-axis to compensate for the modal birefringence using $r_{12} = -r_{22}$. Indeed this equation also contains the term involving YZ and X, Y, Z are no longer the principal axes. To find the new principal axes, one need to eliminate the YZ term appearing in (2.25). This can be done by rotating the index ellipsoid by an angle

$$\theta^\mathrm{e} = \frac{1}{2}tan^{-1}\frac{2r_{51}E_y^\mathrm{e}}{(n_\mathrm{e}^{-2} - n_\mathrm{o}^{-2})} \tag{2.26}$$

in the YZ-plane using the rotation matrix given in (2.20).

If we apply, say, $V = (38 - (-38))\ \mathrm{V} = 76\ \mathrm{V}$ to compensate for the modal birefringence across a gap of $22\ \mu\mathrm{m}$ ($G = (10 + 6 + 6)\ \mu\mathrm{m}$), then we know the field strength $E_y^\mathrm{e} = V/G$ causes $\theta^\mathrm{e} = 0.4254°$. Angle θ^e replaces θ in (2.21) to get off-diagonal term $\Delta\varepsilon$, and $\Delta\varepsilon = 0.0005$. κ simply equals $114\ \mathrm{m}^{-1}$ as explained above for the off-axis propagation case, and hence we can calculate the amount of static polarization mode coupling in principal-axis propagation case.

The coupled modes μ and ν obey the coupled mode equations

$$\begin{aligned}\frac{\partial E_\mu(z)}{\partial z} &= \imath\kappa E_\mu e^{-2\imath\Delta\beta z}\\ \frac{\partial E_\nu(z)}{\partial z} &= \imath\kappa^* E_\nu e^{2\imath\Delta\beta z}\end{aligned}, \tag{2.27}$$

where κ is the coupling coefficient between the two modes and $\Delta\beta = (\beta_\mu - \beta_\nu)/2$ is phase mismatch parameter. Above coupled differential equation (2.27) reduces to

$$\begin{aligned}\frac{\partial \mathbf{E}}{\partial z} &= \tilde{\mathbf{M}}\mathbf{E}\\ \mathbf{E(z)} &= \begin{pmatrix} E_\mu e^{-\beta_\mu z} \\ E_\nu e^{-\beta_\nu z}\end{pmatrix}\end{aligned}, \tag{2.28}$$

with matrix $\tilde{\mathbf{M}}$ given by

$$\tilde{\mathbf{M}} = \imath\begin{pmatrix}\beta_\mu & \kappa^* \\ \kappa & \beta_\nu\end{pmatrix}. \tag{2.29}$$

A solution of the above coupled differential equations is assumed to be of the form

$$\mathbf{E}(\mathbf{z}) = \mathbf{E}(\mathbf{0})e^{\imath\gamma z} \tag{2.30}$$

and results in

$$\tilde{\mathbf{M}}\mathbf{E} = \imath\gamma\mathbf{E} \tag{2.31}$$

This is a standard matrix algebra eigenvalue problem, where $\mathbf{E}$ is the eigenvector and $\imath\gamma$ is the eigenvalue of the matrix $\tilde{\mathbf{M}}$. Since the coupling coefficient is imaginary, the supermodes of the waveguide or the eigensolution of the above coupled differential equations are therefore circularly polarized modes [52]

$$\begin{pmatrix} E^+ \\ E^- \end{pmatrix} = \frac{1}{\sqrt{2}} \begin{pmatrix} 1 \\ \pm\imath \end{pmatrix}, \tag{2.32}$$

and this confirms the speculations of Čtyroký [49].

Conclusion

The only option to reduce this undesired mode coupling is to fabricate optical waveguides along the principal axis. It is to be ensured that the waveguide is exactly parallel to the Z–axis during photolithography. Otherwise, the $LiNbO_3$ anisotropy will play the undesired role. Of course a relatively high V_B will result.

Whether one physically rotates the direction of propagation in the YZ-plane globally or rotates the index ellipsoid electrooptically in the YZ-plane locally, the net modal birefringence (typically 1.1×10^{-4}) compensation has the same effect. In this compensation process, one always ends up with the undesired imaginary coupling coefficient between the two orthogonally polarized modes, and this makes mode converters nonideal. If one compensates the modal birefringence globally then phenomenon is length-dependent and beyond any physical control due to the inherent $LiNbO_3$ anisotropy. If one compensates it locally then it is field–dependent. If the waveguide is exactly parallel to the Z–axis then the voltages required for the compensation are ideally symmetric, otherwise they are asymmetric in practice. This effect resembles more like a optical activity even though there are no optical active chiral molecules present in $LiNbO_3$ because it gives rise to an apparent circular birefringence when such devices are characterized using polarimeter. This phenomenon is found to be reciprocal because the waveguide itself is reciprocal.

25 mm long TE↔TM mode converter with a gap of 6 μm are designed, realized, and characterized for the mode conversion efficiency and voltage required for full mode conversion. TE-to-TM mode conversion efficiency is > 99 % and voltage required for full mode conversion is ≈ 10 V. Needed bias voltages were ± 38 V.

2.3.4 PI Temperature Controller

Temperature of the $LiNbO_3$-based IOC was kept constant during measurements in order to get repeatable and reproducible results, especially from phase shifters and mode converters.

This is because the $LiNbO_3$ has small but finite thermooptic coefficients ($\partial n/\partial t = +5.3 \times 10^{-5}$ for n_e and $\partial n/\partial t = +0.56 \times 10^{-5}$ for n_o) and it can cause the considerable refractive index change say 5×10^{-3} when the crystal temperature changes from room temperature to 100° C.

Therefore, a simple temperature controller based on proportional and integral control (PI) is designed and developed in-house, and is used to keep the temperature of the $LiNbO_3$-based IOC constant to say 25° C within $\pm 0.1^\circ$ C. It uses thermistor from Siemens which has a resistance of 10 kΩ at 25° C and a set of two Peltier elements from Melcor to either heat or cool the copper block on which the 80 mm long $LiNbO_3$-based IOC is mounted.

Figure 2.8 shows the photograph of the fiber pigtailed and packaged lithium niobate-based IOC. This device was fabricated by the Applied Physics group of Prof. W. Sohler, here at the University of Paderborn.

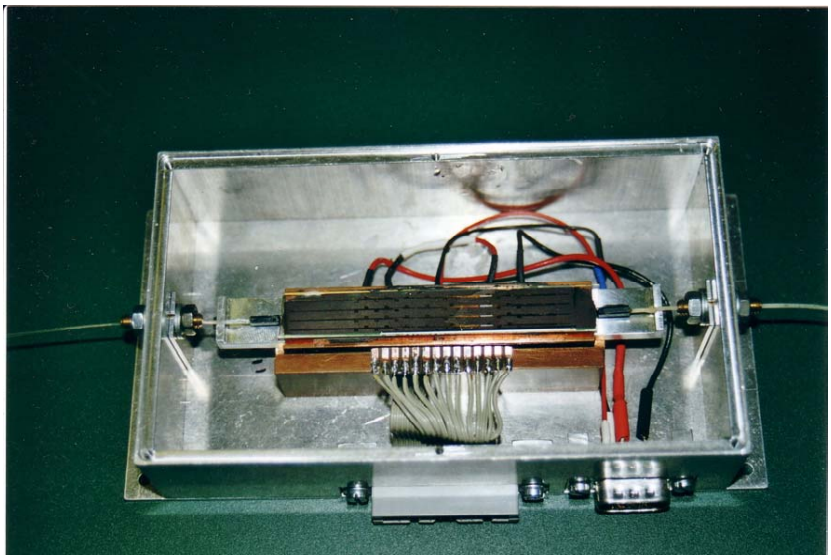

Figure 2.8: Photograph of the fiber pigtailed and packaged $LiNbO_3$-based IOC

2.4 The 3x3 Fiber Coupler

Use of 3x3 fused fiber optic coupler (FOC) as an interfering device, in the field of fiber sensors is becoming more popular. The advantage of 3x3 coupler is that the three output signals are available. The three output intensities are sinusoidal function of the optical path length difference between the any two arms of the interferometer. With the proper design of the 3x3 FOC, there exist a 120° phase difference between any two of the three output sinusoids. This phase difference can be exploited in electronic signal processing for avoiding the DC thermal drift and to generate two signals which are 90° out of phase with each other by taking the linear combinations of these three 3-phase output sinusoids. This in principle

allows us to perform more accurate phase measurement than a standard 2x2 coupler. This is because the conventional 2x2 coupler needs a nonreciprocal phase bias ($\pi/2$ rad), otherwise the sensitivity is zero at initial operating point. Another reason is as the differential phase ϕ fluctuates in the conventional 2x2 coupler causes corresponding fluctuations in the device sensitivity. Therefore 3x3 coupler is recommended over 2x2 coupler. Of course the performance of the interferometer depends sensitively on the characteristics of the 3x3 FOC. In principle the operation of the 3x3 FOC can be predicted using the "Coupled Mode Theory". In practice, the coupling coefficients and the required geometric parameters are neither known nor can be easily determined.

2.4.1 Analysis of 3x3 Fiber Coupler

Optical power transfer properties of the 3x3 FOC are characterized by the transfer matrix

$$\mathbf{M} = \begin{pmatrix} a & b & c \\ d & e & f \\ g & h & k \end{pmatrix}, \tag{2.33}$$

which itself is 3x3 [26]. There is a reference point for each input fiber lead and the each output fiber lead. The positions of these reference points can be so adjusted that the matrix elements a, b, c, d, and g are all real and positive numbers while e, f, h, and k are the complex numbers. Energy conservation principle results in

$$\mathbf{M}\mathbf{M}^{+} = \mathbf{M}^{+}\mathbf{M} = \mathbf{I}. \tag{2.34}$$

On expanding above equation into elemental equations, it is found that there are 9 conditions on the 13 parameters (one each for the real components, 2 each for the others). Therefore, 4 independent parameters e, f, g and h characterizes the optical power transfer properties of the 3x3 FOC. The convenient choices are the modulus of the complex parameter e, f, g and h. The elemental equations derived from above equation yields the real parameters as

$$\begin{aligned} a^2 &= e^2 + f^2 + h^2 + k^2 - 1 \\ b^2 &= 1 - e^2 - h^2 \\ c^2 &= 1 - k^2 - f^2 \\ d^2 &= 1 - e^2 - f^2 \\ g^2 &= 1 - k^2 - h^2 \end{aligned} \tag{2.35}$$

in terms of the modulus of $e,\ f,\ g$ and h. The phase of the complex elements

$$\begin{aligned}
\cos(\phi_{\mathrm{e}}) &= \frac{c^2f^2 - a^2d^2 - b^2e^2}{2adbe}, \quad \phi_{\mathrm{e}} > 0 \\
\cos(\phi_{\mathrm{f}}) &= \frac{b^2e^2 - a^2d^2 - c^2f^2}{2adcf}, \quad \phi_{\mathrm{f}} < 0 \\
\cos(\phi_{\mathrm{h}}) &= \frac{c^2k^2 - a^2g^2 - b^2h^2}{2agbh}, \quad \phi_{\mathrm{h}} < 0 \\
\cos(\phi_{\mathrm{k}}) &= \frac{b^2h^2 - a^2g^2 - c^2k^2}{2agck}, \quad \phi_{\mathrm{k}} > 0
\end{aligned} \tag{2.36}$$

can also be derived from the elemental equations. Note that these phases depend only on the modulus of the matrix elements of $\mathbf{M}$. The modulus of the matrix elements are directly related to the splitting ratios. For example, if the power is applied to the input arm 1 only, then powers measured at the three output arms will be in the ratio $a^2{:}b^2{:}c^2$. The modulus of all the elements of $\mathbf{M}$ can be determined in principle from the splitting ratio data.

In the case of the completely symmetric 3x3 coupler, the square of the modulus of each elements of $\mathbf{M}$ is equal to $1/3$. For this special case of symmetric coupler, $\phi_{\mathrm{f}} - \phi_{\mathrm{e}} = 120^\circ$ and $\phi_{\mathrm{k}} - \phi_{\mathrm{h}} = 120^\circ$. In summary, it has been shown that only 4 parameters are required to characterize the power transfer properties of the lossless 3x3 coupler. These parameters can be very easily obtained from the measurement of the splitting ratio data, and there exists a phase difference of 120° between any two outputs of the symmetric 3x3 coupler. It can also be shown in the next section 2.4.2 that how the performance of a fiber interferometer incorporating a 3x3 fiber coupler can be predicted from this splitting ratio data.

2.4.2 Basic MZI Using 3x3 Fiber Coupler

A typical all-fiber interferometer configuration is shown in the Figure 2.9. The interferometer is of a Mach-Zehnder type and is the fiber analog of the classical, bulk optic version of the Mach-Zehnder interferometer. It simply consist of the input 2x2 fiber coupler and the output 3x3 fiber coupler. The coherent single-mode laser source (both transverse and longitudinal modes) is used as a source in the MZI. The input light is then divided into two beams with nominal equal intensity by the input 2x2 fiber coupler (referred to as divider), part being sent through the measurement arm, the remainder through the reference arm. These two outputs, after passing through the measurement and reference arms, are recombined by the output 3x3 fiber coupler (referred to as recombiner). An interference signal between the two beams is then formed which, after propagating the length of the output fiber, is detected by the photodiodes.

Mathematically, the operation of such a interferometer can be described in terms of the product of transfer matrices (2.37) of each of the component used to construct the interferometer. First, 3x3 transfer matrix characterizes the output 3x3 fiber coupler. Second, transfer matrix characterizes both the reference and measurement arm of the interferometer. The ρ is the magnitude and can be set to 1 for this simplified case, and ϕ is phase difference

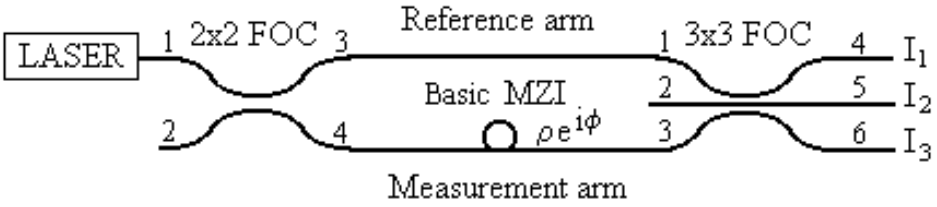

Figure 2.9: Basic Mach-Zehnder interferometer utilizing 3x3 fiber coupler

between the two arms of the interferometer. Third, transfer matrix characterizes the input 2x2 fiber coupler. Fourth, column vector characterizes the input signal P_{in} applied to this interferometer. Input power P_{in} can be set to 1 without the loss of generality.

$$\begin{pmatrix}\alpha\\ \beta\\ \gamma\end{pmatrix} = \begin{pmatrix}a & b & c\\ d & e & f\\ g & h & k\end{pmatrix}\begin{pmatrix}1 & 0 & 0\\ 0 & 0 & 0\\ 0 & 0 & \rho e^{\imath\phi}\end{pmatrix}\begin{pmatrix}A & 0 & B\\ 0 & 0 & 0\\ B & 0 & -A\end{pmatrix}\begin{pmatrix}\sqrt{P_{\text{in}}}\\ 0\\ 0\end{pmatrix} \tag{2.37}$$
$$a=b=c=d=e=f=g=h=k=\frac{1}{\sqrt{3}} \quad \text{and} \quad A=B=\frac{1}{\sqrt{2}}$$

α, β, γ characterizes the output amplitudes of the interferometer

$$\begin{aligned}\alpha &= \sqrt{P_{\text{in}}}(aA + cB\rho e^{\imath\phi})\\ \beta &= \sqrt{P_{\text{in}}}(dA + fB\rho e^{\imath\phi}).\\ \gamma &= \sqrt{P_{\text{in}}}(gA + kB\rho e^{\imath\phi})\end{aligned} \tag{2.38}$$

The output intensities I_1, I_2, and I_3 are given by

$$\begin{aligned}I_1 &= \alpha\alpha^* = P_{\text{in}}[a^2A^2 + c^2B^2 + 4aAcB\rho\cos(\phi)]\\ I_2 &= \beta\beta^* = P_{\text{in}}[d^2A^2 + f^2B^2 + 4dAfB\rho\cos(\phi + \frac{2\pi}{3})].\\ I_3 &= \gamma\gamma^* = P_{\text{in}}[g^2A^2 + k^2B^2 + 4gAkB\rho\cos(\phi - \frac{2\pi}{3})]\end{aligned} \tag{2.39}$$

$\pm 2\pi/3$ phase shifts are added due to the fact that the symmetric 3x3 fiber coupler has any two of its three output signals phase shifted by 120° with respect to each other.

$$I_{\text{ref}} = I_{\text{mes}} = a^2A^2 = c^2B^2 = d^2A^2 = f^2B^2 = g^2A^2 = k^2B^2 = \frac{1}{3}\cdot\frac{1}{2} = 0.1666 \tag{2.40}$$

Therefore, the output intensities now become

$$\begin{aligned}I_1 &= P_{\text{in}}[I_{\text{ref}} + I_{\text{mes}} + 4I_{\text{ref}}I_{\text{mes}}\rho\cos(\phi)]\\ I_2 &= P_{\text{in}}[I_{\text{ref}} + I_{\text{mes}} + 4I_{\text{ref}}I_{\text{mes}}\rho\cos(\phi + \frac{2\pi}{3})]\\ I_3 &= P_{\text{in}}[I_{\text{ref}} + I_{\text{mes}} + 4I_{\text{ref}}I_{\text{mes}}\rho\cos(\phi - \frac{2\pi}{3})].\end{aligned} \tag{2.41}$$

The output fringe visibility of the interferometer is given by

$$V = \frac{I_{\max} - I_{\min}}{I_{\max} + I_{\min}}. \tag{2.42}$$

It should be noted that two effects have been ignored in this calculations; the polarization effects and the effects of the finite source coherence length. Here it is assumed that only co-polarized signals interfere in output coupler. If one assumes a Lorentzian line shape, the normalized self-coherence function $\gamma(\tau)$ is given by $\gamma(\tau) = exp(-|\tau|/\tau_{\rm s})$, where τ is the differential propagation time delay between the measurement and reference optical paths and $\tau_{\rm s}$ is the source coherence time. Thus the actual value of V is a factor $\gamma(\tau)$ smaller than V itself. For this reason, the differential propagation delay between the measurement and reference fiber arms is usually adjusted to be much less than the source coherence time (i.e. $\tau \ll \tau_{\rm s}$); then $\gamma(\tau) \rightarrow 1$ and output fringe visibility equals V.

Two signals which are 90° out of phase with each other can be easily generated from the linear combinations of the three output intensities $I_1,\ I_2,\ \text{and}\ I_3$ as $2I_1 - I_2 - I_3$ and $I_2 - I_3$. For example, these two linear combinations yields

$$\begin{pmatrix} \mathrm{Re}(\rho) \\ \mathrm{Im}(\rho) \end{pmatrix} = \begin{pmatrix} \frac{2}{6} & -\frac{1}{6} & -\frac{1}{6} \\ 0 & \frac{1}{2\sqrt{3}} & -\frac{1}{2\sqrt{3}} \end{pmatrix} \begin{pmatrix} I_1 \\ I_2 \\ I_3 \end{pmatrix} \tag{2.43}$$

the real and imaginary part of the measured complex reflection coefficient ρ of the DUT's such as FBG's.

2.4.3 Advanced MZI Using $LiNbO_3$-based IOC and 3x3 Fiber Coupler

Figure 2.10 shows the advanced Mach-Zehnder interferometer configuration using integrated optical circuit based on X-cut, Z-propagation $LiNbO_3$ instead of the input 2x2 fiber coupler as shown in Figure 2.9 and the output 3x3 fiber coupler. This IOC utilizes 1x2 optical power splitter to split the input power in the ratio of 1:1 between the reference and measurement arms of the hybrid MZI. It also has two sets of electrooptic phase modulators on each arm of the interferometer which facilitates the digital phase shifting of the input signal in both arms of the MZI with respect to each other and a TE–TM mode converter which facilitates polarization change, under computer control.

The power transfer matrix of the input 2x2 fiber coupler is modified to take into account the facility of digital phase shifting. The signal in the reference arm may be phase shifted by the phase $\phi_{\rm r}$ while the signal in the measurement arm may be phase shifted by the phase $\phi_{\rm m}$. The operation of this hybrid MZI can be described once again in terms of the product of the transfer matrices (2.44) of each of the component used to construct this hybrid interferometer with the modified matrix for the input 2x2 fiber coupler which now

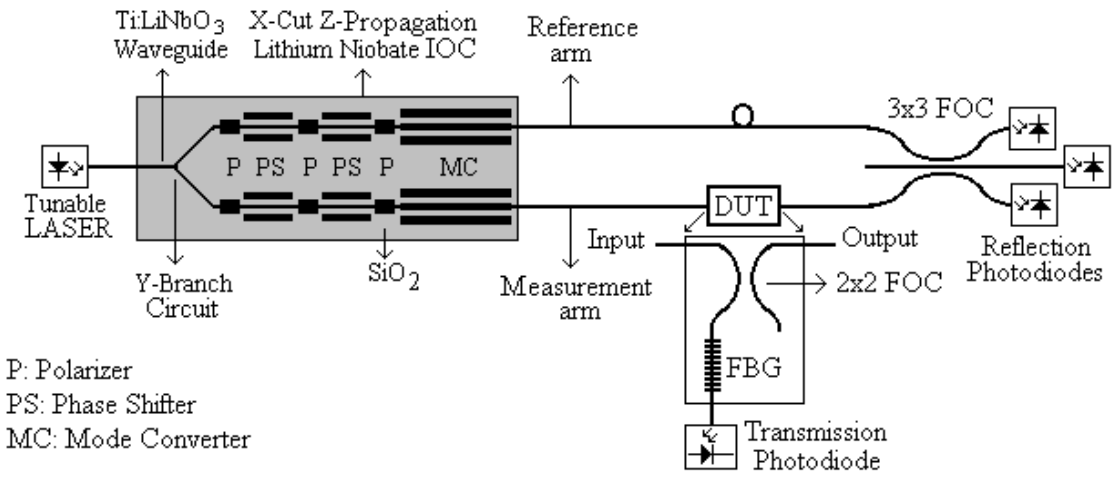

Figure 2.10: Measurement set-up, integrated optical network analyzer using $LiNbO_3$-based IOC and 3x3 fiber coupler

takes into account the possibility of digital phase shifting.

$$\begin{pmatrix}\alpha\\ \beta\\ \gamma\end{pmatrix} = \begin{pmatrix}a & b & c\\ d & e & f\\ g & h & k\end{pmatrix}\begin{pmatrix}1 & 0 & 0\\ 0 & 0 & 0\\ 0 & 0 & \rho e^{\imath\phi}\end{pmatrix}\begin{pmatrix}Ae^{\imath\phi_\mathrm{r}} & 0 & Be^{\imath\phi_\mathrm{m}}\\ 0 & 0 & 0\\ Be^{\imath\phi_\mathrm{m}} & 0 & -Ae^{\imath\phi_\mathrm{r}}\end{pmatrix}\begin{pmatrix}\sqrt{P_\mathrm{in}}\\ 0\\ 0\end{pmatrix} \tag{2.44}$$
$$a = b = c = d = e = f = g = h = k = \frac{1}{\sqrt{3}} \quad \text{and} \quad A = B = \frac{1}{\sqrt{2}}$$

$\alpha,\ \beta,\ \gamma$ characterizes the output amplitudes of the interferometer

$$\begin{aligned}\alpha &= \sqrt{P_\mathrm{in}}(aAe^{\imath\phi_\mathrm{r}} + cBe^{\imath\phi_\mathrm{m}}\rho e^{\imath\phi})\\ \beta &= \sqrt{P_\mathrm{in}}(dAe^{\imath\phi_\mathrm{r}} + fBe^{\imath\phi_\mathrm{m}}\rho e^{\imath\phi}).\\ \alpha &= \sqrt{P_\mathrm{in}}(gAe^{\imath\phi_\mathrm{r}} + kBe^{\imath\phi_\mathrm{m}}\rho e^{\imath\phi})\end{aligned} \tag{2.45}$$

The output intensities $I_1,\ I_2,$ and I_3 are given by

$$\begin{aligned}I_1 &= \alpha\alpha^{*}{=}P_\mathrm{in}[a^2A^2 + c^2B^2 + 4aAcB\rho\cos(\phi_\mathrm{r} - \phi_\mathrm{m} - \phi)]\\ I_2 &= \beta\beta^{*}{=}P_\mathrm{in}[d^2A^2 + f^2B^2 + 4dAfB\rho\cos(\phi_\mathrm{r} - \phi_\mathrm{m} - \phi + \frac{2\pi}{3})].\\ I_3 &= \gamma\gamma^{*}{=}P_\mathrm{in}[g^2A^2 + k^2B^2 + 4gAkB\rho\cos(\phi_\mathrm{r} - \phi_\mathrm{m} - \phi - \frac{2\pi}{3})]\end{aligned} \tag{2.46}$$

$\pm 2\pi/3$ phase shifts are added due to the fact that the symmetric 3x3 coupler has any two of its three output signals phase shifted by 120° with respect to each other.

$$I_\mathrm{ref} = I_\mathrm{mes} = a^2A^2 = c^2B^2 = d^2A^2 = f^2B^2 = g^2A^2 = k^2B^2 = \frac{1}{3}\cdot\frac{1}{2} = 0.1666 \tag{2.47}$$

Therefore, the output intensities now become

$$\begin{aligned} I_1 &= P_{\mathrm{in}}[I_{\mathrm{ref}} + I_{\mathrm{mes}} + 4I_{\mathrm{ref}}I_{\mathrm{mes}}\rho\cos(\phi_{\mathrm{r}} - \phi_{\mathrm{m}} - \phi)] \\ I_2 &= P_{\mathrm{in}}[I_{\mathrm{ref}} + I_{\mathrm{mes}} + 4I_{\mathrm{ref}}I_{\mathrm{mes}}\rho\cos(\phi_{\mathrm{r}} - \phi_{\mathrm{m}} - \phi + \frac{2\pi}{3})]. \\ I_3 &= P_{\mathrm{in}}[I_{\mathrm{ref}} + I_{\mathrm{mes}} + 4I_{\mathrm{ref}}I_{\mathrm{mes}}\rho\cos(\phi_{\mathrm{r}} - \phi_{\mathrm{m}} - \phi - \frac{2\pi}{3})] \end{aligned} \tag{2.48}$$

Phase angle ϕ_{r} is set to $-\pi/2$, 0, $\pi/2$, π while phase angle ϕ_{m} is set to $-3\pi/4$ $-\pi/4$ $\pi/4$, $3\pi/4$, respectively. There are 16 linear combinations of these 4 phase shifts ϕ_{r} and ϕ_{m}, which are successively applied to interferometer. This fact can be exploited to generate two signals which are 90° out of phase with each other using

$$\begin{aligned} \mathrm{Re}(\rho) &= \frac{3}{8}\sum_{k=1}^{4}\sum_{j=1}^{4}\sum_{i=1}^{3} I_i\cos(\phi_{\mathrm{c}_i} + \phi_{\mathrm{r}_j} - \phi_{\mathrm{m}_k} - \phi) \\ \mathrm{Im}(\rho) &= \frac{3}{8}\sum_{k=1}^{4}\sum_{j=1}^{4}\sum_{i=1}^{3} I_i\cos(\phi_{\mathrm{c}_i} + \phi_{\mathrm{r}_j} - \phi_{\mathrm{m}_k} - \phi - \frac{\pi}{2}) \end{aligned} . \tag{2.49}$$

The phase angle ϕ_{c} in (2.49) takes into account the phase difference introduced by the output 3x3 fiber coupler and is either set to 0 or $2\pi/3$ or $-2\pi/3$. Index i represents the intensities at the output of the 3x3 coupler and goes from 1 to 3 while index j and k represents the phase angles ϕ_{r_j} and ϕ_{m_k}, and both the indexes goes from 1 to 4. For example, this again gives the real part and imaginary part of the measured quantity using this interferometer such as a complex reflection coefficient ρ of the DUT's such as FBG's.

The advantage of this technique is that the DC thermal drift in the fiber interferometers could be avoided to some extent. This is because the digital phase shifting is done electrooptically using the $LiNbO_3$-based IOC which has typically a response time of 1 ns and the very fast measurements are possible in principle. This is a kind of AC measurements where we change the optical path lengths in both arms of the interferometer in a predetermined manner and sample the data so that the effects of power fluctuations could be averaged out.

2.5 Conclusion

In summary, the measurement setup of an integrated optical network analyzer is developed using fiber and the lithium niobate based integrated optical circuit. The basic integrated optical components such as polarizers, phase modulators, and TE↔TM mode converters are all integrated on to a single IOC to get more functionality. Each of these basic integrated optical components are designed, fabricated, and characterized independently so as to get an optimum performance before integration. The integrated optical network analyzer is also interfaced to a computer system. Analog–to–digital converters are used for data acquisition. Digital–to–analog converters are used to drive phase modulator, TE↔TM mode converter,

and programmable constant current source which is interfaced to tuneable DFB laser diode, under computer control. Proportional integral temperature controller is implemented to keep the temperature constant of the integrated optical network analyzer circuit. Finally, the operation of basic and advanced Mach-Zehnder interferometer using fiber and integrated optics is explained. Moreover, the use of digital phase shifters to implement AC rather than DC measurement is described.

Chapter 3

Longitudinal Structure Characterization of FBG

3.1 Fiber Bragg Gratings: An Introduction

Fiber Bragg gratings represent a key element in the established fields of optical communications, optoelectronics, and optical sensors. Bragg Gratings allows to implement various primary functions such as reflection, diffraction, and filtering in a highly efficient, low-loss manner in single-mode optical fibers. Their unique filtering properties and versatility as in-fiber component is illustrated by their use in a wavelength stabilized semiconductor lasers, fiber lasers, tuneable wavelength filters, optical fiber polarization mode converters, gain equalizers for Erbium Doped Fiber Amplifiers (EDFA), to improve the pump efficiency of EDFA's, dispersion compensators, wavelength division multiplexers and demultiplexers, add or drop multiplexers, and optical sensors etc. These are comparatively simple device and in their most basic form consists of a periodic modulation of the index of refraction along the fiber core. Different types of fiber Bragg gratings are proposed and realized depending on the function and hence by refractive index modulation. These includes uniform, nonuniform, chirped, apodized, and blazed gratings.

Nobel Laureates Sir W. H. Bragg (1862–1942) and his son Sir W. L. Bragg (1890–1971) discovered the well known Bragg diffraction condition ($2\Lambda \sin\Theta = n\lambda$), in 1913, for the X-ray diffraction from the periodic crystal lattice. Diffraction can be considered as a reflection of the incident X-ray beam from a series of lattice planes. In the Bragg condition, Λ is the periodicity of the atomic planes, Θ is the angle of incidence, λ is the wavelength of X-rays, and n is the order of diffraction. For $\Theta = 90^\circ$ and $n = 1$, the Bragg diffraction condition simplifies to $2\Lambda = \lambda$. The periode Λ of the refractive index modulation of an optical fiber Bragg grating is set equal to half of the wavelength λ of the light propagating in the fiber. It is this phase matching condition between the grating planes and incident light that results in coherent back reflection. Reflectivities approaching 100 % are possible with grating bandwidth ($\Delta\lambda$) tailored from 0.1 nm to in excess of 100 nm.

Figure 3.1 shows the uniform fiber Bragg grating along with the incident, diffracted,

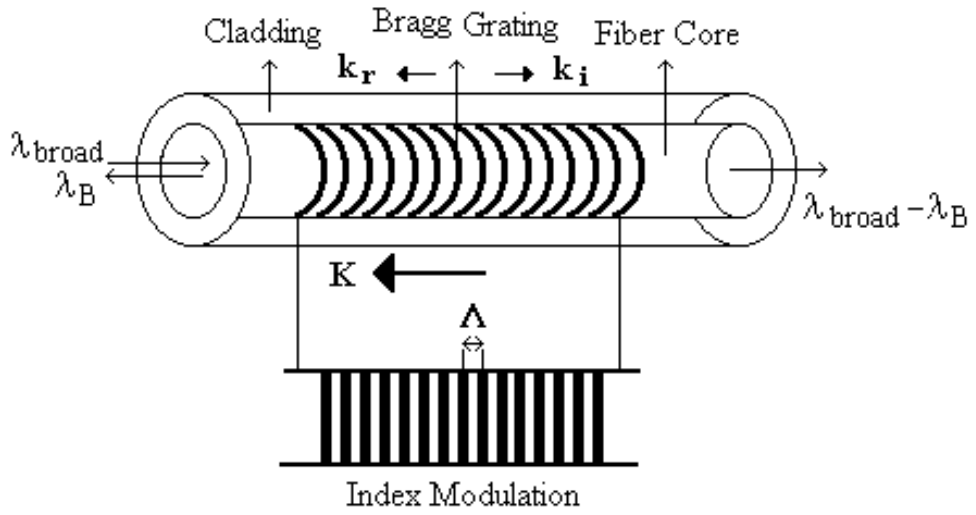

Figure 3.1: Illustration of a uniform grating with constant amplitude of refractive index modulation and grating period

and grating wavevectors. The Bragg condition is simply the requirement that satisfies both energy and momentum conservation principles. The energy conservation principle ($\hbar\omega_i = \hbar\omega_r$) requires that the frequency of the incident and the reflected light must be the same. The momentum conservation principle requires that the incident wavevector, $\mathbf{k_i}$, plus the grating wavevector, $\mathbf{K}$, equal the wavevector of the scattered radiation, $\mathbf{k_r}$. This would mean

$$\mathbf{k_i} + \mathbf{K} = \mathbf{k_r}, \tag{3.1}$$

where the grating wavevector, $\mathbf{K}$, has a direction normal to the grating planes with a magnitude $2\pi/\Lambda$. The diffracted wavevector is equal in magnitude, but opposite in direction to the incident wavevector. Therefore, the momentum conservation principle

$$2(\frac{2\pi n_0}{\lambda_B}) = \frac{2\pi}{\Lambda}, \tag{3.2}$$

simplifies to first order Bragg diffraction condition

$$\lambda_B = 2n_0\Lambda, \tag{3.3}$$

where the Bragg wavelength, λ_B, is the free space center wavelength of the input light that will be reflected back from the Bragg grating, and n_0 is the effective refractive index of the fiber core at the free space center wavelength.

Figure 3.2 shows the grating structure and physical grating parameters that determines the spectral response of the optical fiber Bragg gratings. The refractive index modulation $n(z)$ of the Bragg grating is written as

$$n(z) = n_0 + \frac{1}{2}\Delta n_{\mathrm{pp}}(z)\cos(\frac{2\pi}{\Lambda}z + \phi(z)), \tag{3.4}$$

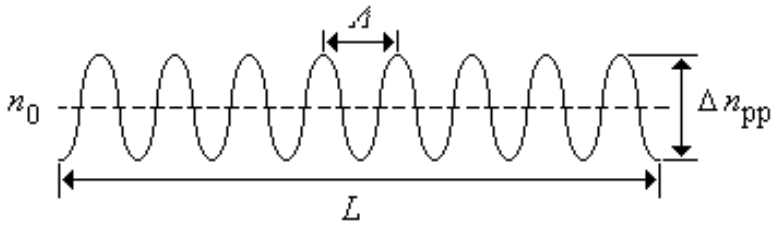

Figure 3.2: Illustration of peak to peak refractive index modulation Δn_{pp} and grating period Λ

where $\Delta n_{\mathrm{pp}}(z)$ is the gratings peak to peak refractive index modulation amplitude (typical values 10^{-5} to 10^{-3}), and $\phi(z)$ is the grating phase. L is the grating length, and z is the distance along the fiber longitudinal-axis. Using the "Coupled Mode Theory" of Lam and Garside [53] that described the reflection properties of Bragg grating, reflectivity and transmissivity of a uniform fiber Bragg grating with constant refractive index modulation amplitude and period is given by the following expressions:

$$\begin{aligned} R(L,\lambda) &= \frac{\kappa^2 \sinh^2(sL)}{\Delta k^2 \sinh^2(sL) + s^2 \cosh^2(sL)} \\ T(L,\lambda) &= \frac{\kappa^2}{\Delta k^2 \sinh^2(sL) + s^2 \cosh^2(sL)} \end{aligned}, \tag{3.5}$$

where $R(L,\lambda)$ and $T(L,\lambda)$ is reflectivity and transmissivity as a function of grating length L and the incident wavelength λ. κ is the coupling coefficient, $\Delta k = k - \pi/\lambda$ is the detuning wavevector, $k = (2\pi/\lambda)n_0$ is the propagation constant, and $s^2 = \kappa^2 - \Delta k^2$. Gratings local coupling coefficient, $\kappa(z)$, is directly proportional to the peak refractive index modulation amplitude, Δn, and may be written as

$$\kappa(z) = \frac{\pi \Delta n(z)}{\lambda_{\mathrm{B}}} M_{\mathrm{P}}, \tag{3.6}$$

where M_{p} is the fraction of the fiber mode power contained by the fibre core. On the basis that the grating is uniformly written through the fibre core, M_{p} can be approximated by $1 - V^{-2}$, where V is the normalized frequency of the fiber. $V = (2\pi/\lambda)d\sqrt{n_{\mathrm{co}}^2 - n_{\mathrm{cl}}^2}$ where d is radius of the fiber core, n_{co} and n_{cl} are the core and cladding refractive indices, respectively. The product κL gives the grating strength. At the Bragg gratings center wavelength, λ_{B}, there is no wavevector detuning and $\Delta k = 0$; therefore, the expressions for peak reflection and peak transmission of the uniform fiber gratings simplifies to

$$\begin{aligned} R(L,\lambda_{\mathrm{B}}) &= \tanh^2 \kappa L \\ T(L,\lambda_{\mathrm{B}}) &= \operatorname{sech}^2 \kappa L \end{aligned}. \tag{3.7}$$

Depending on the application, fiber Bragg gratings with varying periods and as well as depths of refractive index modulation have been proposed and fabricated. To what extent

the specific fiber Bragg grating design and the actual fabricated device correspond to each other has to be checked by the suitable characterization methods. So far very few studies have been done in an area of reconstructing the longitudinal grating structure from the experimental data. Here we would like to apply the concepts of optical network analysis in order to efficiently characterize the fiber Bragg gratings and at the same time we would like to demonstrate the versatility and functionality of the lithium niobate-based integrated optical network analyzer.

3.2 Longitudinal Structure Characterization of FBG

Scalar characterization is the fastest and simplest method to characterize optical fiber Bragg gratings for longitudinal structure characterization. To perform this, we need to correctly measure either the frequency-dependent complex reflection or transmission coefficients of the FBG in the frequency domain and then use the inverse Fourier transform to get the time domain impulse response of the FBG. From the latter, the longitudinal grating structure could be determined either by using the inverse scattering algorithms or by using layer-peeling methods [54, 55].

3.2.1 Measurement of Complex Reflection Coefficient

Optical frequency domain interferometry was used to measure the frequency-dependent complex reflection coefficient $\rho(f)$. The optical frequency is scanned symmetrically over ≈ 50 GHz optical bandwidth with the Bragg wavelength ($\lambda_{\mathrm{B}} = 1548.25\ \mathrm{nm}$) being at the scan center, of a given FBG under test. The DFB laser diode was used as a tuneable laser source with a resolution of ≈ 25 MHz. Number of measurement points n were equal to the m^{th} power of 2 and m was set to 11, i.e 2048 points.

Thermal noise ultimately represents the fundamental noise limit in fiber-optic interferometric sensors which affects the signal-to-noise ratio (SNR) of the measurement system. Thermal processes in the fiber modulate the refractive index of the fiber which again causes phase modulation of the signals propagating in the fiber. There are two basic causes of refractive index modulation, namely, temperature and density fluctuations. The former dominate at low frequencies while later dominate at high frequencies with a cross-over point of 1 MHz. The frequency range of interest for most fiber sensor applications is below 1 MHz and therefore, in that frequency interval, it is the temperature fluctuations that ultimately limits the signal-to-noise ratio of the system [56, 57]. In a MZI, the signals in the two arms are exposed to two different random processes, and both arms contribute to the thermally induced phase noise. Therefore, very fast measurements must be done in order to combat the thermal drift in the fiber-optic interferometers. The measurements are done using the programmable constant current source and the DFB laser diode which is used as a narrowband tuneable laser source. Typical tuning slope is of the order of ≈ 10 pm/mA of pump current. This static wavelength shift also affects the laser power. The optical power received by all photodiodes in the measurement setup, therefore, must

be normalized. This power normalization, for example, can be achieved by monitoring the laser power as function of frequency by means of an additional 10 dB coupler connected to the power monitor photodiode. The transmission coefficient $\tau(f)$ of the FBG is given by $\sqrt{I_4/I_8}$. Two linear combinations of the three three-phase photocurrents yields the real and imaginary parts of the frequency-dependent complex reflection coefficient $\rho(f)$ of the FBG under test as $2I_1 - I_2 - I_3$ and $I_2 - I_3$, respectively, as described in section 2.4.2.

3.2.2 Calculation of Impulse Response

The frequency-dependent complex reflection coefficient $\rho(f)$ and the real transmission coefficient $\tau(f)$ of FBG under test must satisfy the lossless relation

$$R + T \leq 1 \tag{3.8}$$

in frequency domain where the reflectivity and the transmissivity of the FBG is given by $R = |\rho(f)|^2$ and $T = |\tau(f)|^2$, respectively.

The frequencies obtained from the reference interferometer were used to resample (linearly interpolate) both magnitude and argument of the measured frequency-dependent complex reflection coefficient, independently, so that, this frequency correction creates an accurate and equidistant frequency grid for inverse Fourier transform which enables us to calculate the impulse response,

$$h(t) \Longleftrightarrow \rho(f), \tag{3.9}$$

of the DUT. This inverse Fourier transform is calculated using the standard Inverse Fast Fourier Transform algorithm (IFFT). For the inverse Fourier transform, the number of Fourier steps $N = 2^{12} = 4096$. Therefore, we shift $\rho(f)$ so that it is at the center in the frequency domain. The First and the last 1024 points are padded with 0's, so that the total number of Fourier steps N equals 4096 together with $\rho(f)$ sampled at 2048 points. The frequency domain results were multiplied by a $\cos^2$ window to suppress errors introduced by the discontinuous borders. This scheme is implemented due to the fact that 62.5 GHz (≈ 0.5 nm at 1550 nm) is scanned in the frequency domain and we wanted to convert it to 125 GHz, so that, the corresponding time step becomes

$$\Delta t = \frac{1}{N \cdot \Delta f} = \frac{1}{125\ \mathrm{GHz}} = 8\ \mathrm{ps}. \tag{3.10}$$

This time step is equal to the reciprocal of the product of the number of Fourier steps N and the corresponding frequency step Δf used during the measurement of $\rho(f)$, in the frequency domain. Once the impulse response of the Bragg grating under test is known accurately in the time domain, then the job of calculating the longitudinal grating structure is straightforward.

3.2.3 Calculation of Longitudinal Grating Structure

A second order differential equation governing two independent state variables one dimensional (1-D) space coordinate, z, and time, t,

$$\frac{\partial^2 E}{\partial z^2} = \frac{1}{c^2}\frac{\partial^2 E}{\partial t^2}, \tag{3.11}$$

generally, characterizes the propagation of electromagnetic waves, in the medium with constant material parameters. The solutions of (3.11) are the waves having electric field E propagating with speed c along the $\pm z$-direction. Our aim is to know what happens when an electromagnetic wave propagates in a medium (single mode fiber) with constant material parameters (refractive index) and then the wave suddenly encounters an abrupt change, or a discontinuity in the material parameters of the medium such as a periodic refractive index change (fiber Bragg grating) as a function of z. This is an ideal case for inverse problems. In inverse problems, the unknown properties of the medium are found out by applying some input (say a delta function $\delta(t)$) to the medium and measuring some output (impulse response $h(t)$). A pair of first-order coupled differential equations, as derived in the Appendix C,

$$\begin{aligned} (\frac{\partial}{\partial z} + \frac{n_o}{c}\frac{\partial}{\partial t})\mathbf{D}(z,t) &= \kappa^*(z)\mathbf{U}(z,t) \\ (\frac{\partial}{\partial z} - \frac{n_o}{c}\frac{\partial}{\partial t})\mathbf{U}(z,t) &= \kappa(z)\mathbf{D}(z,t) \end{aligned}, \tag{3.12}$$

where $\mathbf{D}$ is the electric field matrix of the forward (Down), and $\mathbf{U}$ is the electric field matrix of the backward (Up) propagating waves that governs the propagation of an electromagnetic waves in time t and 1-D space coordinate z for such a medium. $\kappa(z)$ in (3.12) is the coupling coefficient between the forward and backward propagating waves. When the system parameter such as refractive index do not vary with 1-D space coordinate z, then $\kappa(z) = 0$ and the above two first-order coupled differential equations decouples. The physical meaning of the decoupling of $\mathbf{D}$ and $\mathbf{U}$ is that the two waves do not interact. When the refractive index changes either continuously or discontinuously, then the $\mathbf{D}$ and $\mathbf{U}$ waves do interact. These waves had the property that they do not interact unless there is a change in the value of at least one of the material parameters of the medium. It is this interaction that complicates the problem of transmission and reflection of electromagnetic waves from the medium with periodically varying refractive index change such as the Bragg gratings in fibers. Therefore we need to analyze the waves in two situations:
(1) as they travel along the region where material parameter is constant;
(2) as they cross the region where material parameter is discontinuous.

Inverse problem assumes that the systems impulse response $\mathbf{U}_{0,t} = h(t)$ is known in addition to the given Dirac impulse $\mathbf{D}_{0,t} = 1\delta(t)$. It is assumed that the output, $\mathbf{U}_{0,t}$ (impulse response) is caused by the input, $\mathbf{D}_{0,t}$ (delta function) by the fundamental concept of casualty. Principle of casualty states that the cause must precede the effect. Therefore, it is possible to find the whole casual solutions $\mathbf{D}_{\mu,\nu}$, $\mathbf{U}_{\mu,\nu}$, and in addition, be able to

find $\kappa(z)$. In order to calculate $\kappa(z)$, we discretize (3.12) using a time step Δt and a corresponding position step $\Delta z = (c/n_o)\Delta t$. A pair of discrete equations

$$\begin{aligned} \mathbf{D}_{\mu,\nu} &= \tau_{\mu-1}^{-1}(k_{\mu-1}^{*}\mathbf{U}_{\mu-1,\nu+1} + \mathbf{D}_{\mu-1,\nu-1}) \\ \mathbf{U}_{\mu,\nu} &= \tau_{\mu-1}^{-1}(\mathbf{U}_{\mu-1,\nu+1} + k_{\mu-1}\mathbf{D}_{\mu-1,\nu-1}) \end{aligned} \tag{3.13}$$

are derived from the piecewise solutions of (3.12) under the assumption of locally constant $k = \kappa\Delta z$ as derived in Appendix D.

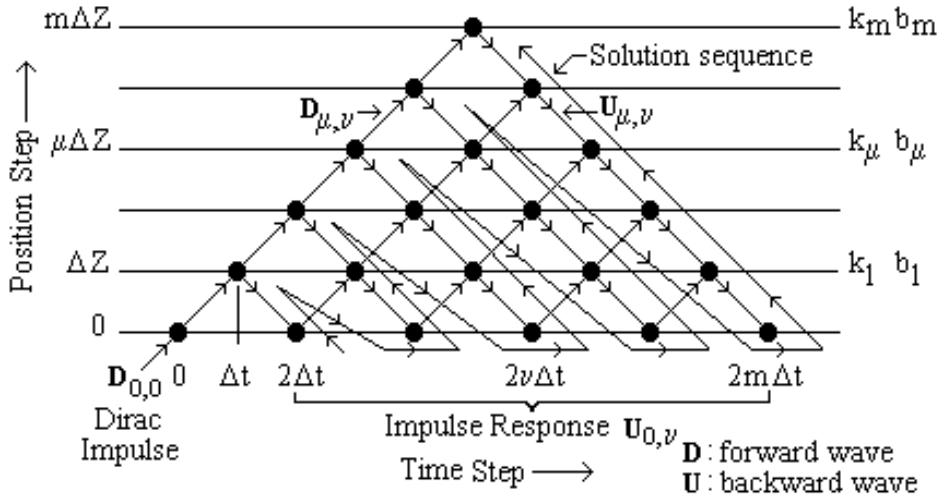

Figure 3.3: Wave propagation and solution sequence for inverse scattering algorithm

Figure 3.3 shows wave propagation and solution sequence given by dashed arrow in a grid of time and space. Solution starts from the knowledge of incident unity matrix $\mathbf{D}_{0,0}$ (the only nonzero component of a discretized $\mathbf{D}_{0,t} = 1\delta(t)$) and the measured impulse response matrix $\mathbf{U}_{0,\nu}$ (discretized $\mathbf{U}_{0,t} = h(t)$). Waves $\mathbf{D}_{\mu,\nu}$, $\mathbf{U}_{\mu,\nu}$ and as far as yet unknown matrix $\kappa(z)$ are calculated in a sequence given by the dashed arrow.

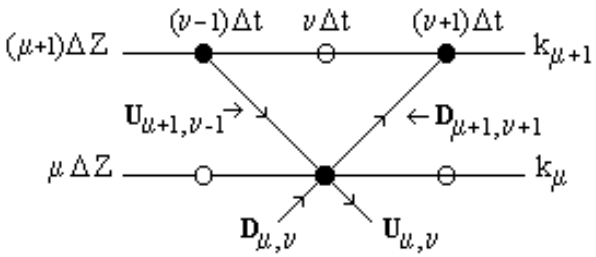

Figure 3.4: Calculation of $\mathbf{D}_{\mu,\nu}$ and $\mathbf{U}_{\mu,\nu}$ for one position step ΔZ

Mathematically speaking for calculation of k_m, all k_μ with $0 < \mu < m$ must be known. This is automatically the case if one starts with $m = 1$. Each solution steps then requires (3.13) to be solved successively for $\mu = 1 \cdots m$, $\nu = 2m$.

Figure 3.4 shows the quantities required to calculate $\mathbf{D}_{\mu,\nu}$ and $\mathbf{U}_{\mu,\nu}$ for one position step ΔZ. The transmission coefficient τ_μ and the coupling coefficient k_μ in (3.13) is given by

$$\begin{aligned} \tau_\mu &= \sqrt{1-|k_\mu|^2} \\ k_\mu &= -\frac{\mathbf{U}_{\mu,\mu}}{\mathbf{D}_{\mu,\mu}} \end{aligned} \quad . \tag{3.14}$$

The refractive index modulation $\Delta n(z)$ which is directly proportional to the complex coupling coefficient $\kappa(z)$ of the FBG under test is

$$\Delta n(z) = \frac{\lambda_{\mathrm{B}}}{\pi}\kappa(z) \quad \text{where} \quad \kappa(z) = \frac{k_\mu}{\Delta z}. \tag{3.15}$$

Therefore peak to peak amplitude and phase of the refractive index modulation equals

$$\begin{aligned} \Delta n_{\mathrm{pp}}(z) &= 2 \cdot \Delta n(z) \\ \arg[\Delta n_{\mathrm{pp}}(z)] &= \arg[k_\mu] - \frac{\pi}{2}. \end{aligned} \tag{3.16}$$

3.2.4 Scalar Measurements

Fiber Bragg grating of reflectivity $> 95\%$ and $\Delta\lambda \approx 0.2$ nm at $\lambda_{\mathrm{B}} = 1548.25$ nm, is used as an object for the longitudinal structure characterization, in forward as well as backward direction. Temperature of the fiber Bragg grating is kept constant during experiment by mounting it on to an aluminium plate whose temperature is sensed using a thermistor and kept constant using a set of Peltier elements and a simple proportional integral temperature controller. For scalar measurement, the manual polarization controllers (in Figure 2.1) are adjusted for the maximum interference contrast assuming that only co-polarized waves interferes in the output 3x3 fiber coupler of the measurement interferometer. As it has been mentioned in section 3.2.1, the optical frequency is symmetrically scanned to measure the complex reflection coefficient $\rho(f)$ at 2048 points. The inverse Fourier transform and inverse scattering algorithm mentioned in section 3.2.2 and 3.2.3 are used to determine the longitudinal grating structure. Results for the forward as well as backward measurement are summarized below.

Forward Measurement

Figure 3.5(a) shows the magnitude of the measured frequency-dependent complex reflection coefficient $|\rho(f)|$ while Figure 3.5(b) shows the magnitude of the scalar transmission coefficient $|\tau(f)|$ of the FBG in forward direction.

Figure 3.6(a) shows the impulse response $h(t)$ while Figure 3.6(b) shows the longitudinal grating structure $\Delta n(z)$ with a corresponding grating burst for this FBG in forward direction.

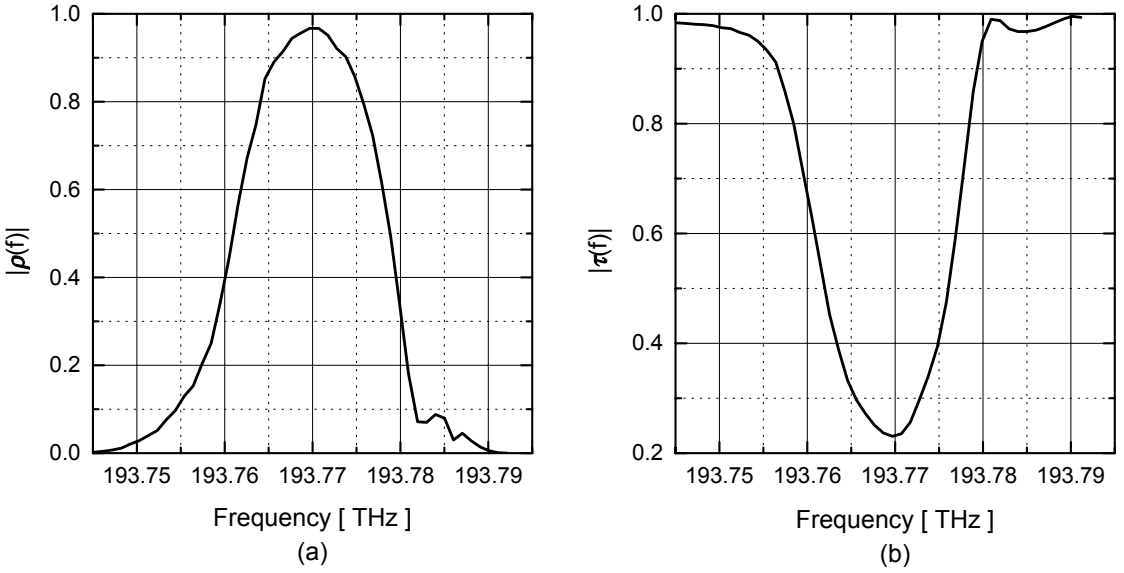

Figure 3.5: (a) Complex reflection coefficient $|\rho(f)|$ and (b) scalar transmission coefficient $|\tau(f)|$ of this FBG in forward direction

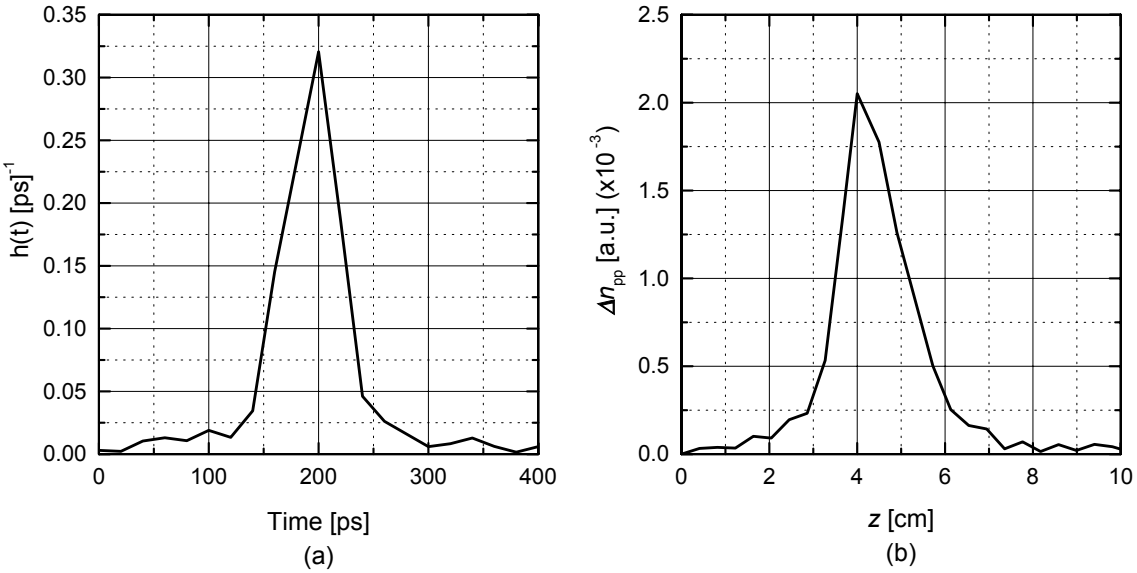

Figure 3.6: (a) Impulse response $h(t)$ and (b) longitudinal grating structure $\Delta n(z)$ of this FBG in forward direction

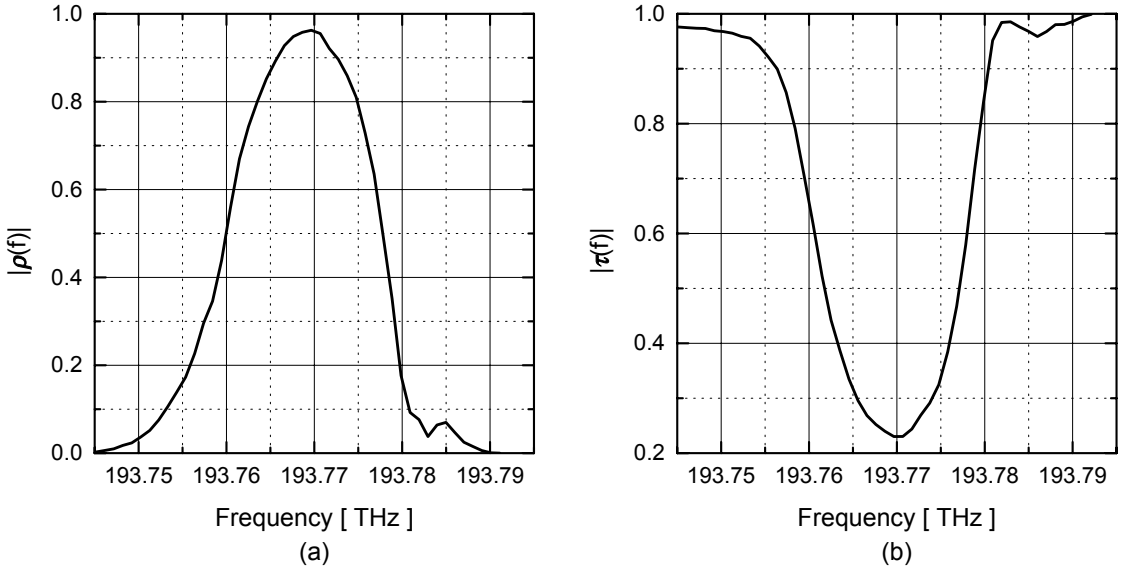

Figure 3.7: (a) Complex reflection coefficient $|\rho(f)|$ and (b) scalar transmission coefficient $|\tau(f)|$ of this FBG in backward direction

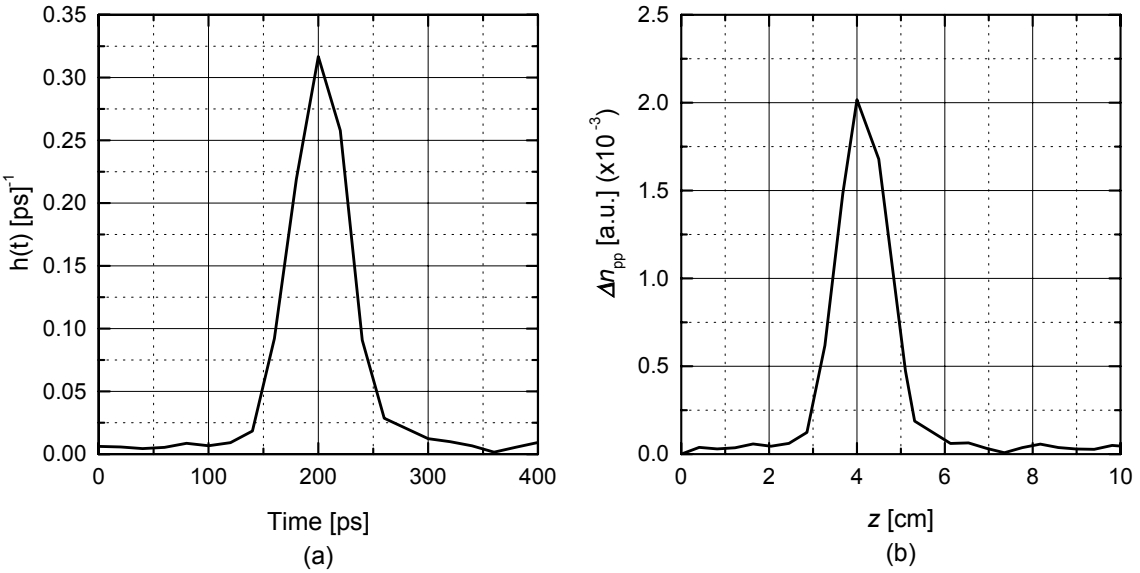

Figure 3.8: (a) Impulse response $h(t)$ and (b) longitudinal grating structure $\Delta n(z)$ of this FBG in backward direction

Backward Measurement

Figure 3.7(a) shows the magnitude of the measured frequency-dependent complex reflection coefficient $|\rho(f)|$ while Figure 3.7(b) shows the magnitude of the scalar transmission coefficient $|\tau(f)|$ of the FBG in backward direction.

Figure 3.8(a) shows the impulse response $h(t)$ while Figure 3.8(b) shows the longitudinal grating structure $\Delta n(z)$ with a corresponding grating burst for this FBG in backward direction.

Conclusion

This validates the measurement principle and grating structure since "forward" and "backward" measurement results agree very well. This grating is a very strong one and has a single burst in its longitudinal grating structure.

3.3 Vectorial Structure Characterization of FBG

Grating behavior is dependent on polarization, at least when the period of a grating and wavelength of the incident light are of the same order. Consequently the best scalar theories are often unable to predict the efficiencies of modern gratings since they have not taken the vectorial character of light into account. During the last decade, new techniques have been derived from Maxwell's equations [58]. One of the method that is used here is briefly outlined, then studied in grater depth and applied for the vectorial structure characterization of fiber sensor grating.

3.3.1 Concept of Birefringence and Dichroism

The propagation of monochromatic plane electromagnetic waves in an infinite isotropic dielectric media is characterized by their refractive index n. For a monochromatic plane wave with an angular frequency ω, the wave vector of the plane wave is $\mathbf{k} = (n\omega/c)\widehat{\mathbf{u}}$, where $\widehat{\mathbf{u}}$ is a unit vector. The plane wave is related to a notion of light ray whose direction is given by the direction of the Poynting vector $\mathbf{S} = \mathbf{E} \times \mathbf{H}$. In isotropic media the vectors $\mathbf{k}$ and $\mathbf{S}$ are parallel no matter what the direction of propagation is. In general, this does not hold true for anisotropic media.

Generally, optical properties of an anisotropic dielectric medium are determined by its refractive index, as seen by a plane electromagnetic wave passing through it and depend on its direction of propagation $\widehat{\mathbf{u}}$. In fact, it can be shown, for a given direction of propagation, that two refractive indices may co-exist. The latter are associated with electromagnetic waves having states of polarization that can propagate without any alteration. These particular states of polarization are called eigenstates for the considered direction of propagation.

Usually, two different kinds of optical anisotropy can be considered:

–The linear anisotropy, whose eigenstates of propagation are the linear states of polarization.
–The circular anisotropy, whose eigenstates of propagation are the circular states of polarization.
–These two kinds of anisotropy can coexist in the media and in such a case, the eigenstates of polarization are in general elliptical.

Whenever an electromagnetic wave passes through a material medium, it induces an electric polarization $\mathbf{P}^1$ which is added to the vacuum polarization $\mathbf{P}^0$, defined by: $\mathbf{P}^0 = \varepsilon_0\mathbf{E}$. The total polarization $\mathbf{P} = \mathbf{P}^0 + \mathbf{P}^1$ is represented by a vectorial function $\mathbf{P}(\mathbf{E})$, where $\mathbf{E}$ is the exciting field of the electromagnetic wave. Thus, in the approximation of low electric field intensities, the induced polarization

$$\mathbf{P}^1 = \varepsilon_0[\boldsymbol{\chi}]\mathbf{E} \tag{3.17}$$

is a linear function of $\mathbf{E}$ where $[\boldsymbol{\chi}]$ is the first-order electric susceptibility tensor. Since the electric displacement vector $\mathbf{D}$ is such that $\mathbf{D} = \varepsilon_0[\boldsymbol{\varepsilon}]\mathbf{E} + \mathbf{P}^1$ we get:

$$\mathbf{D} = \varepsilon_0[\boldsymbol{\varepsilon}]\mathbf{E} \tag{3.18}$$

where $[\boldsymbol{\varepsilon}]$ is the relative permittivity tensor and is related to the electric susceptibility tensor $[\boldsymbol{\chi}]$ through the relation: $[\boldsymbol{\varepsilon}] = [\mathbf{I}] + [\boldsymbol{\chi}]$, where $\mathbf{I}$ is the identity matrix.

As the electric permittivity of materials is closely related to the notion of the refractive index ($\varepsilon = n^2$), the properties of the dielectric tensor $[\boldsymbol{\varepsilon}]$ are immediately translated to the optical properties of the materials. With the exception of some peculiar cases, the considered media are non-magnetic, i.e. their magnetic permeability constant μ is equal to μ_0. The relative permittivity tensor $[\boldsymbol{\varepsilon}]$ is symmetrical for non-absorbent materials, i.e.

$$\varepsilon_{ij} = \varepsilon_{ji}. \tag{3.19}$$

It can also be shown that, in the case where the terms of the tensor $[\boldsymbol{\varepsilon}]$ are complex numbers, without the medium being absorbent, the previous relation would become:

$$\varepsilon_{ij} = \varepsilon^*_{ji} \tag{3.20}$$

which more generally shows that the permittivity tensor is Hermitian. Only the media possessing circular anisotropy exhibit this special property.

The case of absorbent media is non-negligible complication because they exhibit not only the linear anisotropy but also an absorption related anisotropy. The latter phenomenon is known as dichroism.

The electric field associated with a monochromatic plane electromagnetic waves with an angular frequency $\omega = 2\pi\nu$ and a wavevector $\mathbf{k}$, propagating through a non-absorbent medium exhibiting a linear anisotropy are characterized by the dielectric tensor $[\varepsilon]$ which can be expressed using the complex notation:

$$\mathbf{E} = \mathbf{E}_0 \exp[-i(\omega t - \mathbf{kr})] \tag{3.21}$$

The other components of the electromagnetic field, $\mathbf{D}$, $\mathbf{B}$, and $\mathbf{H}$, naturally exhibit the same spatio-temporal dependency. Without any source term, the solution of Maxwell's equations in terms of field $\mathbf{D}$ by eliminating the field $\mathbf{H}$ and by introducing a unit vector $\widehat{\mathbf{u}}$ in the direction of propagation of the wave phase, i.e. $\mathbf{k} = k\widehat{\mathbf{u}}$, we obtain:

$$\mathbf{D} = \frac{k^2}{\omega^2 \mu_0}[\mathbf{E} - (\widehat{\mathbf{u}}.\mathbf{E})\widehat{\mathbf{u}}] \tag{3.22}$$

It is useful to note, in more general case, that the vector $\mathbf{D}$ is not parallel to vector $\mathbf{E}$ any more. Therefore, the scalar product $\widehat{\mathbf{u}}.\mathbf{E}$ is not null and the electric field is not transverse as was the case with an isotropic medium. Only the fields $\mathbf{D}$, $\mathbf{H}$ (or $\mathbf{B}$) are transverse, i.e. perpendicular to the wave vector $\mathbf{k}$. The electric field $\mathbf{E}$ usually is not.

The solutions to Maxwell's equations as plane waves of wave vector $\mathbf{k} = k\widehat{\mathbf{u}}$ for which the components of the vector $\widehat{\mathbf{u}}$ are $[\alpha,\, \beta,\, \gamma]$ are given by the Fresnel's equation:

$$\frac{n_x^2 \alpha^2}{n^2 - n_x^2} + \frac{n_y^2 \beta^2}{n^2 - n_y^2} + \frac{n_z^2 \gamma^2}{n^2 - n_z^2} = 0 \tag{3.23}$$

Fresnel's equation leads to concept of birefringence and to following conclusions.
–For a given direction of propagation $\widehat{\mathbf{u}}$, there are two solutions for n^2, lets say $\pm n_1$ and $\pm n_2$. The $\pm$ sign corresponds to the two possible directions of propagation along the unit vector $\widehat{\mathbf{u}}$. The positive values n_1 and n_2 are the solutions of Fresnel's equation and existence of these two values and therefore, their difference ($\Delta n = n_2 - n_1$) gives the birefringence.
–Each of the two values of refractive index is related to a plane wave characterized by its electric displacement vector $\mathbf{D}$ and its phase velocity v. Hence, for a given direction propagation $\widehat{\mathbf{u}}$, there are two plane waves characterized by $\mathbf{D}_1$ and $\mathbf{D}_2$ which are orthogonal to vector $\widehat{\mathbf{u}}$. Moreover, they travel with phase velocities $v_1 = c/n_1$ and $v_2 = c/n_2$, respectively.

3.3.2 Birefringence and Dichroism in Optical FBG

As it has been mentioned in the previous section that any birefringent medium can be characterized by the dielectric tensor $\boldsymbol{\varepsilon}_r$. The electric displacement vector $\mathbf{D}$ is not parallel to the electric field vector $\mathbf{E}$ and this relation, in general, is written as

$$\mathbf{D} = \varepsilon_0 \boldsymbol{\varepsilon}_r \mathbf{E} = \varepsilon_0 \begin{bmatrix} \varepsilon_{r,xx} & \varepsilon_{r,xy} & \varepsilon_{r,xz} \\ \varepsilon_{r,yx} & \varepsilon_{r,yy} & \varepsilon_{r,yz} \\ \varepsilon_{r,zx} & \varepsilon_{r,zy} & \varepsilon_{r,zz} \end{bmatrix} \mathbf{E}. \tag{3.24}$$

The vector electromagnetic wave equation now has the dielectric tensor $\boldsymbol{\varepsilon}_r$ instead of relative permittivity ε_r and is written as

$$\nabla \mathbf{E} = \mu_0 \varepsilon_0 \boldsymbol{\varepsilon}_r \left(\frac{\partial}{\partial t}\right)^2 \mathbf{E}. \tag{3.25}$$

Since the quantities $\boldsymbol{\varepsilon}_{\mathrm{t}} = \boldsymbol{\varepsilon}_r(x,\, y)$ and hence the transverse field components $\mathbf{E}_{\mathrm{t}} = (\mathbf{E}_x,\, \mathbf{E}_y)$ are independent of z, one can write

$$\left(\frac{\partial}{\partial z}\right)^2 \mathbf{E} = \mu_0 \varepsilon_0 \boldsymbol{\varepsilon}_r \left(\frac{\partial}{\partial t}\right)^2 \mathbf{E}. \tag{3.26}$$

For source free medium $\nabla \cdot \mathbf{D} = 0$ and moreover, there is no $\mathbf{D}_z$ component. It can be shown that it is indeed zero as follows:

$$\mathbf{D}_z = \varepsilon_0 \begin{bmatrix} \varepsilon_{r,zx} & \varepsilon_{r,zy} & \varepsilon_{r,zz} \end{bmatrix} \begin{bmatrix} E_x \\ E_y \\ E_z \end{bmatrix} = 0 \Leftrightarrow E_z = -\frac{\varepsilon_{r,zx} E_x + \varepsilon_{r,zy} E_y}{\varepsilon_{r,zz}}. \tag{3.27}$$

Therefore, the three dimensional vector wave equation reduces to two dimensional one with only transverse components $\mathbf{E}_t$:

$$\left(\frac{\partial}{\partial z}\right)^2 \begin{bmatrix} E_x \\ E_y \end{bmatrix} = \mu_0 \varepsilon_0 \begin{bmatrix} \varepsilon_{r,xx} & \varepsilon_{r,xy} & \varepsilon_{r,xz} \\ \varepsilon_{r,yx} & \varepsilon_{r,yy} & \varepsilon_{r,yz} \end{bmatrix} \left(\frac{\partial}{\partial t}\right)^2 \begin{bmatrix} E_x \\ E_y \\ E_z \end{bmatrix} \tag{3.28-a}$$

with

$$\begin{bmatrix} E_x \\ E_y \\ E_z \end{bmatrix} = \begin{pmatrix} 1 & 0 \\ 0 & 1 \\ -\frac{\varepsilon_{r,zx}}{\varepsilon_{r,zz}} & -\frac{\varepsilon_{r,zy}}{\varepsilon_{r,zz}} \end{pmatrix} \begin{bmatrix} E_x \\ E_y \end{bmatrix} \tag{3.28-b}$$

Inserting 3.28-b into 3.28-a, we get

$$\left(\frac{\partial}{\partial z}\right)^2 \begin{bmatrix} E_x \\ E_y \end{bmatrix} = \mu_0 \varepsilon_0 \begin{bmatrix} \varepsilon_{r,xx} & \varepsilon_{r,xy} & \varepsilon_{r,xz} \\ \varepsilon_{r,yx} & \varepsilon_{r,yy} & \varepsilon_{r,yz} \end{bmatrix} \begin{pmatrix} 1 & 0 \\ 0 & 1 \\ -\frac{\varepsilon_{r,zx}}{\varepsilon_{r,zz}} & -\frac{\varepsilon_{r,zy}}{\varepsilon_{r,zz}} \end{pmatrix} \left(\frac{\partial}{\partial t}\right)^2 \begin{bmatrix} E_x \\ E_y \end{bmatrix}. \tag{3.29}$$

The matrix multiplication in (3.29) gives

$$\begin{aligned} \left(\frac{\partial}{\partial z}\right)^2 \begin{bmatrix} E_x \\ E_y \end{bmatrix} &= \mu_0 \varepsilon_0 \begin{bmatrix} \varepsilon_{r,xx} - \frac{\varepsilon_{r,zx}}{\varepsilon_{r,zz}} \varepsilon_{r,xz} & \varepsilon_{r,xy} - \frac{\varepsilon_{r,zy}}{\varepsilon_{r,zz}} \varepsilon_{r,xy} \\ \varepsilon_{r,yx} - \frac{\varepsilon_{r,zx}}{\varepsilon_{r,zz}} \varepsilon_{r,yz} & \varepsilon_{r,yy} - \frac{\varepsilon_{r,zy}}{\varepsilon_{r,zz}} \varepsilon_{r,yy} \end{bmatrix} \left(\frac{\partial}{\partial t}\right)^2 \begin{bmatrix} E_x \\ E_y \end{bmatrix} \\ &= \mu_0 \varepsilon_0 \begin{bmatrix} \varepsilon_{xx} & \varepsilon_{xy} \\ \varepsilon_{yx} & \varepsilon_{yy} \end{bmatrix} \left(\frac{\partial}{\partial t}\right)^2 \begin{bmatrix} E_x \\ E_y \end{bmatrix} \end{aligned}. \tag{3.30}$$

The refractive index matrix $\mathbf{n}$ is directly related to the dielectric tensor $\boldsymbol{\varepsilon}$ ($\mathbf{n} = \sqrt{\boldsymbol{\varepsilon}}$). This refractive index matrix $\mathbf{n}$ will have to eigen values, say $\pm n_1$ and $\pm n_2$. If one considers only positive eigen values, say n_1 and n_2 along the positive x- and y- direction, respectively, then their difference with respect to the average refractive index $\overline{n}$ gives the birefringence

$$\Delta n = \frac{n_2 - n_1}{\overline{n}} \quad \text{and} \quad \overline{n} = \frac{n_1 + n_2}{2}. \tag{3.31}$$

Due to birefringence, Bragg grating with the given refractive index modulation (Δn_{pp}) and the grating period Λ will always reflect two discrete wavelengths say, $\lambda_{\mathrm{B}\,1}$ and $\lambda_{\mathrm{B}\,2}$, corresponding to these two eigenvalues, and are equal to

$$\lambda_{\mathrm{B}\,1,\,2} = 2n_{1,\,2}\Lambda. \tag{3.32}$$

Therefore, there will be two reflectivities ρ_1 and ρ_2 and two eigenvectors, say $\mathbf{E}_1$ and $\mathbf{E}_2$, corresponding to these two eigenvalues of the refractive index matrix $\mathbf{n}$. The resultant electric field of the output wave reflected by the grating depends on the polarization or the electric field of the input wave that is parallel to one of the eigenvectors. This resultant electric field could then be written as

$$\mathbf{E}_{\mathrm{out}} = \rho_1 E_{\mathrm{in},\,1}\mathbf{E}_1 + \rho_2 E_{\mathrm{in},\,2}\mathbf{E}_2. \tag{3.33}$$

The reflection coefficient is no more a scalar quantity. It represents a 2x2 Jones reflectance matrix:

$$\mathbf{E}_{\mathrm{out}} = \boldsymbol{\rho}\mathbf{E}_{\mathrm{in}} = \begin{bmatrix} \rho_{11} & \rho_{12} \\ \rho_{21} & \rho_{22} \end{bmatrix} \mathbf{E}_{\mathrm{in}}. \tag{3.34}$$

3.3.3 Polarization Mode Coupling

For the medium with no birefringence, the dielectric tensor obeys the relation $\boldsymbol{\varepsilon} = \boldsymbol{\varepsilon}^{\dagger}$. With eigenvalue decomposition the dielectric tensor $\boldsymbol{\varepsilon}$ is decomposed into

$$\boldsymbol{\varepsilon} = \mathbf{E}_{\boldsymbol{\varepsilon}} \begin{pmatrix} \varepsilon_1 & 0 \\ 0 & \varepsilon_2 \end{pmatrix} \mathbf{E}_{\boldsymbol{\varepsilon}}^{+} \tag{3.35}$$

with $\varepsilon_{1,\,2} \in \mathbf{R}$ and orthogonal eigenvectors $\mathbf{E}_{\boldsymbol{\varepsilon}} = [\mathbf{E}_1,\, \mathbf{E}_2]$ with scalar product equal to the Kronecker delta ($\mathbf{E}_i \cdot \mathbf{E}_j^{*} = \delta_{ij}$).

The dielectric tensor for anisotropic optical grating with a periodic modulation of refractive index is written as

$$\boldsymbol{\varepsilon}(z) = \varepsilon_0\boldsymbol{\varepsilon}_b + \boldsymbol{\varepsilon}_g e^{\jmath k_g z} + \boldsymbol{\varepsilon}_g^{+} e^{-\jmath k_g z}. \tag{3.36}$$

The first term $\boldsymbol{\varepsilon}_b$ comes from the static birefringence while the second and third term comes from the grating structure that couples the forward and the backward propagating modes. Since Δn is directly proportional to $\Delta\varepsilon$; the above equation directly transforms into

$$\Delta\mathbf{n}(z) = \Delta\mathbf{n}_b + \Delta\mathbf{n}_k e^{\jmath k_g z} + \Delta\mathbf{n}_k^{+} e^{-\jmath k_g z}, \tag{3.37}$$

where the birefringence and refractive index modulation matrices are

$$\begin{aligned} \Delta\mathbf{n}_b &= \begin{pmatrix} \Delta n_{11} & \Delta n_{12} \\ \Delta n_{12}^{*} & -\Delta n_{11} \end{pmatrix} \\ \Delta\mathbf{n}_\kappa &= \frac{1}{4} e^{\jmath\phi_k} \begin{pmatrix} \Delta n_{pp11} & \Delta n_{pp12} \\ \Delta n_{pp21} & \Delta n_{pp22} \end{pmatrix} \end{aligned}. \tag{3.38}$$

The electric field of the forward and backward propagating waves is given by

$$\begin{aligned}\mathbf{E}_f(z,\,t) &= \mathbf{D}(z)e^{\jmath\omega t-kz}\\ \mathbf{E}_b(z,\,t) &= \mathbf{U}(z)e^{\jmath\omega t+kz}\end{aligned}\quad \text{with}\quad k=\frac{\omega}{c_0}\mathbf{n}(z), \tag{3.39}$$

while there superposition gives the total field as

$$\mathbf{E}(z,\,t)=\mathbf{D}(z)e^{\jmath\omega t-kz}+\mathbf{U}(z)e^{\jmath\omega t+kz}. \tag{3.40}$$

The electromagnetic wave equation with this electric field and refractive index modulation is written as

$$\left(\frac{\partial}{\partial z}\right)^2\mathbf{E}(z,\,t)=\left(\frac{\mathbf{n}(z)}{c_0}\right)^2\left(\frac{\partial}{\partial t}\right)^2\mathbf{E}(z,\,t). \tag{3.41}$$

Simplification of this equation similar to the one derived in Appendix C yields

$$\begin{aligned}\frac{\partial}{\partial z}\mathbf{D}(z) &= -\jmath\boldsymbol{\beta}(z)\mathbf{D}(z)+\boldsymbol{\kappa}^*(z)e^{\jmath(2k-k_g)z}\mathbf{U}(z)\\ \frac{\partial}{\partial z}\mathbf{U}(z) &= \jmath\boldsymbol{\beta}(z)\mathbf{U}(z)+\boldsymbol{\kappa}(z)e^{-\jmath(2k-k_g)z}\mathbf{D}(z)\end{aligned}, \tag{3.42}$$

with

$$\begin{aligned}\boldsymbol{\beta}(z) &= \frac{k}{n_0}\Delta\mathbf{n}_b(z)\\ \boldsymbol{\kappa}(z) &= \frac{\jmath k}{n_0}\Delta\mathbf{n}_k(z)\end{aligned}. \tag{3.43}$$

3.3.4 Measurement of Complex Reflectance Jones Matrix

Any birefringent or dichroic optical device like FBG has the frequency-dependent reflection coefficient $\rho(f)$ which depends on the input polarization and the reference polarization which is analyzed at its output. An interferometric measurement determines a complex reflection coefficient

$$\rho(f)=\rho_{\mathbf{E}_\mathrm{r},\,\mathbf{E}_\mathrm{m}}(f) \tag{3.44}$$

where $\mathbf{E}_\mathrm{r}$ is the Jones vectors in the reference branch while $\mathbf{E}_\mathrm{m}$ is the Jones vector in the measurement branch where the device under test is inserted. The interference contrast is at its maximum when the polarizations in the reference and measurement branch of the interferometer are identical.

In order to determine the complete 2x2 Jones reflectance matrix $\boldsymbol{\rho}$, the four combinations of $\rho_{\mathrm{r},\,\mathrm{m}}$ have to be measured and these will be the elements of $\boldsymbol{\rho}$. The above scalar equation for the complex reflection coefficient is modified to

$$\boldsymbol{\rho}(f)=\mathbf{E}_\mathrm{r}^+\boldsymbol{\rho}_{\mathrm{r,m}}(f)\mathbf{E}_\mathrm{m} \tag{3.45}$$

where $\mathbf{E}_{\mathrm{r}}$ and $\mathbf{E}_{\mathrm{m}}$ are the two pairs of Jones vectors. Even if Jones vector $\mathbf{E}_{\mathrm{r}}$ and $\mathbf{E}_{\mathrm{m}}$ are unknown the knowledge of elements of the transformed $\boldsymbol{\rho}$ matrix is generally sufficient to reveal the birefringence and dichroism because the transformed $\boldsymbol{\rho}$ matrix is no more than the original $\boldsymbol{\rho}$ matrix which is pre- and post- multiplied by the unitary matrices $[\mathbf{E}_{\mathrm{r}_{||}}, \mathbf{E}_{\mathrm{r}_{\perp}}]^{+}$ and $[\mathbf{E}_{\mathrm{m}_{||}}, \mathbf{E}_{\mathrm{m}_{\perp}}]$, respectively. It is indeed difficult to generate such orthogonal pairs of polarization by using the calibrated polarization transformers based on $LiNbO_3$ due to DC drift. The polarization orthogonalization scheme derived by Sandel [16] which makes use of Poincaré's sphere based tetrahedrons is used here to measure the complete reflectance Jones matrix of the device under test which is complex.

To use orthogonalization scheme, it is necessary to generate two sets of four arbitrary polarizations which form a tetrahedron with nonzero volume on the Poincaré sphere: one for reference- and another for measurement- branch. These polarizations are generated using the calibrated polarization transformers that are based on X-cut, Z-propagation $LiNbO_3$ (see Figure 2.1).

The transformed elements of $\boldsymbol{\rho}_{\mathrm{r,\,m}}$ corresponding to orthogonal pairs of $\mathbf{E}_{\mathrm{r}}$ and $\mathbf{E}_{\mathrm{m}}$ can be deduced from 16 reflectances

$$\boldsymbol{\rho}_{\mathrm{r}_i,\,\mathrm{m}_j}(f) = \rho_{\mathbf{E}_{\mathrm{r}_i},\,\mathbf{E}_{\mathrm{m}_j}} = \mathbf{E}^{+}_{\mathrm{r}_i}\boldsymbol{\rho}_{i,\,j}(f)\mathbf{E}_{\mathrm{m}_j} \quad i,\,j \in \{0\cdots 3\} \tag{3.46}$$

measured with four arbitrary $\mathbf{E}_{\mathrm{r}_i}$ and four arbitrary $\mathbf{E}_{\mathrm{m}_j}$. These two sets of four arbitrary polarizations enable us to derive two sets of orthogonal polarization pairs:

$$\begin{array}{ll} \mathbf{E}_{\mathrm{r}_{||}},\,\mathbf{E}_{\mathrm{r}_{\perp}} & \text{with} \quad \mathbf{E}_{\mathrm{r}_{||}}\cdot\mathbf{E}_{\mathrm{r}_{\perp}} = 0 \\ \mathbf{E}_{\mathrm{m}_{||}},\,\mathbf{E}_{\mathrm{m}_{\perp}} & \text{with} \quad \mathbf{E}_{\mathrm{m}_{||}}\cdot\mathbf{E}_{\mathrm{m}_{\perp}} = 0 \end{array}. \tag{3.47}$$

With this orthogonal pairs of polarization, the measured 2x2 Jones reflectance matrix now becomes

$$\begin{bmatrix} \rho_{\mathbf{E}_{\mathrm{r}_{||}},\,\mathbf{E}_{\mathrm{m}_{||}}}(f) & \rho_{\mathbf{E}_{\mathrm{r}_{||}},\,\mathbf{E}_{\mathrm{m}_{\perp}}}(f) \\ \rho_{\mathbf{E}_{\mathrm{r}_{\perp}},\,\mathbf{E}_{\mathrm{m}_{||}}}(f) & \rho_{\mathbf{E}_{\mathrm{r}_{\perp}},\,\mathbf{E}_{\mathrm{m}_{\perp}}}(f) \end{bmatrix} = \begin{bmatrix} \mathbf{E}_{\mathrm{r}_{||}} \\ \mathbf{E}_{\mathrm{r}_{\perp}} \end{bmatrix} \cdot \boldsymbol{\rho} \cdot \begin{bmatrix} \mathbf{E}_{\mathrm{m}_{||}} & \mathbf{E}_{\mathrm{m}_{\perp}} \end{bmatrix} = \mathbf{R}_L \cdot \boldsymbol{\rho} \cdot \mathbf{R}_R = \widetilde{\boldsymbol{\rho}}, \tag{3.48}$$

where the subscripts $||$ and $\perp$ refers to orthogonal pairs of polarizations, both at the input of the device under test which is inserted in the measurement branch and in the reference branch. Polarization transformers which generates these waves must operate reproducibly but calibration is not needed. The rotation matrices $\mathbf{R}_L$ and $\mathbf{R}_R$ are in fact unitary. This frequency-dependent transformed $\boldsymbol{\rho}$ matrix enables us to calculate the impulse response and hence vectorial grating structure.

3.3.5 Polarization Orthogonalization

For some special cases which are excluded here, every polarization $\mathbf{E}_{\mathrm{r}_i}$ and $\mathbf{E}_{\mathrm{m}_j}$ in section 3.3.4 can be expressed by a linear combination of two others (see Figure 3.9), for example,

$$\mathbf{E}_{\mathrm{m}_0} = \vartheta_1\mathbf{E}_{\mathrm{m}_1} + \vartheta_2\mathbf{E}_{\mathrm{m}_2} = \xi_1\mathbf{E}_{\mathrm{m}_1} + \xi_3\mathbf{E}_{\mathrm{m}_3}, \tag{3.49}$$

where ϑ_1, ϑ_2, ξ_1, ξ_3 are scalers. For fixed i, the reflectances $\rho_{i,j}$ can also be expressed using the same scalers, for example,

$$\rho_{i,0} = \vartheta_1 \rho_{i,1} + \vartheta_2 \rho_{i,2} = \xi_1 \rho_{i,1} + \xi_3 \rho_{i,3}. \tag{3.50}$$

This is obvious because the same polarizations are used during the measurement of $\boldsymbol{\rho}_{i,j}$.

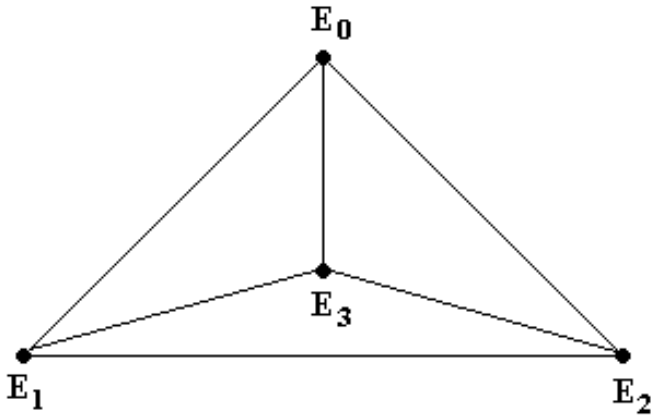

Figure 3.9: Schematic of a Poincaré sphere-based tetrahedron

One possibility to determined the coefficients ϑ_1, ϑ_2, ξ_1, and ξ_3 from the measured frequency-dependent reflection coefficients $\boldsymbol{\rho}_{i,j}(f)$ is to effectively use (3.50). In fact, this can be easily done by integrating the matrix product of $\boldsymbol{\rho}^{+}_{i,j}(f)$ and $\boldsymbol{\rho}_{i,j}(f)$ where '+' sign indicates the Hermitian conjugate over the whole frequency range, i.e. ν going from 0 to N.

$$\mathbf{H} = \begin{bmatrix} h_{00} & h_{01} & h_{02} & h_{03} \\ h_{10} & h_{11} & h_{12} & h_{13} \\ h_{20} & h_{21} & h_{22} & h_{23} \\ h_{30} & h_{31} & h_{32} & h_{33} \end{bmatrix} = \int_{\nu=0}^{N} \boldsymbol{\rho}^{+}_{i,j}(f_\nu) \cdot \boldsymbol{\rho}_{i,j}(f_\nu) df \tag{3.51}$$

where each element of $\mathbf{H}$ is given by

$$h_{i,j} = \sum_{k=0}^{3} \sum_{\nu=0}^{N} \rho^{*}_{i,k}(f_\nu) \rho_{j,k}(f_\nu) df. \tag{3.52}$$

For any Hermitian matrix, say $\mathbf{H}$, the eigenvalues of $\mathbf{H}$ are real, $\mathbf{H}$ is diagonalizable, eigenvectors corresponding to distinct and nonzero eigenvalues are orthogonal, and the matrix $\mathbf{H}$ possesses a complete orthonormal set of eigenvectors. Eigenvalue decomposition of this $\mathbf{H}$ matrix yields four eigenvalues $\boldsymbol{\lambda}_j$ (where $j = 0 \cdots 3$) and the corresponding four eigenvectors $\boldsymbol{\chi}_j$ (where $j = 0 \cdots 3$). The two out of four eigenvalues should come out to be identically zero because two out of four polarizations which are used during the

measurement of $\boldsymbol{\rho}_{i,j}$ are linearly dependent on two other polarizations and hence two out of four columns and rows of $\boldsymbol{\rho}_{i,j}$ are also linearly dependent on two other columns and rows of $\boldsymbol{\rho}_{i,j}$. In practice, the two out of four eigenvalues are not identically zero but are rather close to zero due to measurement errors and polarization drift. It is indeed possible to select two eigenvectors corresponding to two eigenvalues which are close to zero, say for example, λ_1 and λ_2, because these two eigenvectors are linearly dependent on each other. One linear combination of these two eigenvectors yields ϑ_1 and ϑ_2 when first and last element is set to -1 and 0, respectively, while their second linear combination yields ξ_1 and ξ_3 when first and third element is set to -1 and 0, respectively. Therefore, one can write

$$\begin{bmatrix} -1 \\ \vartheta_1 \\ \vartheta_2 \\ 0 \end{bmatrix} = \alpha_1 \boldsymbol{\chi}_{\lambda_1} + \alpha_2 \boldsymbol{\chi}_{\lambda_2} \quad \text{and} \quad \begin{bmatrix} -1 \\ \xi_1 \\ 0 \\ \xi_3 \end{bmatrix} = \beta_1 \boldsymbol{\chi}_{\lambda_1} + \beta_3 \boldsymbol{\chi}_{\lambda_3}, \tag{3.53}$$

where α_1, α_2, β_1, and β_3 are two set of constants. Every $\mathbf{E}_{\mathrm{m}_j}$ can be further expressed by the desired orthogonal pair $\mathbf{E}_{\mathrm{m}_{||}}$ and $\mathbf{E}_{\mathrm{m}_\perp}$ as

$$\mathbf{E}_{\mathrm{m}_j} = C_j \mathbf{E}_{\mathrm{m}_{||}} + D_j \mathbf{E}_{\mathrm{m}_\perp} \quad (|C_j|^2 + |D_j|^2 = 1,\ j = 1 \cdots 3). \tag{3.54}$$

For $j = 0$, let $\mathbf{E}_{\mathrm{m}_0} = \mathbf{E}_{\mathrm{m}_{||}}$ by definition. There are nine degrees of freedom in the choice of C_j and D_j. The eight real equations in (3.49) balance them except for the phase of one of the component of $\mathbf{E}_{\mathrm{m}_\perp}$, which can be freely chosen. For example, D_1 can be set to a real positive number. For $\mathbf{E}_{\mathrm{m}_{||}}$ and $\mathbf{E}_{\mathrm{m}_\perp}$ polarization components, the insertion of (3.54) into (3.49) results in

$$1 = \vartheta_1 C_1 + \vartheta_2 C_2 \quad 1 = \xi_1 C_1 + \xi_3 C_3 \tag{3.55}$$

and

$$0 = \vartheta_1 D_1 + \vartheta_2 D_2 \quad 0 = \xi_1 D_1 + \xi_3 D_3 \tag{3.56}$$

respectively. This allows C_2, C_3, D_2, and D_3 to be expressed in terms of C_1 and D_1 as

$$C_2 = \frac{1 - \vartheta_1}{\vartheta_2} C_1 \quad C_3 = \frac{1 - \xi_1}{\xi_3} C_1, \tag{3.57}$$

$$D_2 = -\frac{\vartheta_1}{\vartheta_2} D_1 \quad D_3 = -\frac{\xi_1}{\xi_3} D_1. \tag{3.58}$$

The expressions $(|C_j|^2 + |D_j|^2 = 1,\ j = 1 \cdots 3)$ with (3.57) and (3.58) inserted for $j = 2$ and 3 lead to a set of two equations linear in $\mathrm{Re}(C_1)$ and $\mathrm{Im}(C_1)$ whose solution is

$$\begin{bmatrix} \mathrm{Re}(C_1) \\ \mathrm{Im}(C_1) \end{bmatrix} = \frac{1}{2} \begin{bmatrix} \mathrm{Re}(\vartheta_1) & -\mathrm{Im}(\vartheta_1) \\ \mathrm{Re}(\xi_1) & -\mathrm{Im}(\xi_1) \end{bmatrix}^{-1} \begin{bmatrix} 1 - |\vartheta_2|^2 + |\vartheta_1|^2 \\ 1 - |\xi_3|^2 + |\xi_1|^2 \end{bmatrix}. \tag{3.59}$$

The positive real scalar D_1 can be derived from the complex C_1 as

$$D_1 = \sqrt{1 - |C_1|^2}. \tag{3.60}$$

In principle, the scalers C_1 and D_1 are sufficient to calculate $\mathbf{E}_{\mathrm{m}_\perp}$ from $\mathbf{E}_{\mathrm{m}_0}$ and $\mathbf{E}_{m_1}$ and corresponding reflection factors:

$$\mathbf{E}_{\mathrm{m}_\perp} = \frac{\mathbf{E}_{\mathrm{m}_j} - C_1\mathbf{E}_{\mathrm{m}_0}}{D_1}\,, \rho_{\mathrm{r}_i,\,\mathrm{m}_\perp} = \frac{\rho_{\mathrm{r}_i,\,\mathrm{m}_j} - C_1\rho_{\mathrm{r}_i,\,\mathrm{m}_0}}{D_1}\;(i = 0\cdots 3,\; j = 1). \tag{3.61}$$

In practice, there are always some random errors in every measured $\rho_{\mathrm{r}_i,\mathrm{m}_j}$. This lead errors in $\rho_{\mathrm{r}_i,\mathrm{m}_\perp}$ which are enhanced by the factor $1/D_1$. Since C_2, C_3, D_2, and D_3 can be easily derived from C_1 and D_1 using (3.57) and (3.58). The index $j = 1$ in (3.61), may be replaced by k going from 2 to 3 or an average over all $j = 1\cdots 3$ is taken which is in fact a better choice. The weighted averages of $|D_j|^2$ results in

$$\begin{aligned}\mathbf{E}_{\mathrm{m}_\perp} &= \frac{\sum_{j=1}^{3}|D_j|^2\frac{\mathbf{E}_{\mathrm{m}_j}-C_1\mathbf{E}_{\mathrm{m}_0}}{D_1}}{\sum_{j=1}^{3}|D_j|^2}\\ \rho_{\mathrm{r}_i,\,\mathrm{m}_\perp} &= \frac{\sum_{j=1}^{3}|D_j|^2\frac{\rho_{\mathrm{r}_i,\,\mathrm{m}_j}-C_1\rho_{\mathrm{r}_i,\,\mathrm{m}_0}}{D_1}}{\sum_{j=1}^{3}|D_j|^2}\end{aligned} \tag{3.62}$$

with minimum errors for a given set of $\mathbf{E}_{\mathrm{m}_j}$ for $j = 0\cdots 3$. An analogous process would orthogonalize the reference polarization and a (transformed) 2x2 Jones reflectance matrix would result (3.34). This polarization orthogonalization scheme was proposed and successfully used by D. Sandel [16].

3.3.6 Calculation of Impulse Response Matrix

For vectorial grating structure characterization, the matrix impulse response

$$\mathbf{h}(t) = \begin{bmatrix} h_{11}(t) & h_{12}(t) \\ h_{21}(t) & h_{22}(t) \end{bmatrix} \Leftrightarrow \boldsymbol{\rho}(f) = \begin{bmatrix} \rho_{11}(f) & \rho_{12}(f) \\ \rho_{21}(f) & \rho_{22}(f) \end{bmatrix} \tag{3.63}$$

is calculated by inverse Fourier transform of each of the reflectances

$$h_{i,\,j}(t) = F^{-1}(\rho_{i,\,j}(f)). \tag{3.64}$$

3.3.7 Calculation of Vectorial Grating Structure

The difference equations which are discretized using the position step Δz and corresponding time step $\Delta t = (n_0/c)\Delta z$ are derived in

$$\begin{aligned}\mathbf{D}_{\mu,\,\nu} &= \boldsymbol{\tau}_{\mu-1}^{-1}(-\mathbf{b}_{\mu-1}^{-1}\mathbf{k}_{\mu-1}^{+}\mathbf{U}_{\mu-1,\,\nu+1} + \mathbf{b}_{\mu-1}\mathbf{D}_{\mu-1,\,\nu-1})\\ \mathbf{U}_{\mu,\,\nu} &= \boldsymbol{\tau}_{\mu-1}^{-1}(\mathbf{b}_{\mu-1}^{-1}\mathbf{U}_{\mu-1,\,\nu+1} + \mathbf{b}_{\mu-1}\mathbf{k}_{\mu-1}\mathbf{D}_{\mu-1,\,\nu-1})\end{aligned} \tag{3.65}$$

where $\mathbf{D}$ is the electric field matrix of the forward- and $\mathbf{U}$ the electric field matrix of the backward-propagating waves from piecewise solutions of

$$\begin{aligned}(\frac{\partial}{\partial z} + \frac{n_\mathrm{o}}{c}\frac{\partial}{\partial t})\mathbf{D}(z,t) &= -\jmath\boldsymbol{\beta}(z)\mathbf{D}(z,t) + \boldsymbol{\kappa}^*(z)\mathbf{U}(z,t)\\ (\frac{\partial}{\partial z} - \frac{n_\mathrm{o}}{c}\frac{\partial}{\partial t})\mathbf{U}(z,t) &= \jmath\boldsymbol{\beta}(z)\mathbf{U}(z,t) + \boldsymbol{\kappa}(z)\mathbf{D}(z,t)\end{aligned} \tag{3.66}$$

under the assumptions of locally constant $\boldsymbol{\kappa}$ and $\boldsymbol{\beta}$ matrices which are given here in the diagonalized form

$$\begin{aligned} \mathbf{k} = \boldsymbol{\kappa}\Delta z = \mathbf{E}_k \begin{pmatrix} k_1 & 0 \\ 0 & k_2 \end{pmatrix} \mathbf{E}_k^+ \\ \mathbf{b} = exp(-\jmath\boldsymbol{\beta}\Delta z) = \mathbf{E}_b \begin{pmatrix} b & 0 \\ 0 & b^* \end{pmatrix} \mathbf{E}_b^+ \end{aligned}, \tag{3.67}$$

represents the grating coupling coefficient and birefringence, respectively, for one position step Δz. Transmission matrix must satisfy the lossless relation

$$\boldsymbol{\tau}\boldsymbol{\tau}^+ + \mathbf{k}\mathbf{k}^+ = \mathbf{I}. \tag{3.68}$$

This matrix is Hermitian and has same eigenvectors as that of $\mathbf{k}$. In the calculation of

$$\boldsymbol{\tau} = \sqrt{\mathbf{I} - \mathbf{k}\mathbf{k}^+} = \mathbf{E}_k \begin{pmatrix} t_1 & 0 \\ 0 & t_2 \end{pmatrix} \mathbf{E}_k^+ \quad (t_1,\, t_2 > 0) \tag{3.69}$$

positive signs must be chosen for its real eigenvalues t_1, t_2.

Figure 3.3 shows the wave propagation and solution sequence in a grid of time, t , and one-dimensional space coordinate z. Solution starts from the knowledge of incident the unity matrix $\mathbf{D}_{0,0}$ (the only nonzero component of a discretized $\mathbf{D} = \mathbf{I}\delta t$) and the measured impulse response matrix $\mathbf{U}_{0,\nu}$ (discretized $\mathbf{U}_{0,t}$=$\mathbf{h}(t)$). Waves $\mathbf{D}_{\mu,\nu}$ and $\mathbf{U}_{\mu,\nu}$, and as far as yet unknowns, $\mathbf{k}$ and $\mathbf{b}$ are calculated in a sequence given by dashed arrow. For calculation of $\mathbf{k}_m$ and $\mathbf{b}_m$, all $\mathbf{k}_\mu$ and $\mathbf{b}_\mu$ with $0 < \mu < m$ must be known. This is automatically the case if one starts with $m = 1$. Each solution step requires the difference equations to be successively solved for $\mu = 1 \cdots m$ and $\nu = 2m - \mu$. $\mathbf{D}_{m,m}$ and $\mathbf{U}_{m,m}$ are obtained as an intermediate result and the matrix quotient

$$\mathbf{Q} = -\mathbf{U}_{m,m}\mathbf{D}_{m,m}^{-1} = \mathbf{b}_m\mathbf{k}_m\mathbf{b}_m \tag{3.70}$$

has to be decomposed in such way that the first product

$$\mathbf{Q}^+\mathbf{Q} = (\mathbf{b}\mathbf{k}\mathbf{b})^+\mathbf{b}\mathbf{k}\mathbf{b} = \mathbf{b}^+\mathbf{E}_k\boldsymbol{\Lambda}_k^+\boldsymbol{\Lambda}_k\mathbf{E}_k^+\mathbf{b} \tag{3.71}$$

delivers $|k_1|$, $|k_2|$ as the square root of its eigenvalues. The missing argument is

$$\arg(k_1) = \arg(k_2) = \frac{1}{2}\arg(\det(\mathbf{k})) \,\text{or}\, \frac{1}{2}\arg(\det(\mathbf{k})) + \pi. \tag{3.72}$$

Second eigenvector matrix $(\mathbf{b}^+\mathbf{E}_k)$ of (3.71) allows for the calculation of matrix

$$(\mathbf{b}\mathbf{E}_k) = \mathbf{Q}(\mathbf{b}^+\mathbf{E}_k)\boldsymbol{\Lambda}_k^{-1}. \tag{3.73}$$

Third, now, we can obtain

$$\mathbf{b} = \sqrt{(\mathbf{b}\mathbf{E}_k)(\mathbf{E}_k^+\mathbf{b})} \tag{3.74}$$

which successively leads to

$$\begin{aligned} \mathbf{E}_k &= \mathbf{b}^{+}(\mathbf{b}\mathbf{E}_k) \\ \mathbf{k} &= \mathbf{E}_k \boldsymbol{\Lambda}_k \mathbf{E}_k^{+}. \end{aligned} \tag{3.75}$$

Expecting a small retardation due to $\mathbf{b}$ within Δz, the ambiguities of (3.75) and (**??**) can be settled so that the argument of eigenvalues of $\mathbf{b}$ are closest to zero. Finally, locally varying $\boldsymbol{\kappa} = \mathbf{k}/\Delta z$ and $\boldsymbol{\beta} = \jmath \ln(\mathbf{b})/\Delta z$ are calculated to yield the gratings peak-to-peak refractive index modulation amplitudes , grating phase, and refractive index differences (birefringence).

3.3.8 Vectorial Measurements

Fiber Bragg grating of reflectivity $> 95\%$ and $\Delta\lambda \approx 0.2$ nm at $\lambda_{\mathrm{B}} = 1548.25$ nm is used as an object for the vectorial structure characterization in both forward as well as backward direction. During the measurements, the temperature of the fiber Bragg grating's is kept constant by mounting it on to a aluminium plate whose temperature is sensed using a thermistor and kept constant using a Peltier element and a simple proportional integral temperature controller. Initially, for vectorial measurement, manual polarization controllers (in Figure 2.1) are adjusted for the maximum interference contrast assuming that only copolarized waves interfere in the output 3x3 fiber coupler of the measurement interferometer. For vectorial structure characterization, the broadband polarization transformers which are on the lithium niobate-based integrated optical network analyzer circuit are initially used to generate the two sets of four arbitrary polarizations for the implementation of orthogonalization scheme. Number of trials has been made to implement this scheme with available DFB laser. Main problem in implementing this scheme is that DFB laser was never stable during the scan and from scan to scan. Therefore, these polarization transformers are calibrated using the commercial rotating quarter waveplate polarimeter to generate the pair of orthogonal polarizations for vectorial measurement. This scheme has worked positively. The results of vectorial structure characterization are summarized below. Scattering parameters, impulse response matrix elements and derived grating structures were essentially identical when like measurements were performed from both sides of the same grating.

Forward Measurement

Figure 3.10(a) shows the magnitude of the elements of the measured frequency-dependent complex reflectance matrix $|\boldsymbol{\rho}(f)|$ while Figure 3.10(b) shows the magnitude of the scalar transmission coefficient $|\tau(f)|$ of this FBG in forward direction.

Figure 3.11(a) shows the impulse response matrix elements $\mathbf{h}(t)$ while Figure 3.11(b) shows the longitudinal grating structure $\boldsymbol{\Delta}n(z)$ with the corresponding grating burst for this FBG in forward direction.

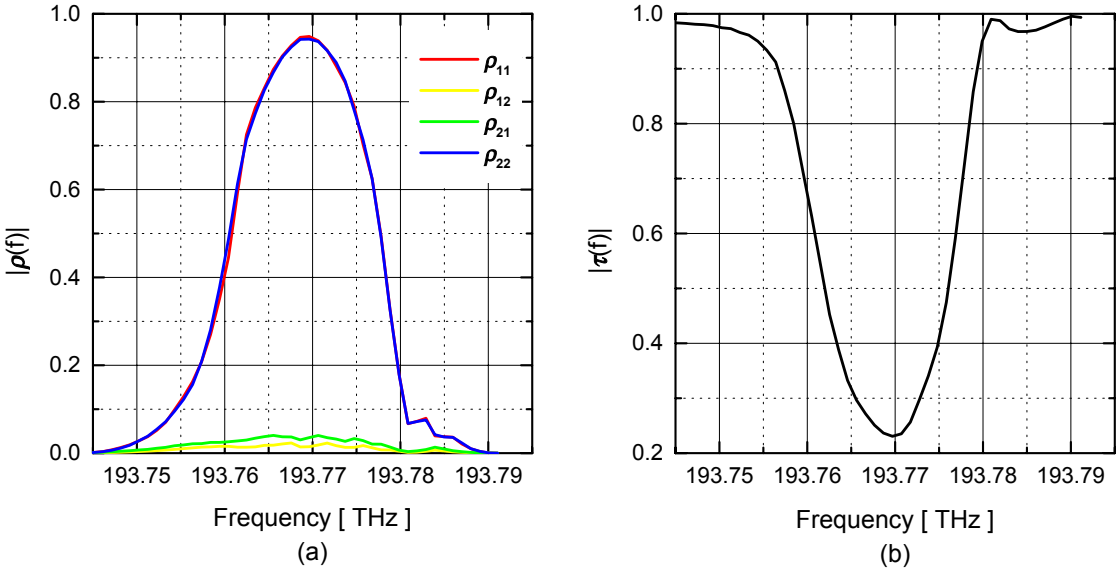

Figure 3.10: (a) 2x2 Jones reflectance matrix elements $|\boldsymbol{\rho}(f)|$ and (b) scalar transmission coefficient $|\tau(f)|$ of FBG in forward direction

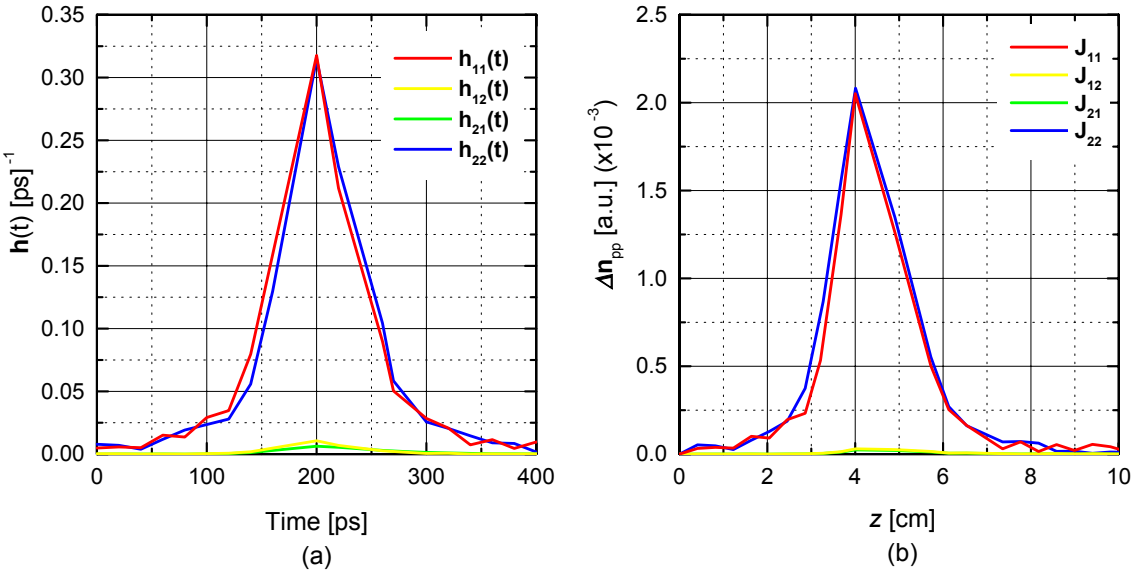

Figure 3.11: (a) Impulse response matrix elements $\mathbf{h}(t)$ and (b) vectorial grating structure $\Delta\mathbf{n}(z)$ of FBG in forward direction

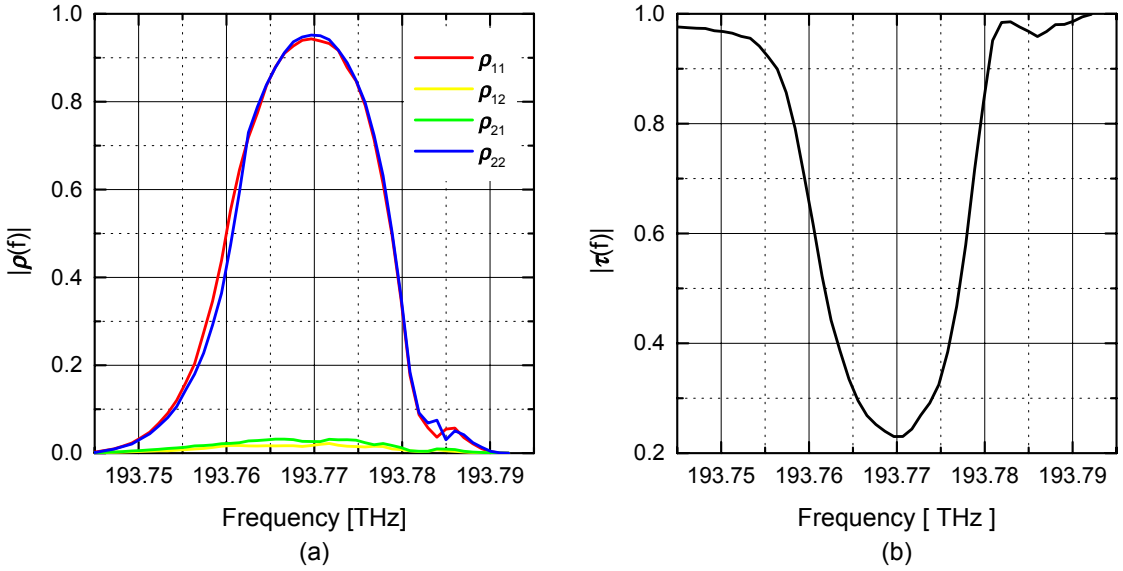

Figure 3.12: (a) 2x2 Jones reflectance matrix elements $|\boldsymbol{\rho}(f)|$ and (b) scalar transmission coefficient $|\tau(f)|$ of FBG in backward direction

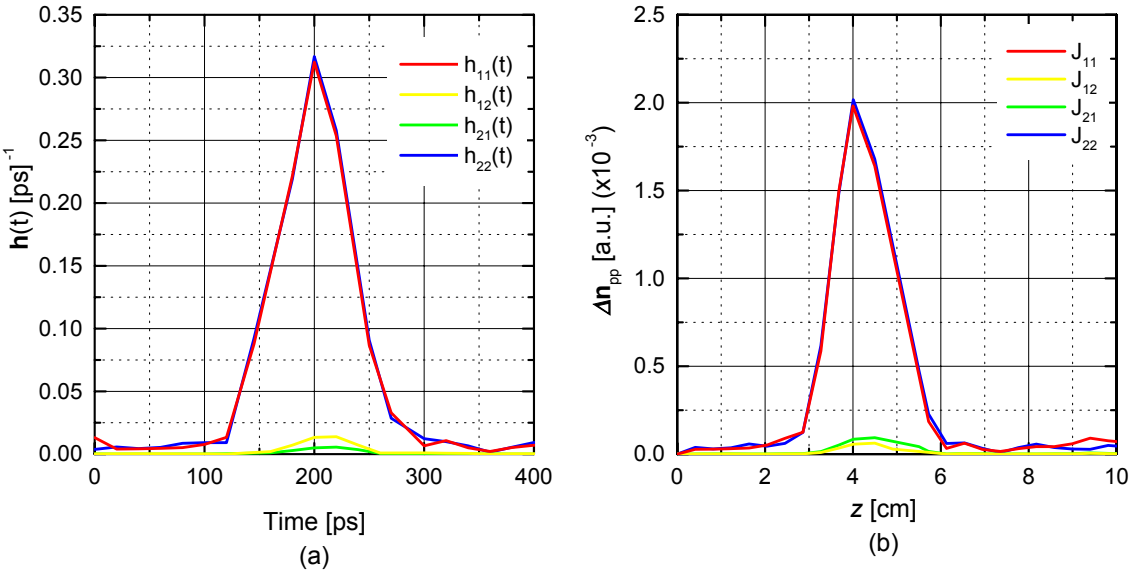

Figure 3.13: (a) Impulse response matrix elements $\mathbf{h}(t)$ and (b) vectorial grating structure $\Delta\mathbf{n}(z)$ of FBG in backward direction

Backward Measurement

Figure 3.12(a) shows the magnitude of the elements of the measured frequency-dependent complex reflectance matrix $|\boldsymbol{\rho}(f)|$ while Figure 3.12(b) shows magnitude of the scalar transmission coefficient $|\tau(f)|$ of the FBG in backward direction.

Figure 3.13(a) shows the impulse response matrix elements $\mathbf{h}(t)$ while Figure 3.13(b) shows the longitudinal grating structure $\boldsymbol{\Delta}n(z)$ with the corresponding grating burst for this FBG in backward direction.

Conclusion

This validates the measurement principle and the vectorial grating structure since "forward" and "backward" results agree very well. This grating is a very strong one and the calculated birefringence (not shown) of this commercial fiber Bragg grating was negligible. This commercial Bragg grating was also free from dichroism. The vectorial structure characterization results are summarized in [59].

3.4 Conclusion

The given FBG is evaluated for both scalar and vectorial structure characterization using the in-house developed integrated optical network analyzer. This would demonstrate the functionality and versatility of integrated optical circuits in lithium niobate and their direct application to optical instrumentation and communication.

Chapter 4

Integrated Optical PMD Compensator

4.1 Design Issues for Integrated Optical PMDC

Integrated Optical PMD compensator in X-cut, Y-propagation lithium niobate is designed, and characterized for different differential group delay profiles. It is based on cascaded TE↔TM mode converters with endlessly adjustable coupling phases. The natural birefringence (0.22 ps/mm) of this birefringent crystal cut can be used to compensate the DGD at the same time. Operational principle of this type of PMD compensator is described in the next section.

4.1.1 Operational Principle

The operational principle is based on the spatially weighted coupling between two waves with different propagation constants [20]. The phase difference between one mode and the coupled mode therefore depends on the position where coupling occurs and is periodic with the beat length $\Lambda = \lambda/\Delta n$. The TE–TM refractive index difference in a Ti-indiffused waveguide in X-cut, Y-propagation $LiNbO_3$ is $\Delta n = 0.0679$ at a free space wavelength $\lambda = 1550$ nm, thereby giving $\Lambda = 22$ μm. The interdigital electrodes are needed for phase matching with a period equal to one optical beat length, Λ. The widths and gaps are equal to $1/4$ of the optical beat length, and subsequent electrode pairs are additionally spaced by $3/4$ of the optical beat length which allows mode coupling to be adjusted in both quadratures endlessly via the electrooptic coefficient r_{51}. The coupling coefficient κ is given by

$$\kappa \cong \hat{\Gamma}(\pi/2)n^3 r_{51}(V/G)\lambda^{-1}, \tag{4.1}$$

where $\hat{\Gamma}$ is a weighted field overlap integral factor as defined later and $n = 2.1785$ is the average refraction index of the waveguide. $r_{51} = 28 \cdot 10^{-12}$ m/V is the relevant electrooptic coefficient and V is the interelectrode voltage.

Figure 4.1 shows the schematic of such PMD compensator in the X-cut, Y-propagation $LiNbO_3$. Voltage V_{1n} acts on one set of comb electrodes and performs mode conversion in phase. Voltage V_{2n} acts on another set of comb electrodes which are translated by $3/4$ of the

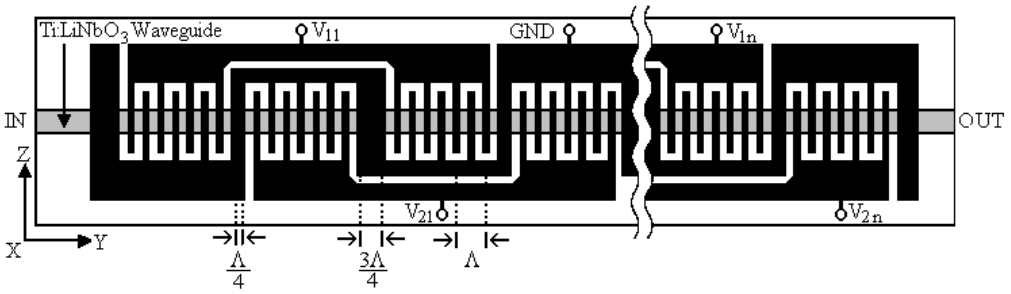

Figure 4.1: Schematic of PMD compensator on X-cut, Y-propagation $LiNbO_3$

optical beat length with respect to the first and performs mode conversion in quadrature. The resulting complex coupling coefficient is proportional to $V_{1n} + \jmath V_{2n}$ for n in-phase and quadrature electrode pairs. The need for 2 quadratures at least doubles the necessary chip length. The longitudinal electrode cross-section as well as local field overlap integral factors $\Gamma(y)$ for one quadrature of 2–phase TE–TM mode converter electrodes that are used in [22] are shown in Figure 4.2.

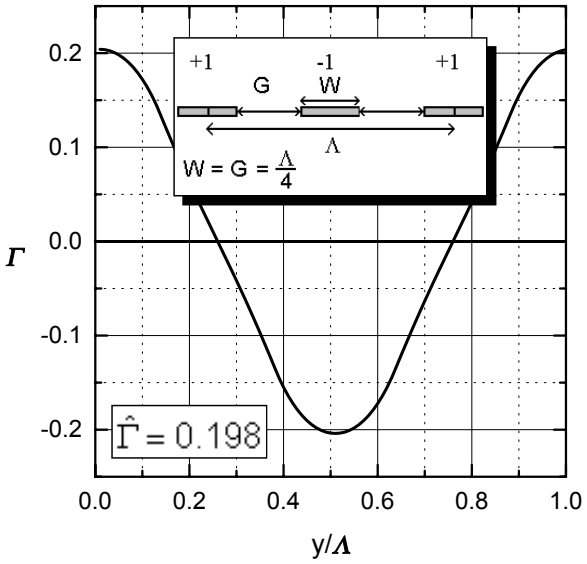

Figure 4.2: 2–phase electrodes with corresponding voltages and local field overlap integral factors vs normalized longitudinal coordinates

4.1.2 Two vs. Three Phases

As has been mentioned in [20], this 2–phase implementation is not the only possible choice. If isolated electrode crossings are available, 3–phase electrodes can be used with electrode widths and gaps equal to $\Lambda/6$. In-phase and quadrature mode conversion can be produced by the linear combinations of the "cosine" and "sine" cases as shown in Figure 4.3 and

Figure 4.4. Even and odd voltage distributions are applied by choosing electrode voltages $V_0 f(\hat{y})$ where V_0 serves as a reference voltage and $\hat{y}$ is the longitudinal position of the center of an electrode. Here $f(y) = cos(2\pi y/\Lambda)$ and $f(y) = sin(2\pi y/\Lambda)$ are structure functions needed for cosine and sine cases, respectively.

The Point Matching Method [40] has been chosen to calculate the electrostatic fields of these periodic electrode structures. The transversal optical field $\mathbf{E_o(x, z)}$ is assumed to be Gaussian and Hermite-Gaussian along width and depth of the single-mode Ti-indiffused waveguide in $LiNbO_3$ with mode field diameters matched to our experimental values. The position-dependent overlap integral $\Gamma(y)$ [39] must be multiplied by $f(y)$, integrated over one beat length and normalized to obtain the weighted overlap integral factor

$$\begin{aligned} \hat{\Gamma} &= \frac{2}{\Lambda}\int_0^{\Lambda} \Gamma(y) f(y) dy \quad \text{with} \\ \Gamma(y) &= \frac{G}{V}\frac{\int\int |\mathbf{E_o(x, z)}|^2 \mathbf{E_x(x, y, z)} dx dz}{\int\int |\mathbf{E_o(x, z)}|^2 dx dz}. \end{aligned} \tag{4.2}$$

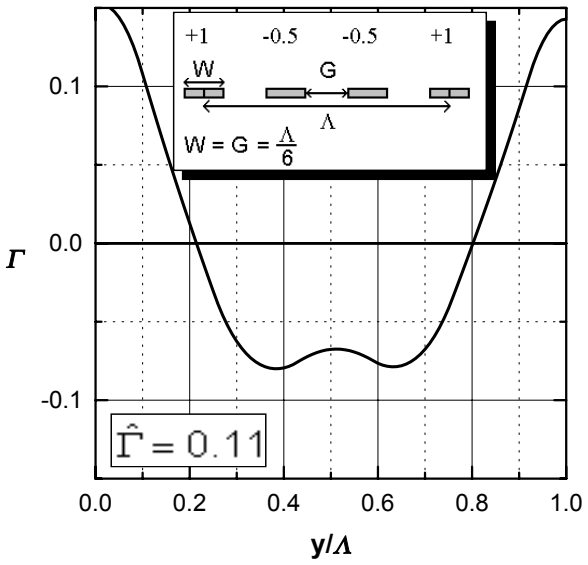

Figure 4.3: 3–phase cosine electrodes with corresponding voltages and local field overlap integral factors vs normalized longitudinal coordinates

For cosine and sine cases, $\hat{\Gamma}$ is the real or imaginary part of the spatial Fourier coefficient of $\Gamma(y)$, respectively. $\mathbf{E_x(x, y, z)}$ is the vertical component of the electrostatic field in the crystal. In $\Gamma(y)$ we have multiplied by the applicable gap G and divided by the maximum interelectrode voltage V as defined in (4.2). Figure 4.2 shows the local overlap factors $\Gamma(y)$ for one quadrature of the 2–phase TE-TM mode converter. For the two cases of the 3–phase TE-TM mode converters $\Gamma(y)$ is shown in Figure 4.3 and Figure 4.4. The resulting weighted overlap factors are $\hat{\Gamma} = 0.198,\ 0.11$ and 0.096, respectively. The 2–phase $\hat{\Gamma}$ is resized to an effective value of $\sim 0.086 \ldots 0.098$, if one takes into account

the fact that two quadratures of the 2–phase design need at least twice the length of the 3–phase design. If the maximum permissible field strength limits the design, the factor V/G in κ as defined in (4.1) is replaced by a constant. The 3–phase design performs in its worst case 0.096 roughly equal or slightly better than the 2–phase design. If the output range of the voltage sources is the limiting factor, κ as defined in (4.1) is obtained through a multiplication by the same V/G $(8/\Lambda,\ 9/\Lambda,\ 6\sqrt{3}/\Lambda)$ by which we have divided in calculating $\Gamma(y)$ as defined in (4.2). This yields equal κ values for both 3–phase cases, and these are $1.26 \ldots 1.44$ as high as κ in the 2–phase case. The above simulation results are published in [60].

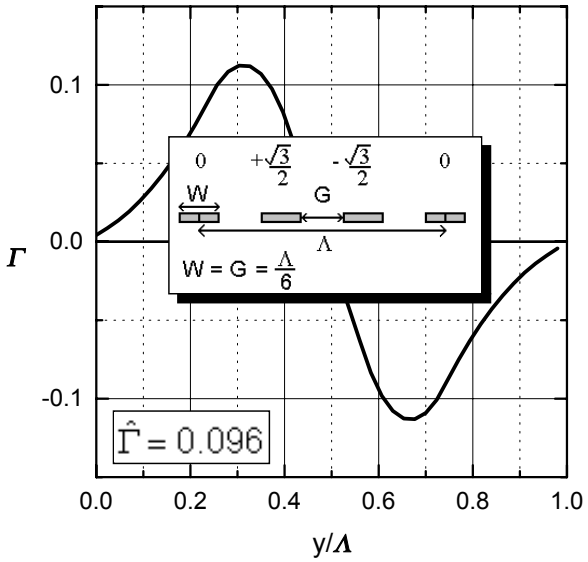

Figure 4.4: 3–phase sine electrodes with corresponding voltages and local field overlap integral factors vs normalized longitudinal coordinates

Figure 4.5 shows the photograph of a portion of the chip used in [22]. This device was fabricated by the Applied Physics group of Prof. W. Sohler, here at the University of Paderborn. This device was fiber pigtailed and packaged with slanted endfaces to improve the input/output optical return loss. The insertion loss was 4 dB and PDL 1.2 dB. Operating voltages were < 50 V. Thermal tuning is possible with 100 GHz/K.

4.1.3 New Proposals for High-Bit Rate PMD Compensators

This type of lithium niobate-based integrated optical PMD compensator (PMDC) should work up to at least 40 Gbit/s. At 160 Gbit/s a poor performance is to be expected because the experimentally needed length for one full mode conversion is on the order of 5 mm. This means that the corresponding DGD of about 1.2 ps is only partly orientable. However, PMD compensation at 160 Gbit/s or beyond seems to be mandatory to maximize dispersion-shifted fiber capacity, for example, in particular in all Japan. To reach higher

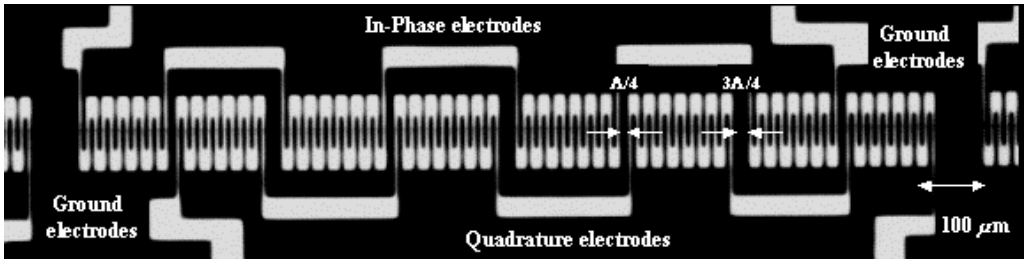

Figure 4.5: Photograph of in-phase and quadrature TE↔TM mode converter electrode pairs (in dark) on Ti:$LiNbO_3$ PMD compensator

and higher bit rates one needs to tailor the birefringence of lithium niobate. This is possible in principle in two ways: one possibility is to use tilted waveguide in YZ-plane which will reduce the birefringence and hence the differential group delay. The other possibility is to use the mixture of lithium niobate (LN) and lithium tantalate (LT) also known as lithium–niobate–tantalate (LNT).

Tilted Waveguide

We have also investigated the case of a larger Λ. For large Λ the electrical field reaches deeper into the waveguide and are also more uniform, thereby increasing the overlap integral as shown in Figure 4.6. Similar characteristics are found for all three cases. The weighted field overlap integral factor $\hat{\Gamma}$ grows almost $\propto \Lambda$ in the range considered.

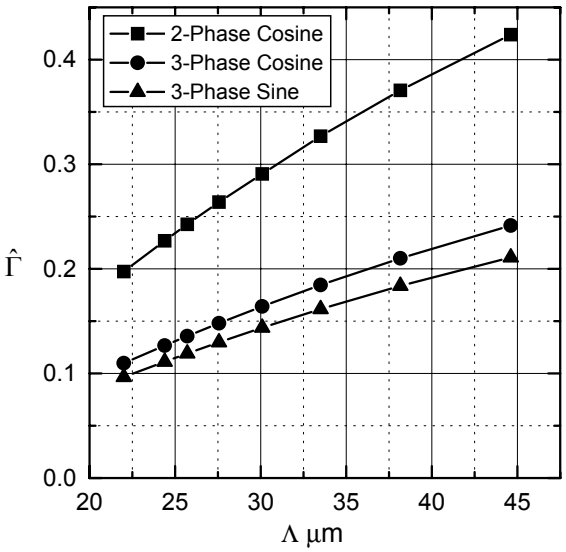

Figure 4.6: Weighted field overlap integral factor $\hat{\Gamma}$ as a function of beat length Λ in μm

A high $\Lambda \propto cos^{-2}\vartheta$ can be achieved in $LiNbO_3$ if the waveguide is tilted by an angle ϑ in the YZ plane. The coupling factor then becomes $\kappa(\vartheta) = \hat{\Gamma}(\pi/2)n^3\ (r_{51}cos\vartheta -$

$r_{22}sin\vartheta)(V/G)\lambda^{-1}$ with $n = n_o + (1/2)(n_e - n_o)cos^2\vartheta$ and $r_{22} = 6.8 \cdot 10^{-12}$ m/V. To give an example, for $\vartheta = -\pi/4$ the waveguide runs halfway between +Y and +Z axes. Λ doubles, $\hat{\Gamma}$ more than doubles, and $\kappa(-\pi/4) \cong 1.75 \cdot \kappa(0)$ in the field strength limited case. Furthermore, since the DGD per length is halved the DGD spent to implement a full mode conversion is ~ 3.5 times smaller than for Y–axis propagation. This means a 3.5 times more accurate PMD compensation becomes possible. However, twice as high a voltage V is required to keep V/G constant. Furthermore, a PMD compensator with a given length can compensate only half as much DGD. A large Λ is particularly advantageous if neither available driving voltages nor total chip length are limiting factors. This is the case at high bit-rates, say ≥ 40Gbit/s, where truly bad fibers have to be ruled out anyway.

It is indeed necessary to consider the substrate radiation modes which may cause high propagation losses in tilted waveguides. They may become significant when the waveguide is tilted in practice because the propagation constants of the guided mode and the substrate radiation mode may become identical. However no attempt has been made to verify this possibility independently as it is clear from [61, 62].

Lithium–Niobate–Tantalate Crystals

The mixed ferroelectrics have been the focus of intensive fundamental and applied research for many years. Interest in the study of these materials arises from the fact that the physical properties of crystalline materials are governed to a large extent by the composition of the crystals. Therefore, the physical properties can be tuned by varying the composition. One of the simplest ferroelectric mixed crystal systems is lithium–niobate–tantalate, as both end members exhibit the same crystal structure (space group *R3c*) with only slight differences in the lattice and positional parameters. The physical properties can be very easily tuned by varying the parameter y in the composition of LNT crystals. To a certain degree, the mixed system yields a simple crystal modelling that may lead to functional materials and devices, which has direct implication for PMD compensation in optical communication. Lithium niobate is a slightly nonstoichiometric, typically Li-deficient, preferably grown at the congruently melting composition with 48.5 Mol% of Li2O. A large variety of dopants ranging from +1 valent state H+ to the +3 valent state such as rare earth cations can be introduced into the crystal structure frame of lithium niobate. Most are known to occupy Li-sites. In contrast to these Li-site dopants, tantalum is isomorphic to niobium and replaces niobium when introduced into the crystal structure frame of LN. Tantalum can substitute niobium up to 100%. Any changes in the crystal composition will finally affect all physical properties of the crystal such as the linear dielectric response, i.e. refractive index, electro-optic coefficients and so on. It has been shown in [63] that refractive index and electro-optic coefficients depend linearly on the Ta content y in LNT crystals. Therefore one can tailor the birefringence of this mixed crystal especially for PMD compensation at higher bit rates.

The ordinary refractive index n_o and the relevant electro-optic coefficient r_{51} depend linearly on the Ta content y in LNT crystals: $n_o = 2.2125 - 0.07y$, and $r_{51} = 28 - 8y$. Figure 4.7 shows the calculated optimum weighted field overlap integral factor $\hat{\Gamma}$, as defined in [60], for 2-phase as well as two representative cases of 3-phase TE-TM mode converters

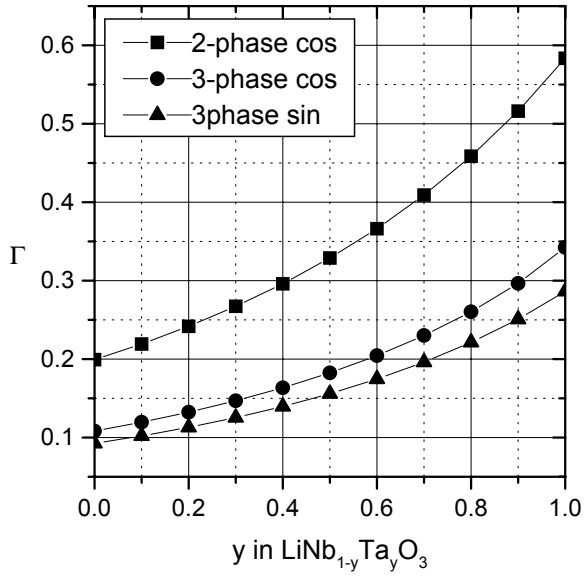

Figure 4.7: Weighted field overlap integral factor $\hat{\Gamma}$ as a function of Ta content y in lithium–niobate–tantalate crystals

with interdigital electrodes. The numbers can be directly compared if the 2-phase $\hat{\Gamma}$ has been halved due to the fact that the 2-phase design need at least twice the length of the 3-phase design. Using this $\hat{\Gamma}$ and assuming 2-phase electrodes, the achievable number of full mode conversions per DGD at electric field strength near breakdown (10 V/mm), and the required length per DGD have been calculated as a function of the Ta content y in the LNT crystals (Figure 4.8). Pure LN allows for ≈ 8 full mode conversions / ps in theory if $\hat{\Gamma} = 1$, and ≈ 0.8/ps experimentally, in agreement with theory ($\hat{\Gamma} \approx 0.1$). Pure LT allows for 20 time more mode conversions/DGD. The length/DGD is ≈ 4.2 mm/ps in LN, and ≈ 42 mm/ps in LT. But this should not be problematic since less PMD may be expected in links for highest bit rates. LT alone should work in principle up to at least 640 Gbit/s. Appreciable advantages over pure LN with the potential of reaching 160 Gbit/s can also be expected for low y which may be accessible either by incorporating Ta into LN during crystal growth or later by thermal in-diffusion. An interesting situation occurs near $y = 0.9$ where the sign reversal of Δn promises Tbit/s PMD compensation. A major problem for large y in LNT and pure LT are the large beat lengths, which scale proportional to the length/DGD. High voltages are required to reach fields near breakdown, even for 3-phase electrodes where the gaps are smaller (≈ 370 V in LT).

4.1.4 Conclusion

We found that a 3–phase TE-TM mode converter can (but need not in all cases) outperforms a 2–phase one. Tilting the waveguide in the YZ plane can drastically increase the efficiency

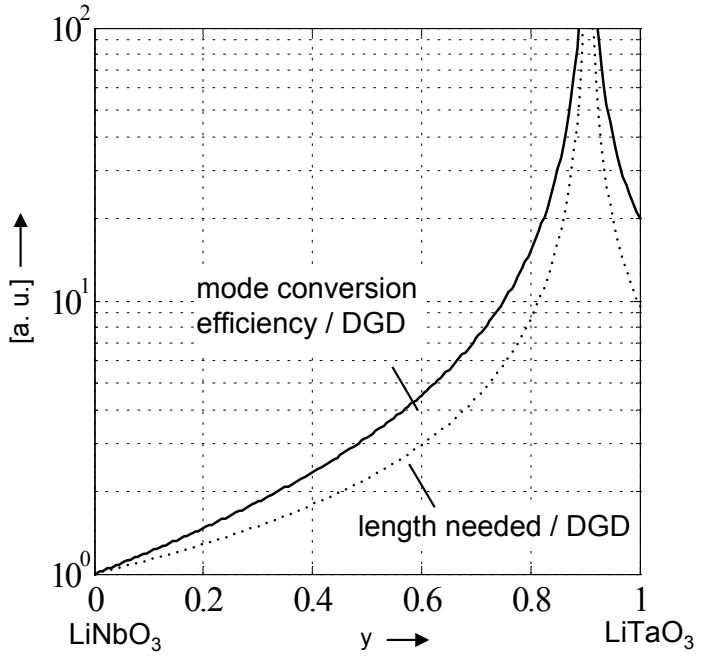

Figure 4.8: Mode Conversion/DGD and length needed/DGD for a TE↔TM in LNT crystals as function of Ta content y

but the leaky modes losses are the main issues involved in its realization. The other possibility is to use mixed ferroelectric crystals such as the lithium–niobate–tantalate to realize high bit rate PMD compensators where just a little DGD needs to be compensated. The birefringence Δn and electrooptic coefficient r_{51} decreases linearly with increasing the Ta content y in LNT crystals. A Ta content y of up to 0.5 is good to realize a PMD compensator at about 160 Gbit/s. These two possibilities are explored and the simulation results are summarized in [24]. These solutions combines optimum performance and high-speed with a high degree of integration and hence low cost potential.

4.2 DGD Profile Characterization

Different kinds of PMD compensators (PMDCs) based on all optical as well as electrical filters have been demonstrated or proposed. Most of these were designed for first-order PMD compensation. PMDCs suitable for higher order compensation like the one described above is proposed by R. Noé [19]. Experimental validation of such a filter is not have been reported so far nor a PMD medium with complicated structure have been analyzed. B. L. Heffner first demonstrated the use of Jones matrix eigenanalysis technique to accurately measure both the PSP and DGD as a function of optical frequency. This has allows to verify the structure with only 3 known DGS section which were precharacterized [64, 65]. On the other hand, L. Möller from Bell Labs has synthesized a 2x2 Jones matrix filter

for broadband PMD compensation [66] generalizing the basic work done by S. E. Harris and his coworkers [67]. Later on A. Eyal and A. Yariv also simulated this concept for minimization of the maximum differential group delay within a given frequency band for broadband PMD compensation filters [68]. In Möller's paper, a synthesis algorithm and a design concept that descends directly from Ozeki [69] is described. Filter types which were proposed by R. Noè can not only be represented but also analyzed by means of this algorithm. Therefore, we proposed a nondestructive method based on this algorithm for determining the DGD profiles. This method would be of particular help for identification, emulation, and compensation of higher-order PMD effects that persists after compensation of first-order PMD.

4.2.1 Measurement Setup

A measurement setup consist of external cavity tuneable laser source, an integrated optical network analyzer circuit having on chip broadband electrooptic polarization transformers which are based on X-Cut, Z-propagation $LiNbO_3$ and a set of two polarimeters. External cavity tunable laser source is connected to the input of the fiber pigtailed and packaged integrated optical network analyzer circuit. This integrated optical circuit is used to split the laser signal between the reference and measurement branch. Electrooptic polarization transformer which is on the measurement branch is used to generate 8 different polarization states that are equally distributed onto the Poincar sphere. These output polarization states are given as input to the device under test. The output of the reference branch is given to reference polarimeter through ≈ 25 ps DGD section and it works as a frequency meter for frequency correction. A measurement polarimeter is connected to the output of the device under test. The laser is swept in the steps of 10 GHz between the 1525 nm and 1545 nm where it had no mode hops. Figure 4.9 shows the measurement setup.

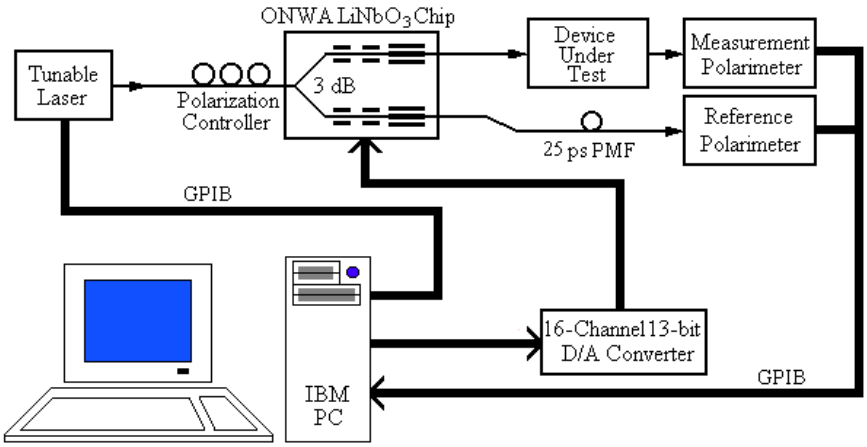

Figure 4.9: Measurement setup for DGD profile characterization

The frequency-dependent 3x3 rotation matrix $\mathbf{R}$ of the device, i.e. rows and columns 2 to 4 of its Müller matrix are thereby measured. Each of the n (= 8 in our case) normalized input (in) Stokes vectors results in corresponding output (out) Stokes vectors. Both vector groups are arranged in form of a matrix

$$\mathbf{S}_{\mathrm{out}} = \mathbf{R}\mathbf{S}_{\mathrm{in}}. \tag{4.3}$$

The rotation matrix $\mathbf{R}$ is then obtained by

$$\mathbf{R} = \mathbf{S}_{\mathrm{out}}\mathbf{S}_{\mathrm{in}}^{\mathrm{T}}(\mathbf{S}_{\mathrm{in}}\mathbf{S}_{\mathrm{in}}^{\mathrm{T}})^{-1}. \tag{4.4}$$

Compared to a more compact method [70] with two launched polarizations this gives a better immunity against polarization measurement errors. Any existing nonorthogonality of R is removed by singular value decomposition of R according to

$$\mathbf{R} = \mathbf{u}\mathbf{s}\mathbf{v}^{\dagger}, \tag{4.5}$$

where $\mathbf{u}$, and $\mathbf{v}$ are orthogonal (or more generally: unitary) matrices and $\mathbf{s}$ is a diagonal matrix with the singular values. $\mathbf{R}$ is then redefined as an orthogonal matrix

$$\mathbf{R} = \mathbf{u}\mathbf{v}^{\dagger}. \tag{4.6}$$

From this frequency-dependent rotation matrix, $\mathbf{R}$, the frequency-dependent Jones matrix, $\mathbf{J}$, is obtained in the form

$$\mathbf{J} = \begin{pmatrix} A & B \\ -B^{*} & A^{*} \end{pmatrix}, \quad |A|^2 + |B|^2 = 1. \tag{4.7}$$

The frequency domain results are multiplied by a $\cos^2$ window centered at 1535 nm to suppress errors introduced by the discontinuous borders. The inverse Fourier transform yields the time-dependent Jones matrix with impulse response as elements. Its first column is the finite impulse response to a horizontally polarized pulse while last column is the finite impulse response to an orthogonally polarized pulse (vertical). It is sampled with a 785 fs period. The structure is analyzed on the basis of sections having DGDs equal to this value. The following section gives the core of the inverse scattering algorithm.

4.2.2 Inverse Scattering Algorithm

Analysis by means of an impulse response is a concept that is familiar to the electrical engineers. If an impulse i.e. a Dirac delta function is applied to a linear time independent network, the Fourier transform of the impulse response of the network is the frequency domain transfer function of the network.

We first consider the impulse response of the single birefringent crystal (e. g. polarization maintaining fiber) of Figure 4.10. The crystal is cut with its optic axis perpendicular to its

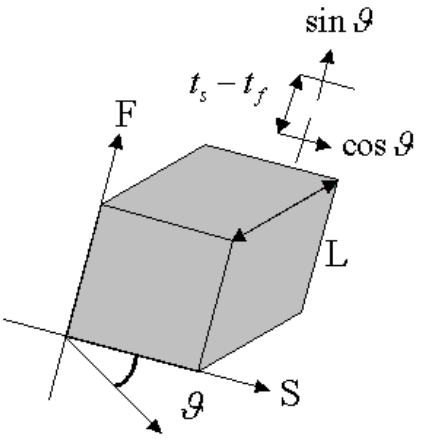

Figure 4.10: Impulse response of a single birefringent crystal

length and with end faces flat and parallel. A linearly polarized impulse of the optical electric field is assumed to be normally incident on the crystal. Since the incoming signal is normally incident, double refraction will not occur. The impulse will divide into two orthogonally polarized impulses whose amplitudes depend on the polarization of the incident impulse with respect to the principle axes of the crystal. These two impulses travel with different velocities and therefore, emerge at different times. The difference in time at which they emerge from the crystal is given by

$$t_{\mathrm{F}} - t_{\mathrm{S}} = \frac{L\Delta n}{v}, \tag{4.8}$$

where Δn is the birefringence of the crystal of length L, and v is velocity of the light in the crystal.

Next, we would like to consider the impulse response of n birefringent crystals of arbitrary birefringence, lengths, and orientations. In general, we can draw some conclusions: Impulse response of n birefringent crystals is a set of $2n$ impulses of finite duration. The magnitude and polarization of these impulses are determined by the crystal orientations while their relative times of emergence is determined by birefringence and lengths of the crystals used. The most important conclusion is that the impulse response of series of birefringent crystals is a train of impulses of finite duration. In contrast, the impulse response of Fabry-Perot and multilayer dielectric-film filters consist of infinite train of impulses.

At the outset, two points should be stressed. First, it is assumed that the birefringent crystals within the network are lossless. This means that at all points between first and last crystal energy must be conserved. Energy conservation principle puts certain restrictions on the impulse which have travel along fast (F_n^n) and slow (S_n^n) axes respectively. This condition is give by

$$F_0^n F_{n-1}^n + S_1^n S_n^n = 0. \tag{4.9}$$

Second, it should be noted that

$$F_n^n = S_0^n = 0. \tag{4.10}$$

This is just the statement of the fact that the first and last impulses out of n^{th} crystal must have propagated along its fast and slow axes, respectively.

To do analysis of such a chain of crystals of arbitrary birefringence, orientation, and lengths, one can write an expression relating the input and output of each crystals. Angle (Θ) represents the input coupling ratio and is known as orientation angle while angle (Ψ) represents the retardation or the differential phase. Therefore, one can write for the output of the first (4.11-a), second (4.11-b), and third (4.11-c) crystals, respectively.

$$\begin{pmatrix} F_0^1 \\ S_1^1 \end{pmatrix} = \begin{pmatrix} -\sin\Theta_1 e^{+\jmath\Psi_1} \\ \cos\Theta_1 e^{-\jmath\Psi_1} \end{pmatrix} \begin{pmatrix} I_0^0 \end{pmatrix} \tag{4.11-a}$$

$$\begin{pmatrix} F_0^2 \\ F_1^2 \\ S_1^2 \\ S_2^2 \end{pmatrix} = \begin{pmatrix} \cos\Theta_2 e^{+\jmath\Psi_2} & 0 \\ 0 & -\sin\Theta_2 e^{+\jmath\Psi_2} \\ \sin\Theta_2 e^{-\jmath\Psi_2} & 0 \\ 0 & \cos\Theta_2 e^{-\jmath\Psi_2} \end{pmatrix} \begin{pmatrix} F_0^1 \\ S_1^1 \end{pmatrix} \tag{4.11-b}$$

$$\begin{pmatrix} F_0^3 \\ F_1^3 \\ F_2^3 \\ S_1^3 \\ S_2^3 \\ S_3^3 \end{pmatrix} = \begin{pmatrix} \cos\Theta_3 e^{+\jmath\Psi_3} & 0 & 0 & 0 \\ 0 & \cos\Theta_3 e^{+\jmath\Psi_3} & -\sin\Theta_3 e^{+\jmath\Psi_3} & 0 \\ 0 & 0 & 0 & -\sin\Theta_3 e^{+\jmath\Psi_3} \\ \sin\Theta_3 e^{-\jmath\Psi_3} & 0 & 0 & 0 \\ 0 & \sin\Theta_3 e^{-\jmath\Psi_3} & \cos\Theta_3 e^{-\jmath\Psi_3} & 0 \\ 0 & 0 & 0 & \cos\Theta_3 e^{-\jmath\Psi_3} \end{pmatrix} \begin{pmatrix} F_0^2 \\ F_1^2 \\ S_1^2 \\ S_2^2 \end{pmatrix} \tag{4.11-c}$$

Since the pattern has be established, one can write an expression for the output from the n^{th} crystal (4.11-d).

$$\begin{pmatrix} F_0^n \\ F_1^n \\ \vdots \\ F_{n-1}^n \\ S_1^n \\ S_2^n \\ \vdots \\ S_n^n \end{pmatrix} = \begin{pmatrix} \cos\Theta_n e^{+\jmath\Psi_n} & 0 & \dots & 0 & 0 \\ 0 & \cos\Theta_n e^{+\jmath\Psi_n} & \dots & 0 & \vdots \\ \vdots & 0 & \dots & -\sin\Theta_n e^{+\jmath\Psi_n} & 0 \\ 0 & \vdots & \dots & 0 & -\sin\Theta_n e^{+\jmath\Psi_n} \\ \sin\Theta_n e^{-+\jmath\Psi_n} & 0 & \dots & \vdots & 0 \\ 0 & \sin\Theta_n e^{-+\jmath\Psi_n} & \dots & 0 & \vdots \\ \vdots & 0 & \dots & \cos\Theta_n e^{-+\jmath\Psi_n} & 0 \\ 0 & 0 & \dots & 0 & \cos\Theta_n e^{-\jmath\Psi_n} \end{pmatrix} \begin{pmatrix} F_0^{n-1} \\ \vdots \\ F_{n-2}^{n-1} \\ S_1^{n-1} \\ \vdots \\ S_{n-1}^{n-1} \end{pmatrix} \tag{4.11-d}$$

This is a set of non-homogeneous equations and has a solution if and only if the rank of the matrix of the coefficients is equal to the rank of the augmented matrix. Several possibility exists for determining the rank of the matrix. Applying one of these criteria, we

get an expression

$$\tan \Theta_n e^{j2\Psi_n} = -\frac{F_{n-1}^n}{S_n^n} \tag{4.12}$$

that relates orientation and retardation angles with the impulse response elements. The calculation is an easy one, involving for any stage no more than the solution of only two simultaneous equations.

Our procedure is to start with the output from the n^{th} crystal. From these two impulse response elements F_{n-1}^n and S_n^n, we can calculate the crystal angles Θ_n and Ψ_n or the mode conversion effect and the input to this crystal (F_n^{n-1} and S_n^{n-1}). Since the input to the n^{th} crystal is nothing but the output of the $(n-1)^{\text{th}}$ crystal. Thus we work our way back through the entire network alternately finding crystal angles and crystal inputs. Successive repetition of this procedure yields the input vector which is two element smaller than the output vector. Finally, when all crystal angles are found out, one is left with a two element vector with one zero element that describes the input signal.

We have used a matrix of an elliptical retarder to describe the mode conversion effect instead of the one used by S. E. Harris [67] or L. Möller [66] because transmission fiber can have not only linear birefringence (due to core ellipticity, micro-bending, transverse stress) but also circular birefringence (due to fiber twist) and may vary along the fiber [18]. Single-mode fiber must, therefore, be represented by an elliptical retarder matrix at a given optical frequency.

Our inverse scattering algorithm can display a full length DGD profile with 40 sections. Experimentally inverse scattering range was chosen to be ≈ 31.5 ps.

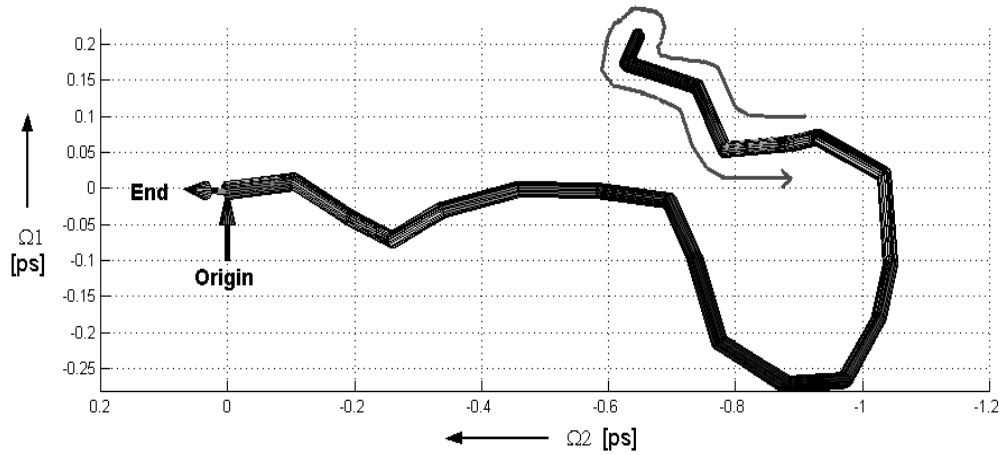

Figure 4.11: DGD profile for back-to-back measurement

4.2.3 DGD Profiles in Fibers

At first a back-to-back measurement without DUT was performed. In this case, all DGD sections (= rods) should be cancelled by oppositely directed adjacent ones. This is indeed

the case in the above Figure 4.11. The DGD profile travels 20 sections forth, then another 20 sections back on the same path, as if returning from a dead end. As a consequence, one has the impression to see only 20 sections, which in reality hide the other 20 sections. Input arrow tip and output arrow back end coincide within < 100 fs which is a measurement error since the true DGD was ~ 0 fs. So the simplified back-to-back DGD profile is a frequency-independent polarization transformation specified by the arrows where input and output arrows indicates the local principle states of polarization of the relevant DGD-sections.

Next DUT was a ~ 11 m long polarization maintaining fiber (PMF) with ≈ 25 ps of DGD. It yielded a straight, 25.12 ps long line (32 sections) followed by a short dead end of 2×4 sections (Figure 4.12).

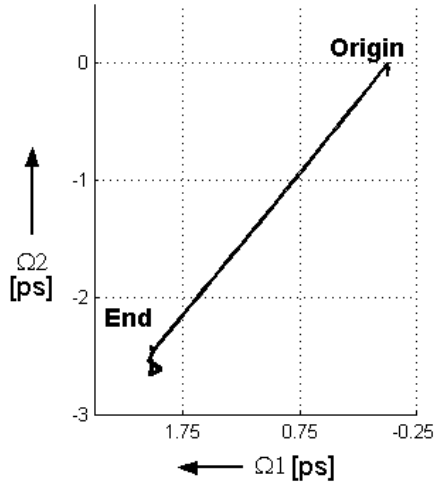

Figure 4.12: DGD profile of one ≈ 25 ps DGD section

Figure 4.13 shows a DGD profile when two pieces of PMF each with ~ 22 ps and ~ 6 ps of DGD are concatenated with $50\ \%$ mode conversion ($45°$ rotation) in between. The long section and the short section which also contains a short dead end of 2×1 section are clearly identified. Angle between the sections was $\approx 90°$ as expected.

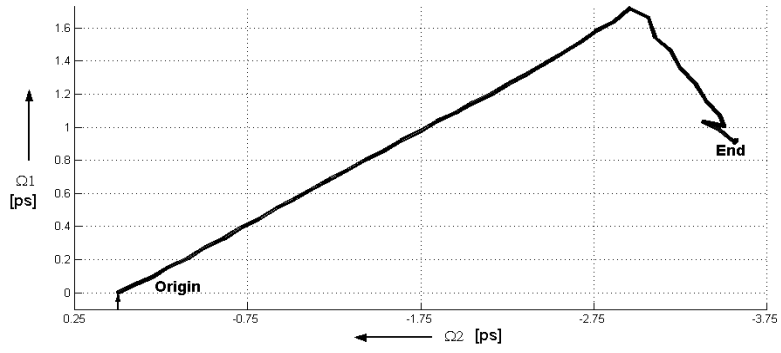

Figure 4.13: DGD profile of two (≈ 22 ps and ≈ 6 ps) DGD sections with $50\ \%$ mode conversion in between

4.2.4 DGD Profiles of Distributed PMD Compensator in $LiNbO_3$

Fiber-pigtailed and packaged X-cut, Y-propagation $LiNbO_3$-based PMD compensator was fabricated in-house, similar to that in [22]. About 70 in-phase and quadrature TE-TM mode converters were distributed over 95 mm long waveguide. An average DGD was about 25 ps. Without any applied voltages the DGD profile was similar to that of Figure 4.10. Figure 4.14 shows the DGD profile bent into a full circle when two full mode conversions were distributed over the whole chip occur in one quadrature. A dead end with approximately 2×4 sections is also seen because the total DGD value of the chip is less than inverse scattering range. Pigtail-shaped profile of Figure 4.15 results when only one and half mode conversions occur in one quadrature, but they were concentrated at about $3/4$ of the total DGD. This demonstrates the versatility of the distributed PMD compensator with respect to emulation and compensation of higher-order PMD effects which persists after compensation of first-order PMD.

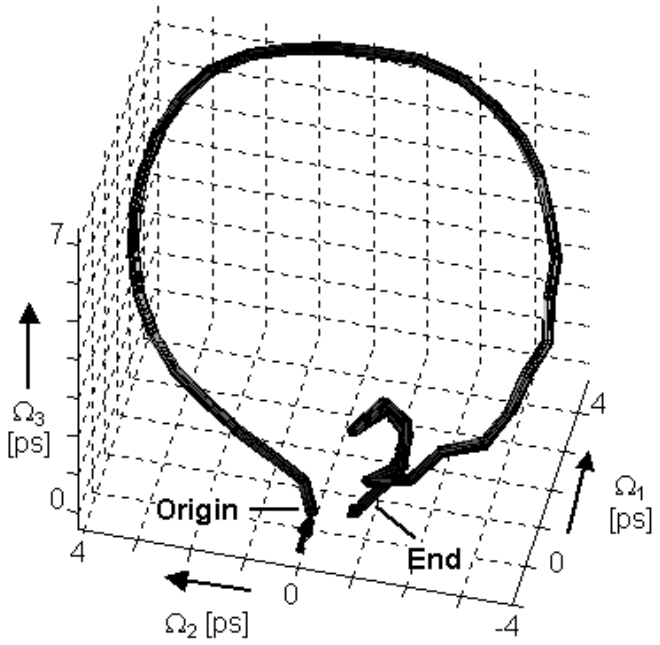

Figure 4.14: DGD profile of $LiNbO_3$ PMDC with 2 full mode conversions distributed over whole chip length in one quadrature

4.2.5 Conclusion

The frequency-dependent reduced Müller matrix measurement enables us to calculate the corresponding Jones matrix and hence the impulse response of the devices with polarization

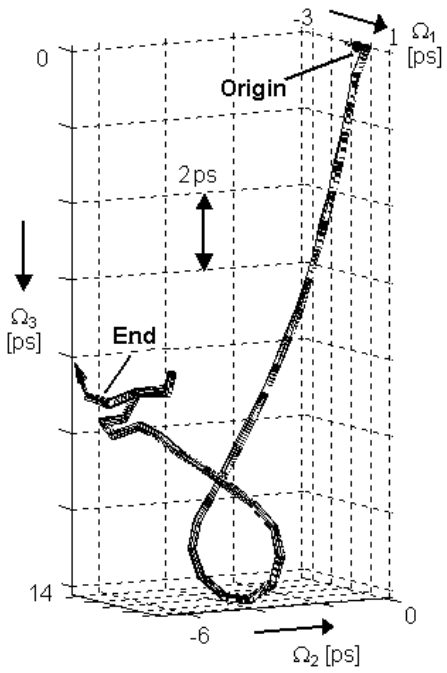

Figure 4.15: DGD profile of $LiNbO_3$ PMDC with 1 and 1/2 mode conversions distributed over whole chip length in one quadrature

mode dispersion. From the latter, the differential group delay profiles are determined by inverse scattering. These results are summarized in [71]. These allow to identity, emulate and compensate the effects of higher-order PMD that persists after compensation of first-order PMD.

4.3 Conclusion

An integrated optical PMD compensator is designed and optimized for maximum electro-optic efficiency. PMD compensator for high bit rate applications are not only proposed but also evaluated for their performance. This includes the use of tilted waveguides or mixed ferroelectric materials such as lithium–niobate–tantalate crystals where birefringence and hence DGD can be tailored. This is particulary advisable at data rates of 40 Gbit/s and beyond where small DGD needs to be compensated. An inverse scattering algorithm is implemented for characterizing the devices with PMD. Some fiber and integrated optical devices with PMD are characterized for different DGD profiles using in-house developed integrated optical network analyzer. The versatility of such a PMDC is demonstrated and is found to be suitable for generation and compensation of higher-order PMD effects.

Chapter 5

Result Discussion and Future Scope

The integrated optical network analyzer based on X-cut, Z-propagation lithium niobate for the vectorial structure characterization of optical fiber Bragg gratings is reported. The frequency-dependent complex reflectance Jones matrix is measured by interferometry and transformed into time-domain. From the impulse response matrix, the vectorial grating structure is determined by inverse scattering. Optical network analyzer was also used to measure frequency-dependent Müller matrix of the optimized polarization mode dispersion compensator in X-cut, Y-propagation lithium niobate and its different differential group delay profiles are determined by inverse scattering using time domain impulse response.

5.1 Characterization of $LiNbO_3$-based IOC

On this integrated optical circuit several optical components such as polarizers, phase shifters, and broadband TE↔TM mode converters are integrated onto each branch of the 3 dB optical power splitter. This IOC together with the 3x3 fiber coupler forms a measurement interferometer. Initially, all of the above mentioned components are integrated onto a test substrate. This test circuit was used to evaluate the performance of each of these integrated optical components. Indeed this has complicated the whole work. Several problems were encountered during the entire development of this integrated optical circuit and are listed below.
(1) Higher propagation losses for TE-polarized modes
(2) Poor power splitting uniformity of the 3 dB optical power splitter
(3) Poor polarization extinction ratio of on-chip TE-pass polarizers
(4) Static TE–TM mode conversion
(5) Nonideal behavior of on-chip TE–TM mode converters

Step by step the characterization data was analyzed. Latter on, the device fabrication steps were also reviewed. It was found from the device fabrication history that this test integrated optical circuit was not realized using the principal-axis (Z-axis) propagation but was realized to use near-Z-axis propagation. Specifically, the substrate was cut an angle of 2° degrees with respect to the principal Z-axis. This off-axis propagation was used to

compensate the modal birefringence and to make the on-chip TE–TM mode converters more efficient.

Ti-indiffused channel waveguides in $LiNbO_3$ themselves were having low propagation losses. But the developed device shows very high insertion loss due to the fact that 1.5 mm long TE-pass polarizes were realized directly on top of the waveguide using an aluminum as a cladding metal. This not only gave excess propagation losses (first issue) but also the differential propagation losses for TE-polarized modes. This resulted into poor power splitting ratios for the TE-polarized modes (second issue), due to nonuniform metal cladding. It also resulted in poor polarization extinction ratios for the TM-polarized modes (third issue).

This off-axis propagation results in the undesired static mode conversion. This not only makes the polarizers but also mode converters nonideal. This is because the TM-polarized mode is regenerated in the waveguide after TE-pass polarizers. This regenerated TM-polarized mode degrades the polarization extinction ratio of the on-chip polarizers (third issue). Whether one physically rotates the direction of propagation in the YZ-plane globally or rotate the index ellipsoid electro-optically in the YZ-plane locally, the net modal birefringence compensation effect is the same. In this compensation process, one always ends up with the undesired imaginary coupling coefficient between two, otherwise, orthogonally polarized modes and this mode coupling results in the undesired static mode conversion (fourth issue). If one compensates for this modal birefringence globally, then the phenomenon is length-dependent and beyond any physical control due to inherent lithium niobate anisotropy. If one compensates for it locally, then it is field-dependent (fifth-issue). In principle, it is possible to compensate for this undesired polarization mode coupling electro-optically.

The only option to reduce this undesired static mode coupling is to fabricate optical waveguides along the principal axis. It is to be ensured that the waveguide is exactly parallel to the Z–axis during photolithography. Otherwise, the $LiNbO_3$-anisotropy will play the undesired role. If the waveguide is exactly parallel to the Z-axis then the voltages required for compensation are ideally symmetric; otherwise, they are asymmetric in practice. Of course a relatively high bias voltages will result.

Therefore, in the next generation of these integrated optical circuits, principal-axis propagation was used. Each component is fabricated separately on a Ti in-diffused optical channel waveguide in lithium niobate and characterized rigorously to give feedback to device fabrication steps and for the design of new versions of the mask plates. Three design iterations were done including the mask design in order to achieve the target specifications set for this integrated optical circuit. The issues which were resolved and gave significant improvement are summarized below.

The only remedy to improve the performance of the polarizers was to use principal-axis propagation for device development. The other possibility was to introduce a buffer layer of right dielectric constant and right thickness in between the waveguide and aluminum metal cladding so as to improve the phase matching condition between the surface plasmon mode and the TM-polarized mode. Both options were implemented. They have drastically

improved the polarization extinction ratio of the TE-pass polarizers and minimized the excess propagation losses for the TE-polarized modes. Several materials have been tried out. It was found out experimentally that 27 nm thick yttrium oxide based polarizers gave an extinction ratio of ≈ 30 dB for 3 mm long polarizers with 500 nm thick aluminum metal cladding. To some extent, this solution has also improved uniformity of power splitting for the TE-polarized modes.

Several 15 mm and 20 mm long phase shifters were realized on straight optical channel waveguides. They were characterized using the Fabry-Perot technique. Voltage x length product for these phase shifters was found out to be 60 V-cm.

The mode converters with 30 mm long electrodes with 6 and 8 μm gaps were characterized. The voltage required for full TE-to-TM mode conversion and vice-versa was 10 V. Needed bias voltages were ± 38 V.

5.2 Longitudinal Structure Characterization

Optical frequency domain interferometry was used in the longitudinal structure characterization of optical fiber Bragg gratings. Once the frequency-dependent complex reflection coefficient for reflective devices or complex transmission coefficient for transmissive devices under test are measured correctly in the frequency domain then the task of deriving the longitudinal structure is straight forward. This type of optical characterization method needs high-speed, single-frequency, broadband tunable laser. The tuning range limits the spatial resolution but large grating lengths may be investigated due to high coherence of a single-mode laser. Such type of lasers are very difficult to find in the shops. External cavity single-frequency tunable lasers with sweeping option are now commercially available in the shops but are very expensive.

The integrated optic on-chip phase modulators are used for digital phase shifting and performs AC rather than DC measurement in order to increase sensitivity. In fact, these phase modulators on X-cut, Z-propagation lithium niobate are also not ideal if the polarity of the applied voltages is such that it reduces the modal birefringence then the net effect is that this applied voltages creates an electric field E_y which will cause both stretching of the index ellipsoid along the principal-axes as well as the rotation of the index ellipsoid cross-section in the yz-plane. This indeed gives undesired static mode conversion. There are polarizers after the phase shifters which are used to suppress negative frequencies generated due to serrodyne modulation; in fact, these polarizers do convert these polarization changes into undesirable intensity changes. One solution was to found out the correct polarity of the applied voltages so that only phase is modulated and not the polarization. These measures were taken into account while configuring the hardware of the network analyzer. This concept of digital phase shifting to increase sensitivity was successfully demonstrated but finally was not used for measurement because it simply took more recording time. Especially, for such interferometric measurements, the measurement time has to be shortest in order to minimize the DC thermal drift. There is always a trade off between sensitivity and DC thermal drift.

Initially, tunable twin-guide laser was employed as tunable laser sources for measurements. Unfortunately, this laser died due to malfunction in the laser control unit. In fact, the temperature controller failed to work. Latter on, narrow linewidth DFB lasers from two well known companies were tried out during this work. The Furukawa laser was having very strange behavior and could not be used even for scalar measurement. On the other hand, JDS-uniphase laser worked satisfactorily for scalar measurements. But JDS-uniphase laser was never stable within the scan and from scan-to-scan. Moreover, the TE–TM mode converters also had severe DC drift. This gave lot of problems in finding the common phase for implementing the orthogonalization scheme devised by D. Sandel. Therefore, instead of using this scheme, the on-chip TE–TM mode converters were calibrated with respect to the commercial rotating waveplate polarimeter to generate orthogonal pairs for the vectorial measurements.

One uniform fiber Bragg grating at 1548.25 nm of $> 95\%$ reflectivity and 0.2 nm bandwidth is characterized for longitudinal structure in order to demonstrate the utility of this integrated optical network analyzer. The results are summarized in chapter 3. The longitudinal structure of this commercial fiber Bragg grating showed a single burst. This was also free from birefringence and dichroism. Shortcoming of this method is that it needs single-frequency, broadband, and high-speed, tunable laser source. Future scope would be either to realize it somehow or to buy such laser with sweeping option and integrate it with the integrated optical network analyzer to complete this work.

5.3 Integrated Optical PMD Compensator

The integrated optic TE–TM mode converters are optimized to have highest electro-optic efficiency by simulation studies. Two-phase verses three-phase TE–TM mode converters are compared and latter outperform the former one but need not in all cases. Frequency-dependent reduced Müller matrix of the fabricated, fiber pigtailed, and packaged PMD compensator is measured using the integrated optical network analyzer from which the Jones matrix is calculated and hence the impulse response of the devices with polarization mode dispersion. Differential group delay profiles of this device are determined from the time domain impulse response by inverse scattering. This allows to identify, emulate, and compensate the effects of higher-order PMD that persists after compensation of first-order PMD.

Distributed PMD compensator performance can be pushed toward highest bit rates if they are implemented in mixed ferroelectric crystals like lithium–niobate–tantalate. A Ta content y in $LiNb_{1-y}Ta_yO_3$ of up to 0.5 is good to realize a PMD compensator for about 160 Gbit/s. Future scope would be to try this option.

5.4 Conclusion

This chapter has summarized these two application of the lithium niobate-based integrated optical circuits to optical communication. In this chapter, some of the fundamental and engineering problems encountered during this work, are described, in details. Moreover, the attempt has been made to systematically analyze and solve most of these problems. Future scope of this work is also presented.

Appendix A

Point Matching Method

Point Matching Method proposed by Marcuse [40], in 1989, is an effective method for solving the Laplace equation for the electric fields in inhomogeneous medium by employing a series expansion of the potential in terms of functions that are themselves the solution of Laplace equation for a homogeneous medium. The solution for stratified dielectric inhomogeneous medium is found by matching the solutions in the different homogenous layers with the help of boundary (continuity) conditions at a finite set of discrete points (Point Matching). This yields solution with a sufficient accuracy with series expansion method that does not involve any iteration.

A.1 Formulation

Figure A.1 shows the geometry of the problem. It consists of a x-cut, z-propagation $LiNbO_3$ crystal ($\varepsilon_x = 43$ and $\varepsilon_y = 28$) that extends from $x = -D$ to $x = -d$. From $x = -d$ to $x = 0$ there exists a buffer layer with $\varepsilon_2 = \varepsilon_{\rm b} = 3.8$ (typically SiO_2), and at $x = 0$, plane metal electrodes are deposited which are assumed to be infinitely thin and perfectly conducting. A medium with dielectric constant $\varepsilon_1 = \varepsilon_{\rm air} = 1$ (usually air), infinitely extends in $+x$ direction from $x = 0$ plane. The number of contacts are arbitrary, but they are assumed to be parallel and to extend infinitely in positive and negative z-direction.

The electrostatic field vector $\mathbf{E}$, generated by potentials applied to the electrodes, can be expressed in terms of potential function ψ as

$$\mathbf{E} = -\nabla\psi. \tag{A.1}$$

In each dielectric region, the potential must be a solution of Laplace equation, which in anisotropic medium assumes the form,

$$\frac{\varepsilon_x}{\varepsilon_y}\frac{\partial^2\psi}{\partial x^2} + \frac{\partial^2\psi}{\partial y^2} = 0. \tag{A.2}$$

In the isotropic regions 1 (air) and 2 (silicon dioxide buffer layer), we have $\varepsilon_x = \varepsilon_y = \varepsilon_j$ with $j = 1 \text{ or } 2$.

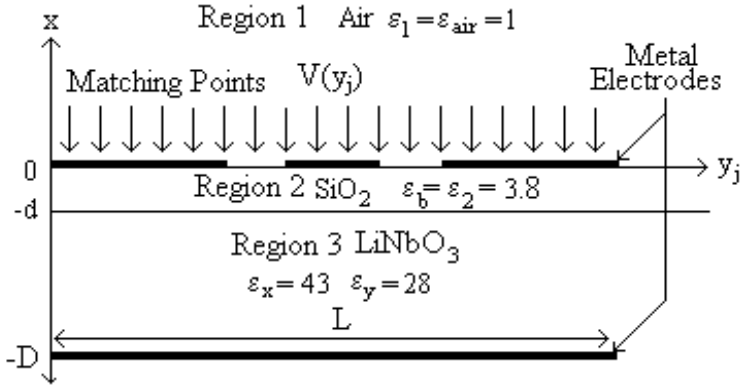

Figure A.1: Schematic of a typical electrode structure (CPW) on top of the layered dielectric substrate like $LiNbO_3$

The electric potentials applied to the metal electrodes imposes a definite y dependence on the potential function in the plane $x = 0$. This field variation could be described by the Fourier integral, but for numerical calculations the discrete series are easier to handle than integrals. Therefore, potential function is expanded in terms of cosine functions. The functions $\cos(\nu(\pi/L)y)$ forms a complete orthogonal set over the domain $0 < y < L$ for integral values of ν. The functions

$$\begin{aligned}
\phi_{1\nu} &= \exp(\pm\nu\kappa(\frac{\pi}{L})x)\cos(\nu(\frac{\pi}{L})y) \\
\phi_{2\nu} &= \cosh(\nu\kappa(\frac{\pi}{L})x)\cos(\nu(\frac{\pi}{L})y) \\
\phi_{3\nu} &= \sinh(\nu\kappa(\frac{\pi}{L})x)\cos(\nu(\frac{\pi}{L})y) \\
\phi_{4\nu} &= a + bx \quad \text{with} \\
\kappa &= \sqrt{\frac{\varepsilon_y}{\varepsilon_x}}
\end{aligned} \tag{A.3}$$

are the solutions of Laplace equation (A.2). Thus, one may express a potential function ψ in region 1 and 2 as follows:

$$\psi_1 = a_0 + \sum_{\nu=1}^{\infty} a_\nu e^{-\nu(\frac{\pi}{L})x}\cos(\nu(\frac{\pi}{L})y) \quad \text{for} \quad x \geq 0 \tag{A.4}$$

$$\psi_2 = b_0 + c_0 x + \sum_{\nu=1}^{\infty}[b_\nu e^{-\nu(\frac{\pi}{L})x} + c_\nu e^{\nu(\frac{\pi}{L})x}]\cos(\nu(\frac{\pi}{L})y) \quad \text{for} \quad 0 \geq x \geq -d \tag{A.5}$$

In region 3, the form of potential function depends on whether the region is infinitely extended or it is terminated by a ground plane. In Case of an infinitely extended medium,

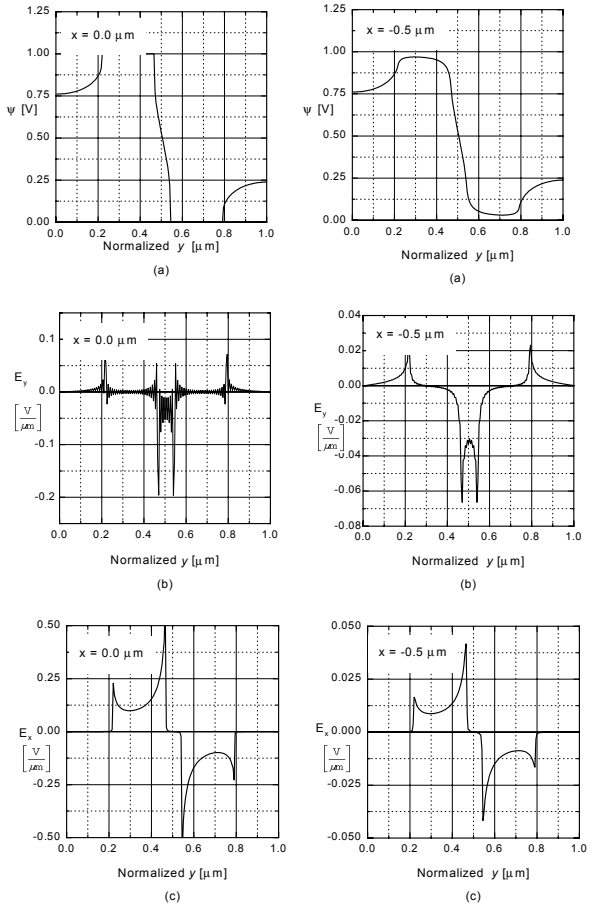

Figure A.2: Potential and electric fields of a two-electrode (CS) phase shifter computed using PMM in the plane of electrodes. $W_{\rm PS} = 50\ \mu$m, $G_{\rm PS} = 15\ \mu$m, $0.3\ \mu$m thick buffer with $\varepsilon_{\rm b} = 3.8$. (a) ψ (b) E_y (c) E_x

potential function is expressed as

$$\psi_3 = d_0 + \sum_{\nu=1}^{\infty} d_\nu e^{\nu\kappa(\frac{\pi}{L})(x+d)} \cos(\nu(\frac{\pi}{L})y) \quad \text{for} \quad x \leq -d. \tag{A.6}$$

The different forms of the series expansions in (A.4)–(A.6) are dictated by the boundary conditions. Since potential can not become infinite as $|x| \rightarrow \infty$, the linear term in x is absent from (A.4) and (A.6). For the same reason, only the exponential function whose value decreases with increasing value of $|x|$ is permitted in the series expansion of (A.4) and (A.6). Since the function $\cos(\nu(\pi/L)y)$ is an even function, the potential is automatically continued as an even function in the domain $-L < y < 0$. Moreover, it is periodic with a period $2L$ and implies that the solution behaves as though the structure were continued as a mirror images, imaged on the plane $y = 0$ and as if this extended system is periodically repeated with period $2L$.

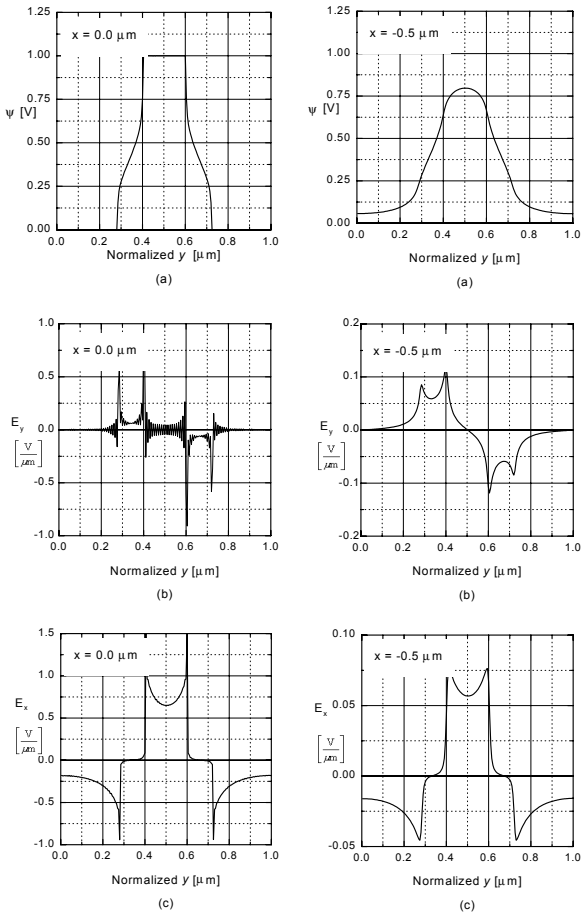

Figure A.3: Potential and electric fields of a coplanar-electrode (CPW) mode converter computed using PMM in the plane of electrodes. $W_{\mathrm{MC}} = 10\ \mu\mathrm{m}$, $G_{\mathrm{MC}} = 6\ \mu\mathrm{m}$, $0.3\ \mu\mathrm{m}$ thick buffer with $\varepsilon_{\mathrm{b}} = 3.8$. (a) ψ (b) E_y (c) E_x

A.2 Satisfying Boundary Conditions

At dielectric interfaces, the electric field must satisfy two boundary conditions, i.e. E_y and $\varepsilon_x E_x$ must pass continuously through the interface. The continuity of $E_y = -\partial\psi/\partial y$ everywhere in the plane $x = \mathrm{constant}$ is assured if ψ is continuous at the interface. Therefore, we may replace the condition for continuity of E_y by the requirement that ψ is continuous at the dielectric interfaces. Continuity of ψ i.e. ($\psi_2 = \psi_3$ at $x = -d$) and $\varepsilon_x \partial\psi/\partial x$ i.e. ($\varepsilon_2 \partial\psi_2/\partial x = \varepsilon_x \partial\psi_3/\partial x$ at $x = -d$) for all values of y requires that the coefficients of corresponding terms $\cos(\nu(\pi/L)y)$ of the expansions (A.5) and (A.6) are identical at plane $x = -d$. This leads to two simultaneous equations expressing b_ν and c_ν coefficients in terms of d_ν coefficients and leads to the following expressions for a structure without a

ground plane:

$$b_\nu = \frac{1}{2}(1-\kappa\frac{\varepsilon_x}{\varepsilon_b})e^{-\nu(\frac{\pi}{L})d}d_\nu \tag{A.7}$$

$$c_\nu = \frac{1}{2}(1+\kappa\frac{\varepsilon_x}{\varepsilon_b})e^{\nu(\frac{\pi}{L})d}d_\nu \tag{A.8}$$

$$\begin{aligned} b_0 &= d_0 \quad \text{and} \\ c_0 &= 0. \end{aligned} \tag{A.9}$$

The boundary condition in the plane of the (vanishingly thin) electrodes at $x = 0$ requires that x assumes same value on either side of the interface. This requirement ($\partial\psi_1/\partial y = \partial\psi_2/\partial y$ at x=0) immediately leads to the conditions

$$a_\nu = b_\nu + c_\nu \quad \text{for} \quad \nu = 1,\, 2,\, \cdots \tag{A.10}$$

$$a_0 = b_0. \tag{A.11}$$

On the electrode, we require instead that the potential function ψ should be equal to the applied voltages $V(y)$ ($\psi_1 = V(y)$ at x=0). We write the electrode potential as a function of y to indicate that its value is different on different electrodes even though $V(y)$ is constant on each individual electrodes. Therefore, one obtains (A.12) directly with the help of (A.10) and (A.11). But the continuity of $\varepsilon_x\partial\psi/\partial x$ now holds only in the gaps between the electrodes and not on the electrodes themselves i.e. to say ($\varepsilon_1\partial\psi_1/\partial x = \varepsilon_2\partial\psi_2/\partial x$ at $x = 0$) and therefore one obtains (A.13)

$$b_0 + \sum_{\nu=1}^{N-1}(b_\nu + c_\nu)\cos(\nu(\frac{\pi}{L})y) = V(y_j) \quad \text{on the electrodes} \tag{A.12}$$

$$\frac{L}{\pi}c_0 + \sum_{\nu=1}^{N-1}\nu[(\frac{\varepsilon_1}{\varepsilon_2}-1)b_\nu + (\frac{\varepsilon_1}{\varepsilon_2}+1)c_\nu]\cos(\nu(\frac{\pi}{L})y) = 0 \quad \text{in the gaps} \tag{A.13}$$

The label j is attached to y coordinate to indicate that the one satisfies the boundary conditions in the plane $x = 0$ only at a finite set of discrete points $y = y_j$. If there are N points in plane $x = 0$, there will be N terms in the series expansion in order to provide as many equations as there are unknown coefficients d_ν. It is necessary to calculate only d_ν coefficients since a_ν, b_ν, and c_ν all depend on d_ν. There are only N equations since (A.12) is used only on electrodes and (A.13) is used in the gaps. Therefore, one needs only to compute the elements of matrix $\mathbf{A_{j\nu}}$ in the system of equations given by (A.14).

$$\sum_{\nu=0}^{N-1}\mathbf{A_{j\nu}}d_\nu = \begin{bmatrix} V(y_j) & \text{on the electrodes} \\ 0 & \text{in the gaps} \end{bmatrix} \tag{A.14}$$

Matrix inversion of $\mathbf{A_{j\nu}}$ leads to the determination of the unknown coefficients d_ν via (A.15).

$$d_\nu = \sum_{\nu=0}^{N-1} (\mathbf{A^{-1}})_{\nu j} \begin{bmatrix} V(y_j) & \text{on the electrodes} \\ 0 & \text{in the gaps} \end{bmatrix} \tag{A.15}$$

The matrix inversion can, of course, be done numerically with the help of computer.

A.3 Computation

Depending upon the device geometry, the electrode structure is defined and a volt array $V(y_j)$ is assigned with appropriate voltages and $\mathbf{A_{j\nu}}$ matrix is generated with the help of (A.12 and A.13). The $Ax = B$ type of matrix equation is solved numerically with the help of computer by using lower upper (LU) triangularization and lower upper (LU) back substitution subroutines. The solution array replaces the volt array $V(y_j)$. Once the d_ν coefficients are known, then a_ν, b_ν, and c_ν can be calculated. After this the potentials ψ_1, ψ_2, and ψ_3 are generated with the help of (A.4)–(A.6). The electric field components E_x and E_y are calculated by analytically taking the first derivatives of ψ_1, ψ_2, and ψ_3 with respect to x and y. This completes the computation of electrostatic fields in air, buffer and lithium niobate regions of a layered dielectric structure.

Figure A.2 above shows the potential, electrostatic field E_y $\mathrm{V}/\mu\mathrm{m}$, and electrostatic field E_x $\mathrm{V}/\mu\mathrm{m}$ calculated for the realized phase shifter ($V_\pi = 40$ V) on X-cut, Z-propagation $LiNbO_3$, where y-directed field E_y is used for the phase modulation.

Figure A.3 above shows the potential, electrostatic field E_y $\mathrm{V}/\mu\mathrm{m}$, and electrostatic field E_x $\mathrm{V}/\mu\mathrm{m}$ calculated for the realized TE-TM mode converter ($V_{\mathrm{MC}} = 10$ V) on X-cut, Z-propagation $LiNbO_3$, where x-directed field E_x is used for the mode conversion.

Appendix B

Generation of Optical Fields

Optical fields within the titanium (Ti) in-diffused optical waveguides in X-cut, Z-propagation $LiNbO_3$ are well approximated by Gaussian and Hermite-Gaussian functions in width and depth directions, respectively [72]. Electric field $E_{\rm o}(x,\, y)$ becomes

$$E_{\rm o}(x,\, y) = (\frac{x}{w_{\rm x}})e^{\frac{-x^2}{w_{\rm x}^2}} e^{\frac{-y^2}{w_{\rm y}^2}} \tag{B.1}$$

where $w_{\rm y}$ and $w_{\rm x}$ are the $(1/e)$ widths of the electric field profiles in width and depth directions, respectively. In the computation of field overlap integral, Γ, as defined in [39], one needs to use the normalized intensity $E_{\rm o}^2(x, y)$. It is possible to measure only the Full Width Half Maximum (FWHM) of the intensity profiles $w_{\rm y_{fwhm}}$ and $w_{\rm x_{fwhm}}$ along the width and depth of the Ti in-diffused waveguides in $LiNbO_3$ experimentally. One needs to fit $w_{\rm x}$ and $w_{\rm y}$ to experimentally measured values of $w_{\rm x_{fwhm}}$ and $w_{\rm y_{fwhm}}$ of the measured intensity profiles.

For Gaussian approximation, one can write $E_{\rm o_y}^2 = e^{-2(y_{1/2}^2/w_{\rm y}^2)} = 1/2$ for the half of the maximum intensity and $y_{1/2} = w_{\rm y}\sqrt{\ln 2/2}$. But $w_{\rm y_{fwhm}} = 2y_{1/2}$ and therefore, $w_{\rm y} = w_{\rm y_{fwhm}}/\sqrt{2\ln 2}$.

For Hermite-Gaussian approximation, the situation is little bit different, one can write $E_{\rm o_x}^2 = (x^2/w_{\rm x}^2)e^{-2(x^2/w_{\rm x}^2)}$ for the intensity as before. This function will have a maximum value at $x = (1/2)e^{-1}$. For half of the maximum value, $E_{\rm o_x}^2 = (x_{1/2}^2/w_{\rm x}^2)e^{-2(x_{1/2}^2/w_{\rm x}^2)} = (1/4)e^{-1}$. There are two solutions: $x_1 = 1.1572w_{\rm x}$ and $x_2 = 0.34056w_{\rm x}$, if one solves this for $x_{1/2}$. For $w_{\rm x_{fwhm}} = x_1 - x_2$ and $w_{\rm x} = w_{\rm x_{fwhm}}/0.81667$.

It is necessary to adjust the peak of the optical intensity at right position along the width and depth of the Ti in-diffused optical waveguide. Therefore, one can introduce the normalization constants $C_{\rm x}$ and $C_{\rm y}$ as well as the p and q variables for the optical intensity as

$$E_{\rm o}^2(x,\, y) = C_{\rm x}^2(\frac{x-q}{w_{\rm x}})^2 e^{-2(\frac{x-q}{w_{\rm x}})^2} C_{\rm y}^2 e^{-2(\frac{y-p}{w_{\rm y}})^2}. \tag{B.2}$$

The p value shifts the peak position of $E_{\rm o}^2(x,\, y)$ along width of the waveguide while the q value shifts the peak position of $E_{\rm o}^2(x,\, y)$ along the depth of the waveguide.

It is essential to take into account the boundary conditions imposed on the $E_{\mathrm{o_x}}$ at the interface between the lithium niobate and buffer layer, which is usually, a silicon dioxide layer. The reason because optical index of lithium niobate is 2.2 and that of silicon dioxide is 1.46. Due to this large discontinuity in the optical refractive indices of these two materials, the optical field intensity decays exponentially in the buffer layer regardless of the thickness of the buffer layer. In the buffer layer, the optical field $E_{\mathrm{o_x}}$ obeys the equation

$$\frac{\partial E_{\mathrm{o_x}}}{\partial x} = \gamma E_{\mathrm{o_x}} \tag{B.3}$$

where $\gamma = k\sqrt{N_{\mathrm{eff}}^2 - N_{\mathrm{b}}^2}$ and $k = 2\pi/\lambda$.

Boundary conditions imposed on $E_{\mathrm{o_x}}$, for the TE-polarized optical field are

$$E_{\mathrm{o_{x_b}}} = E_{\mathrm{o_{x_{LN}}}} \tag{B.4-a}$$

$$\frac{\partial E_{\mathrm{o_{x_b}}}}{\partial x} = \frac{\partial E_{\mathrm{o_{x_{LN}}}}}{\partial x} \tag{B.4-b}$$

where $E_{\mathrm{o_{x_b}}}$ and $E_{\mathrm{o_{x_{LN}}}}$ are the optical fields in the buffer layer and in the $LiNbO_3$, respectively. If one solves (B.3) then $E_{\mathrm{o_{x_b}}} = e^{-\gamma x}$ for the fields in the buffer region. Since, one needs to use the normalized intensity, a normalization constant C_{b} is introduced in the solution of (B.3) and $E_{\mathrm{o_{x_b}}}^2 = C_{\mathrm{b}}^2 e^{-2\gamma x}$. One has to apply the second boundary condition (B.4-b) at $y = 0$, to get the relation between the two normalization constants C_{x} and C_{b} as

$$C_{\mathrm{b}} = \frac{-C_x}{\gamma w_x} \tag{B.5}$$

To find the value of q, one has to apply the boundary condition (B.4-a) at $x = 0$ to get the equation

$$q e^{\frac{-q^2}{w_{\mathrm{x}}^2}} - \frac{1}{\gamma} = 0. \tag{B.6}$$

Solving for q, one gets

$$\begin{aligned} q =& \frac{1}{\gamma e^{(\frac{1}{2}\mathrm{Lambert}[w(\frac{-2}{\gamma^2 w_{\mathrm{x}}^2})])}} \\ \mathrm{Lambert}\, w(x) =& x - x^2 + \frac{3}{2}x^3 - \frac{8}{3}x^4 + \frac{125}{24}x^5 \text{ and } x = (\frac{-2}{\gamma^2 w_{\mathrm{x}}^2}) \end{aligned} \tag{B.7}$$

Similarly the boundary conditions imposed on $E_{\mathrm{o_x}}$ for the TM-polarized optical mode are

$$\varepsilon_{\mathrm{b}} E_{\mathrm{o_{x_b}}} = \varepsilon_{\mathrm{LN}} E_{\mathrm{o_{x_{LN}}}} \tag{B.8-a}$$

$$\varepsilon_{\mathrm{b}} \frac{\partial E_{\mathrm{o_{x_b}}}}{\partial y} = \varepsilon_{\mathrm{LN}} \frac{\partial E_{\mathrm{o_{x_{LN}}}}}{\partial x} \tag{B.8-b}$$

where ε_{b} and ε_{x} are the dielectric constants of the buffer and the X-cut lithium niobate respectively. These conditions modifies the equation (B.7) to

$$\frac{\varepsilon_{\mathrm{x}}}{\varepsilon_{\mathrm{b}}} q e^{\frac{-q^2}{w_{\mathrm{x}}^2}} - \frac{1}{\gamma} = 0 \tag{B.9}$$

where $\varepsilon_{\mathrm{b}} = N_{\mathrm{b}}^2$ and $\varepsilon_{\mathrm{x}} = N_{\mathrm{o}}^2$. Solving for q, one gets

$$\begin{gathered} q = \frac{N_{\mathrm{b}}^2}{N_{\mathrm{o}}^2 \gamma e^{(\frac{1}{2}\mathrm{Lambert}[w(\frac{-2N_{\mathrm{b}}^4}{N_{\mathrm{o}}^4 \gamma^2 w_{\mathrm{x}}^2})])}} \\ \mathrm{Lambert}\, w(x) = x - x^2 + \frac{3}{2}x^3 - \frac{8}{3}x^4 + \frac{125}{24}x^5 \,\text{and}\, x = (\frac{-2N_{\mathrm{b}}^4}{N_{\mathrm{o}}^4 \gamma^2 w_{\mathrm{x}}^2}). \end{gathered} \tag{B.10}$$

For normalization of the Gaussian profile, one uses the condition

$$\begin{gathered} C_{\mathrm{y}}^2 \int_{-\infty}^{\infty} |E_{\mathrm{o_y}}|^2 dy = 1 \\ C_{\mathrm{y}} = \sqrt{\frac{1}{w_{\mathrm{y}}} \sqrt{\frac{2}{\pi}}} \end{gathered} \tag{B.11}$$

For normalization of the Hermite-Gaussian profile, one uses the condition

$$\begin{gathered} C_{\mathrm{x}}^2 \int_{-\infty}^{0} |E_{\mathrm{o_x}}|^2 dx + C_{\mathrm{b}}^2 \int_{0}^{\infty} |E_{\mathrm{o_x}}|^2 dx = 1. \\ C_{\mathrm{x}} = \frac{1}{\sqrt{\frac{1}{2\gamma^3 w_{\mathrm{x}}^2} + \frac{1}{16} w_{\mathrm{x}} \sqrt{2\pi}}} \\ C_{\mathrm{b}} = -\frac{C_{\mathrm{x}}}{\gamma w_{\mathrm{x}}} \end{gathered} \tag{B.12}$$

These normalization constants C_{x}, C_{b}, and C_{y} are used to generate the normalized polarization dependent optical intensity profiles in the buffer region and lithium niobate region, respectively.

$$\begin{aligned} E_{\mathrm{o}}^2(x,\, y) &= C_{\mathrm{b}}^2 e^{-2\gamma(d+x)} C_{\mathrm{y}}^2 e^{-2(\frac{y-p}{w_{\mathrm{y}}})^2} \quad \text{buffer region} \\ E_{\mathrm{o}}^2(x,\, y) &= C_{\mathrm{x}}^2 (\frac{d+x-q}{w_{\mathrm{x}}})^2 e^{-2(\frac{d+x-q}{w_{\mathrm{x}}})^2} C_{\mathrm{y}}^2 e^{-2(\frac{y-p}{w_{\mathrm{y}}})^2} \ \mathrm{LiNbO_3\,region} \end{aligned} \tag{B.13}$$

Appendix C

Derivation of Coupled Differential Equations for FBG

C.1 Maxwell Equations

Light is an electromagnetic wave phenomenon. Its electric and magnetic field is represented by the four electromagnetic field vectors that are functions of position r [m] and time t [s]. The four vectors — electric field $\mathbf{E}$ [V/m], magnetic field $\mathbf{H}$ [A/m], electric flux density $\mathbf{D}$ $[\mathrm{C/m^2}]$, and magnetic flux density $\mathbf{B}$ $[\mathrm{Wb/m^2}]$ governs the well known Maxwell equations:

$$\begin{aligned} \nabla \times \mathbf{E} &= -\frac{\partial \mathbf{B}}{\partial t} \\ \nabla \times \mathbf{H} &= J + \frac{\partial \mathbf{D}}{\partial t} \end{aligned} \tag{C.1}$$

Here $\mathbf{J}$ $[\mathrm{A/m^2}]$ is the current density and $\nabla = (\partial/\partial x,\, \partial/\partial y,\, \partial/\partial z)$ is the del operator. The following continuity equation governs the current density $\mathbf{J}$ and the charge density ρ $[\mathrm{C/m^3}]$:

$$\nabla \cdot \mathbf{J} = -\frac{\partial \rho}{\partial t}. \tag{C.2}$$

Use of (C:1) and (C:2) and the vector identity $\nabla \cdot \nabla \times \mathbf{a} = 0$ one gets

$$\begin{aligned} \nabla \cdot \mathbf{B} &= 0 \\ \nabla \cdot \mathbf{D} &= \rho \end{aligned}. \tag{C.3}$$

Fields are assume to have a periodic time dependence and are written as

$$\mathbf{E}(r,\, t) = \mathrm{Re}[\mathbf{E}(r) e^{\jmath(\omega t - kz)}], \text{ etc.} \tag{C.4}$$

C.2 Constitutive Relations

If the polarization generated in the light transmitting medium is $\mathbf{P}$ $[\mathrm{C/m^2}]$ and the magnetization is $\mathbf{M}$ [A/m], the electric flux density $\mathbf{D}$ and magnetic flux density $\mathbf{B}$ are, respectively,

$$\begin{aligned} \mathbf{D} &= \varepsilon_0 \mathbf{E} + \mathbf{P} \\ \mathbf{B} &= \mu_0 (\mathbf{H} + \mathbf{M}) \end{aligned}. \tag{C.5}$$

Here ε_0 [F/m] and μ_0 [H/m] are the permittivity of vacuum and the permeability of free space, respectively and their values are as follows.

$$\begin{aligned} \varepsilon_0 &= 8.8541878 \times 10^{-12} \quad [\mathrm{F/m}] \\ \mu_0 &= 4\pi \times 10^{-7} \quad [\mathrm{H/m}] \end{aligned} \tag{C.6}$$

If the medium is isotropic, linear, and non-dispersive, the polarization $\mathbf{P}$ and the magnetization $\mathbf{M}$ are obtained as follows:

$$\begin{aligned} \mathbf{P} &= \varepsilon_0 \chi_\mathrm{e} \mathbf{E} \\ \mathbf{M} &= \mu_0 \chi_\mathrm{m} \mathbf{H}. \end{aligned} \tag{C.7}$$

Here χ_e and χ_m are the electric susceptibility and the magnetic susceptibility respectively. If equations (C:7) are substituted into equations (C:5), respectively, then we get the relative permittivity ε_r and the relative permeability μ_r as follows.

$$\begin{aligned} \varepsilon_\mathrm{r} &= 1 + \chi_\mathrm{e} \\ \mu_\mathrm{r} &= 1 + \chi_\mathrm{m} \end{aligned}. \tag{C.8}$$

Therefore the permittivity ε and permeability μ are

$$\begin{aligned} \varepsilon &= \varepsilon_0 \varepsilon_\mathrm{r} \\ \mu &= \mu_0 \mu_\mathrm{r}. \end{aligned} \tag{C.9}$$

The constitutive relations are as follows:

$$\begin{aligned} \mathbf{D} &= \varepsilon \mathbf{E} \quad \text{and} \\ \mathbf{B} &= \mu \mathbf{H} \end{aligned} \quad . \tag{C.10}$$

The refractive index n can be obtained from

$$n = \sqrt{\varepsilon_\mathrm{r} \mu_\mathrm{r}}. \tag{C.11}$$

But for most optical materials, (say glass), $\mu = \mu_0$ and $\mu_\mathrm{r} = 1$, the refractive index n simply becomes

$$n = \sqrt{\varepsilon_\mathrm{r}}. \tag{C.12}$$

C.3 Wave Equation

For deriving the vector wave equation for the electric field $\mathbf{E}$, for an isotropic lossless medium with no wave sources ($\mathbf{J} = 0$ and $\rho = 0$) with uniform permeability μ_0, one has to take the curl of the above Maxwell equation (C:1) and make use of (C:10) to get

$$\begin{aligned} \nabla \times \nabla \times \mathbf{E} = \nabla \times -\frac{\partial \mathbf{B}}{\partial t} = -\frac{\partial}{\partial t} \nabla \times \mathbf{B} = -\mu_0 \frac{\partial}{\partial t} \nabla \times \mathbf{H} \\ = -\mu_0 \frac{\partial^2 \mathbf{D}}{\partial t^2} = -\mu_0 \varepsilon \frac{\partial^2 \mathbf{E}}{\partial t^2} \end{aligned} \tag{C.13}$$

The equation (C:3) for the source free medium becomes ($\nabla \cdot \mathbf{D} = 0$) and making use of the following vector identities

$$\begin{aligned} \nabla \cdot (a\mathbf{b}) &= a(\nabla \cdot \mathbf{b}) + \mathbf{b} \cdot (\nabla a) \\ \nabla \times \nabla \times \mathbf{a} &= -\nabla^2 \mathbf{a} + \nabla(\nabla \cdot \mathbf{a}) \end{aligned} \tag{C.14}$$

one gets the wave equation

$$\nabla^2 \mathbf{E} + \nabla(\mathbf{E} \cdot \nabla \ln \varepsilon) = \mu_0 \varepsilon \frac{\partial^2 \mathbf{E}}{\partial t^2} \quad \text{and} \quad \varepsilon = \varepsilon_0 \varepsilon_r. \tag{C.15}$$

C.4 Coupled Differential Equations for FBG

One can note that the quantities $\varepsilon_t = \varepsilon_r(x,\, y)$ and hence the transverse components $\mathbf{E}_t = (\mathbf{E}_x,\, \mathbf{E}_y)$ are independent of z.

$$\varepsilon_t = \varepsilon_r(x,\, y) = \begin{array}{ll} \varepsilon_{r,\,\text{core}} & \text{for} \quad x^2 + y^2 < R^2 \\ \varepsilon_{r,\,\text{clad}} & \text{for} \quad x^2 + y^2 \geq R^2 \end{array}, \tag{C.16}$$

where R is the core radius of the single mode fiber. Therefore, for the fiber Bragg grating, the above vector wave equation (C:15) with $\mathbf{E}(z,\, t)$ and $\varepsilon_r = \varepsilon_r(z)$ simplifies to

$$\frac{\partial^2}{\partial z^2} \mathbf{E}(z,\, t) = \mu_0 \varepsilon \frac{\partial^2}{\partial t^2} \mathbf{E}(z,\, t) \tag{C.17}$$

For Bragg grating $\varepsilon_r(z) = n^2(z)$ from where

$$\begin{aligned} n(z) &= n_0 + \frac{1}{2} \Delta n_{pp}(z) \cos(\frac{2\pi}{\Lambda} z + \phi_k(z)) \\ &= n_0 + \text{Re}[\frac{1}{2} \Delta n_{pp}(z) e^{\jmath(k_g z + \phi_k(z))}] \quad \text{and} \quad k_g = \frac{2\pi}{\Lambda} \\ &= n_0 + \text{Re}[\Delta n_k(z) e^{\jmath k_g z}] \quad \text{and} \quad \Delta n_k(z) = \frac{1}{2} \Delta n_{pp}(z) e^{\jmath \phi_k(z)} \end{aligned} \quad . \tag{C.18}$$

Peak to peak refractive index modulation amplitude satisfies the condition

$$\Delta n_{pp} << n_{\text{eff}}. \tag{C.19}$$

Using the nomenclature [54], electric field of the forward, $\mathbf{E}_{\mathrm{f}}(z,\,t)$ and backward, $\mathbf{E}_{\mathrm{b}}(z,\,t)$ propagating waves in the Bragg grating are written as

$$\begin{aligned}\mathbf{E}_{\mathrm{f}}(z,\,t) &= \mathrm{Re}[\mathbf{D}(z)e^{\jmath(\omega t-kz)}] = \mathrm{Re}[\mathbf{d}(z)e^{\jmath(\omega t-kz)}]\\ \mathbf{E}_{\mathrm{b}}(z,\,t) &= \mathrm{Re}[\mathbf{U}(z)e^{\jmath(\omega t+kz)}] = \mathrm{Re}[\mathbf{u}(z)e^{\jmath(\omega t+kz)}]\end{aligned} \quad \text{and} \quad k=\frac{n_0}{c_0}\omega, \tag{C.20}$$

where n_0 is the effective refractive index of the grating and c_0 is the free space velocity of light. Taking the second derivatives of (C:20) with respect to time t, one gets

$$\begin{aligned}\frac{\partial^2}{\partial t^2}\mathbf{E}_{\mathrm{f}}(z,\,t) &= \mathrm{Re}[-\omega^2\mathbf{d}(z)e^{\jmath(\omega t-kz)}]\\ \frac{\partial^2}{\partial t^2}\mathbf{E}_{\mathrm{b}}(z,\,t) &= \mathrm{Re}[-\omega^2\mathbf{u}(z)e^{\jmath(\omega t+kz)}]\end{aligned} \tag{C.21}$$

Similarly by taking the second derivative of (C:20) with respect to one dimensional space coordinate z, one gets

$$\begin{aligned}\frac{\partial^2}{\partial z^2}\mathbf{E}_{\mathrm{f}}(z,\,t) &= \mathrm{Re}[(-k^2\mathbf{d}(z)-\jmath 2k\frac{\partial}{\partial z}\mathbf{d}(z)+\frac{\partial^2}{\partial z^2}\mathbf{d}(z))e^{\jmath(\omega t-kz)}]\\ \frac{\partial^2}{\partial z^2}\mathbf{E}_{\mathrm{b}}(z,\,t) &= \mathrm{Re}[(-k^2\mathbf{u}(z)+\jmath 2k\frac{\partial}{\partial z}\mathbf{u}(z)+\frac{\partial^2}{\partial z^2}\mathbf{u}(z))e^{\jmath(\omega t+kz)}]\end{aligned}. \tag{C.22}$$

Term with second order derivative of fields with respect to one dimensional space coordinate z are so small that these terms can be neglected to give

$$\begin{aligned}\frac{\partial^2}{\partial z^2}\mathbf{E}_{\mathrm{f}}(z,\,t) &= \mathrm{Re}[(-k^2\mathbf{d}(z)-\jmath 2k\frac{\partial}{\partial z}\mathbf{d}(z)))e^{\jmath(\omega t-kz)}]\\ \frac{\partial^2}{\partial z^2}\mathbf{E}_{\mathrm{b}}(z,\,t) &= \mathrm{Re}[(-k^2\mathbf{u}(z)+\jmath 2k\frac{\partial}{\partial z}\mathbf{u}(z))e^{\jmath(\omega t+kz)}]\end{aligned}. \tag{C.23}$$

Total field $\mathbf{E}$ is the superposition of the forward $\mathbf{E}_{\mathrm{f}}(z,\,t)$ and backward $\mathbf{E}_{\mathrm{b}}(z,\,t)$ propagating fields in the wave equation (C:17).

$$\frac{\partial^2}{\partial z^2}(\mathbf{E}_{\mathrm{f}}(z,\,t)+\mathbf{E}_{\mathrm{b}}(z,\,t)) = \frac{n(z)^2}{c_0^2}\frac{\partial^2}{\partial t^2}(\mathbf{E}_{\mathrm{f}}(z,\,t)+\mathbf{E}_{\mathrm{b}}(z,\,t)) \tag{C.24}$$

Substituting for the second derivatives of $\mathbf{E}_{\mathrm{f}}(z,\,t)$ and $\mathbf{E}_{\mathrm{b}}(z,\,t)$ with respect to t and z from (C:21) and (C:22) into (C:24) yields

$$\begin{aligned}&\mathrm{Re}[(-k^2\mathbf{d}(z)-\jmath 2k\frac{\partial}{\partial z}\mathbf{d}(z)))e^{\jmath(\omega t-kz)}]+\mathrm{Re}[(-k^2\mathbf{u}(z)+\jmath 2k\frac{\partial}{\partial z}\mathbf{u}(z))e^{\jmath(\omega t+kz)}] =\\ &\frac{1}{c_0^2}(n_0^2+2n_0\mathrm{Re}[\Delta n_k(z)e^{\jmath(k_g z)}])\mathrm{Re}[-\omega^2\mathbf{d}(z)e^{\jmath(\omega t-kz)}]+\mathrm{Re}[-\omega^2\mathbf{u}(z)e^{\jmath(\omega t+kz)}].\end{aligned} \tag{C.25}$$

Simplification of (C:25) using (C:20) gives

$$\begin{aligned}&-\jmath 2k\frac{\partial}{\partial z}\mathbf{d}(z)e^{-\jmath kz}+\jmath 2k\frac{\partial}{\partial z}\mathbf{u}(z)e^{\jmath kz} =\\ &\frac{-\omega^2}{c_0^2}2n_0\mathrm{Re}[\Delta n_k(z)e^{\jmath(k_g z)}](\mathbf{d}(z)e^{-\jmath kz}+\mathbf{u}(z)e^{\jmath kz}).\end{aligned} \tag{C.26}$$

Grating constant k_g as defined in (C:27) is approximately equal to twice the propagation constant k of the wave ($k = 2\pi/\lambda$).

$$k_g \approx 2k \tag{C.27}$$

Equation (C:26) contains to first order differential equations:

$$\begin{aligned} -\jmath 2k\frac{\partial}{\partial z}e^{-\jmath kz}\mathbf{d}(z) &= -\frac{\omega^2}{c_0^2}n_0 e^{\jmath kz}[\Delta n_k^*(z)e^{-\jmath k_g z}]\mathbf{u}(z) \\ \jmath 2k\frac{\partial}{\partial z}e^{\jmath kz}\mathbf{u}(z) &= -\frac{\omega^2}{c_0^2}n_0 e^{-\jmath kz}[\Delta n_k(z)e^{\jmath k_g z}]\mathbf{d}(z) \end{aligned} \tag{C.28}$$

Simplification of (C:28) delivers

$$\begin{aligned} \frac{\partial}{\partial z}\mathbf{d}(z) &= -\jmath\frac{\omega}{2c_0}[\Delta n_k^*(z)e^{\jmath(2k-k_g)z}]\mathbf{u}(z) \\ \frac{\partial}{\partial z}\mathbf{u}(z) &= \jmath\frac{\omega}{2c_0}[\Delta n_k(z)e^{-\jmath(2k-k_g)z}]\mathbf{d}(z) \end{aligned}. \tag{C.29}$$

The coupling coefficient

$$\boldsymbol{\kappa}(z) = \jmath\frac{\omega}{2c_0}\Delta n_k(z) \tag{C.30}$$

modifies the simplified expressions for the coupled differential equations for the fiber Bragg grating as

$$\begin{aligned} \frac{\partial}{\partial z}\mathbf{d}(z) &= \boldsymbol{\kappa}^*(z)e^{\jmath(2k-k_g)z}\mathbf{u}(z) \\ \frac{\partial}{\partial z}\mathbf{u}(z) &= \boldsymbol{\kappa}(z)e^{-\jmath(2k-k_g)z}\mathbf{d}(z) \end{aligned}. \tag{C.31}$$

The forward and backward propagating waves are also the functions of time t. At the Bragg wavelength, $\omega = \omega_0$ and the propagation constant $k = k_0$,

$$\begin{aligned} \mathbf{E}_{\mathrm{f}}(z,\,t) &= \mathrm{Re}[\widetilde{\mathbf{d}}(z,\,t)e^{\jmath(\omega_0 t - k_0 z)}] \\ \mathbf{E}_{\mathrm{b}}(z,\,t) &= \mathrm{Re}[\widetilde{\mathbf{u}}(z,\,t)e^{\jmath(\omega_0 t + k_0 z)}] \end{aligned} \tag{C.32}$$

Subtracting (C:20) from (C:32) respectively,

$$\begin{aligned} \widetilde{\mathbf{d}}(z,\,t)e^{\jmath[(\omega_0-\omega)t-(k_0-k)z]} &= \widetilde{\mathbf{d}}(z,\,t)e^{\jmath[(\omega_0-\omega)(t-\frac{n_0}{c_0}z)]} = \mathbf{d}(z,\,t) \\ \widetilde{\mathbf{u}}(z,\,t)e^{\jmath[(\omega_0-\omega)t+(k_0-k)z]} &= \widetilde{\mathbf{u}}(z,\,t)e^{\jmath[(\omega_0-\omega)(t+\frac{n_0}{c_0}z)]} = \mathbf{u}(z,\,t) \end{aligned} \tag{C.33}$$

Differentiating (C:33) with respect to 1-D space coordinate z,

$$\begin{aligned} \frac{\partial}{\partial z}\left(\widetilde{\mathbf{d}}(z,\,t)e^{\jmath[(\omega_0-\omega)(t-\frac{n_0}{c_0}z)]}\right) &= \frac{\partial}{\partial z}\mathbf{d}(z) \\ \frac{\partial}{\partial z}\left(\widetilde{\mathbf{u}}(z,\,t)e^{\jmath[(\omega_0-\omega)(t+\frac{n_0}{c_0}z)]}\right) &= \frac{\partial}{\partial z}\mathbf{u}(z) \end{aligned} \tag{C.34}$$

Simplification of (C:34) gives

$$\begin{aligned} e^{\jmath[(\omega_0-\omega)(t-\frac{n_0}{c_0}z)]}\left(\frac{\partial}{\partial z}\widetilde{\mathbf{d}}(z,\,t)+\frac{n_0}{c_0}\jmath(\omega-\omega_0)\widetilde{\mathbf{d}}(z,\,t)\right)&=\frac{\partial}{\partial z}\mathbf{d}(z)\\ e^{\jmath[(\omega_0-\omega)(t+\frac{n_0}{c_0}z)]}\left(\frac{\partial}{\partial z}\widetilde{\mathbf{u}}(z,\,t)-\frac{n_0}{c_0}\jmath(\omega-\omega_0)\widetilde{\mathbf{u}}(z,\,t)\right)&=\frac{\partial}{\partial z}\mathbf{u}(z)\end{aligned} \tag{C.35}$$

The terms containing $\jmath(\omega-\omega_0)\widetilde{\mathbf{d}}(z,\,t)$ and $\jmath(\omega-\omega_0)\widetilde{\mathbf{u}}(z,\,t)$ are obtained if one differentiates (C:33) with respect to time t.

$$\begin{aligned}\jmath(\omega-\omega_0)\widetilde{\mathbf{d}}(z,\,t)&=\frac{\partial}{\partial t}\widetilde{\mathbf{d}}(z,\,t)\\ \jmath(\omega-\omega_0)\widetilde{\mathbf{u}}(z,\,t)&=\frac{\partial}{\partial t}\widetilde{\mathbf{u}}(z,\,t)\end{aligned} \tag{C.36}$$

Therefore (C:35) becomes

$$\begin{aligned} e^{\jmath[(\omega_0-\omega)(t-\frac{n_0}{c_0}z)]}[\frac{\partial}{\partial z}\widetilde{\mathbf{d}}(z,\,t)+\frac{n_0}{c_0}\frac{\partial}{\partial t}\widetilde{\mathbf{d}}(z,\,t)]&=\frac{\partial}{\partial z}\mathbf{d}(z)\\ e^{\jmath[(\omega_0-\omega)(t+\frac{n_0}{c_0}z)]}[\frac{\partial}{\partial z}\widetilde{\mathbf{u}}(z,\,t)-\frac{n_0}{c_0}\frac{\partial}{\partial t}\widetilde{\mathbf{u}}(z,\,t)]&=\frac{\partial}{\partial z}\mathbf{u}(z)\end{aligned}. \tag{C.37}$$

The equations (C:35) and (C:37) into (C:31) gives

$$\begin{aligned} &e^{\jmath[(\omega_0-\omega)(t-\frac{n_0}{c_0}z)]}[\tfrac{\partial}{\partial z}+\tfrac{n_0}{c_0}\tfrac{\partial}{\partial t}]\widetilde{\mathbf{d}}(z,\,t)=\\ &\boldsymbol{\kappa}(z)^*e^{\jmath(2k-k_g)z}\widetilde{\mathbf{u}}(z,\,t)e^{\jmath[(\omega_0-\omega)(t+\frac{n_0}{c_0}z)]}\\ &e^{\jmath[(\omega_0-\omega)(t+\frac{n_0}{c_0}z)]}[\tfrac{\partial}{\partial z}-\tfrac{n_0}{c_0}\tfrac{\partial}{\partial t}]\widetilde{\mathbf{u}}(z,\,t)=\\ &\boldsymbol{\kappa}(z)e^{-\jmath(2k-k_g)z}\widetilde{\mathbf{d}}(z,\,t)e^{\jmath[(\omega_0-\omega)(t-\frac{n_0}{c_0}z)]}\end{aligned}. \tag{C.38}$$

Simplification of (C:38) yields the equations (3.12) used in chapter 3.

$$\begin{aligned}(\frac{\partial}{\partial z}+\frac{n_0}{c_0}\frac{\partial}{\partial t})\widetilde{\mathbf{d}}(z,\,t)&=\boldsymbol{\kappa}^*(z)\widetilde{\mathbf{u}}(z,\,t)\\ (\frac{\partial}{\partial z}-\frac{n_0}{c_0}\frac{\partial}{\partial t})\widetilde{\mathbf{u}}(z,\,t)&=\boldsymbol{\kappa}(z)\widetilde{\mathbf{d}}(z,\,t)\end{aligned}. \tag{C.39}$$

Appendix D

Derivation of Discrete Equations for FBG

D.1 S-Matrix Characterization of Optical Components

At network level, a component is considered as a "black box", isolated from rest of the world except for a few designated ports that are accessible for external connection. For network analysis purpose, a component is completely characterized by the relations between the signals or fields available at these ports. This type of component characterization is called port characterization. In the frequency domain, the relations between the various fields at the ports of a linear, time-independent optical component such as a FBG are essentially a set of linear equations. These linear equations are algebraically represented by a matrix. For the characterization of active component, an extra vector describing a signal generator may be needed.

The $\mathbf{S}$-matrix characterization is well suited as a port characterization of optical components. However, due to the fact that in optical waveguides there are two guided modes, each physical port of an optical component is actually equivalent to two strictly single mode ports. An optical component could be treated in exactly same fashion as a microwave component by separating logically two virtual single mode ports that corresponds to each one of the physical ports. This logical separation is a problematic and confusing and therefore, it is better to regard each port both physically and logically as a single entity. This approach is more promising, but there is a price to it: the scattering parameters become 2x2 matrices and the $\mathbf{S}$-matrix becomes a "super matrix", i.e. a matrix whose elements are 2x2 matrices instead of regular numbers. This is most fundamental difference between the optical $\mathbf{S}$-matrix as will be presented here and the corresponding $\mathbf{S}$-matrix used in microwave theory.

If the optical component is linear and time-independent, then in the frequency domain, the input and output Jones vectors $\mathbf{A}'$ and $\mathbf{A}$ are related by a set of linear equations

$$\mathbf{A}' = \mathbf{S}\mathbf{A} + \mathbf{C}, \tag{D.1}$$

where $\mathbf{S}$ is a complex 2x2 matrix and $\mathbf{C}$ is a complex 2 element vector, both independent

of $\mathbf{A}$. The matrix $\mathbf{S}$ is called the Scattering-matrix (S-matrix) of the component. $\mathbf{S}$ may be regarded as a Jones matrix of the component. The Jones vector $\mathbf{C}$ may represent optical field generators that may be present in the component. It has a significant value only in the active components. In passive components such as FBG, $\mathbf{C}$ is normally neglected, since at the frequencies that are currently used in the optical network applications, the blackbody radiation at room temperature is negligible.

Some important properties of $\mathbf{S}$ matrices are derived from the energy conservation considerations. The input and output powers P_{in} and P_{out} are give by

$$P_{\text{in}} = |\mathbf{A}|^2 P_0 \quad \text{and} \quad P_{\text{out}} = |\mathbf{A}'|^2 P_0 = |\mathbf{SA} + \mathbf{C}|^2 P_0 \tag{D.2}$$

where P_0 is a unit power. For passive component, $\mathbf{C} = 0$, and energy conservation implies that $P_{\text{in}} \geq P_{\text{out}}$, so that

$$\mathbf{A}^{\dagger}(\mathbf{I} - |\mathbf{S}|^2)\mathbf{A} \geq 0 \tag{D.3}$$

for any $\mathbf{A}$. For passive component, the matrix $\mathbf{I} - |\mathbf{S}|^2$ is semipositive. Component for which the power is conserved ($P_{\text{in}} = P_{\text{out}}$), $\mathbf{S}$-matrix is unitary:

$$|\mathbf{S}|^2 = \mathbf{I}. \tag{D.4}$$

Power loss can occur as result of absorption,scattering, and coupling to radiation modes. Under normal conditions, optical components may be considered as a reciprocal and are characterized by the symmetric $\mathbf{S}$-matrix:

$$\mathbf{S} = \mathbf{S}^{\mathrm{T}}. \tag{D.5}$$

D.2 Calculation of S-matrix for FBG

In FBG, the forward, $\mathbf{d}(z)$, and backward, $\mathbf{u}(z)$, propagating waves obeys the coupled differential equations (as derived in Appendix C):

$$\begin{aligned} \frac{\partial}{\partial z}\mathbf{d}(z) &= \boldsymbol{\kappa}(z)^* e^{\jmath(2k-k_g)z}\mathbf{u}(z) \\ \frac{\partial}{\partial z}\mathbf{u}(z) &= \boldsymbol{\kappa}(z) e^{-\jmath(2k-k_g)z}\mathbf{d}(z) \end{aligned} \tag{D.6}$$

Fiber Bragg Grating is a reciprocal ($S_{11} = S_{22}$ and $S_{12} = S_{21}$) and lossless optical network, and therefore characterized by the scattering matrix:

$$\mathbf{S} = \begin{bmatrix} S_{11} & S_{12} \\ S_{21} & S_{22} \end{bmatrix}. \tag{D.7}$$

For the Bragg grating of length L, i.e. $0 \leq z \leq L$ one can write:

$$\begin{bmatrix} \mathbf{u}(0) \\ \mathbf{d}(L) \end{bmatrix} = \mathbf{S} \begin{bmatrix} d(0) \\ u(L) \end{bmatrix} = \begin{bmatrix} S_{11} & S_{12} \\ S_{21} & S_{22} \end{bmatrix} \begin{bmatrix} \mathbf{d}(0) \\ \mathbf{u}(L) \end{bmatrix} \tag{D.8}$$

Now one needs to solve the above coupled differential equations given in (D:6) with appropriate boundary conditions in order to calculate individual elements of the scattering matrix $\mathbf{S}$. The exponential term in above coupled differential equations

$$2k - k_g = 0, \tag{D.9}$$

if the forward, $\mathbf{d}$, and backward, $\mathbf{u}$, propagating waves are phase matched. This condition is called the longitudinal phase matching. This condition is a spatial analogue of conservation of energy in time-dependent perturbation theory and therefore, may be called as conservation of momentum. This is a special case of resonant coupling. For significant mode coupling to takes place between the forward and backward propagating modes, two conditions must be satisfied. The first is kinematical condition expressed by (D:9). Second, the coupling coefficient $\kappa(z)$ in (D:6) must not vanish. The later is also called as dynamical condition, since it depends upon the characteristics of the waves such as polarization and mode profiles, etc. The term ($k - k_g/2 = \Delta\beta$) and it represents the detuning factor which is proportional to difference between the incident frequency and resonant frequency. Theoretically $\Delta\beta$ is defined in same units as that of κ. The coupled mode equations becomes

$$\begin{aligned} \frac{\partial}{\partial z}\mathbf{d}(z) &= \boldsymbol{\kappa}(z)^* e^{\jmath 2(\Delta\beta)z}\mathbf{u}(z) \\ \frac{\partial}{\partial z}\mathbf{u}(z) &= \boldsymbol{\kappa}(z) e^{-\jmath 2(\Delta\beta)z}\mathbf{d}(z). \end{aligned} \tag{D.10}$$

Since the coupling coefficient κ is complex, the sign of the right hand side of both the coupled differential equations is different and is very important. This sign will determine the behavior of the coupling. These signs, of course, depends on the direction of propagation of the coupled modes. The coupling is therefore divided into two categories: codirectional and contradirectional. In FBG, as the coupled modes travels in opposite direction, we are dealing with the contradirectional coupling. Boundary conditions that are used to solve the contradirectional coupled mode equations are $\mathbf{d}(0) = 1$ at $z = 0$ and $\mathbf{u}(L) = 0$ at $z = L$. The net power flow in $+z$ direction for this case is $|\mathbf{d}|^2 - |\mathbf{u}|^2$. The coupled mode equations are again consistent with the conservation of energy, which requires that

$$\frac{\partial}{\partial z}(|\mathbf{d}|^2 - |\mathbf{u}|^2) = 0. \tag{D.11}$$

The field amplitudes are say constants, D for the forward and U for the backward propagating waves and therefore, one can write:

$$\begin{aligned} \mathbf{d}(z) &= D{\cdot}e^{(s+\jmath\Delta\beta)z} \\ \mathbf{u}(z) &= U{\cdot}e^{(s-\jmath\Delta\beta)z}. \end{aligned} \tag{D.12}$$

Differentiating above with respect to 1-D space coordinate z, we get

$$\begin{aligned} \frac{\partial}{\partial z}\mathbf{d}(z) &= \frac{\partial}{\partial z}D{\cdot}e^{(s+\jmath\Delta\beta)z} = (s+\jmath\Delta\beta){\cdot}e^{(s+\jmath\Delta\beta)z} = \kappa^* U{\cdot}e^{(s-\jmath\Delta\beta)z}e^{\jmath 2(\Delta\beta)z} \\ \frac{\partial}{\partial z}\mathbf{u}(z) &= \frac{\partial}{\partial z}U{\cdot}e^{(s-\jmath\Delta\beta)z} = (s-\jmath\Delta\beta)U{\cdot}e^{(s-\jmath\Delta\beta)z} = \kappa D{\cdot}e^{(s+\jmath\Delta\beta)z}e^{-\jmath 2(\Delta\beta)z} \end{aligned} \tag{D.13}$$

Multiplication of these two equations in (D:13) and its simplification gives:

$$\begin{aligned} s^2 &= |\kappa|^2 - (\Delta\beta)^2 \\ s &= \pm\sqrt{|\kappa|^2 - (\Delta\beta)^2}. \end{aligned} \tag{D.14}$$

Both the equations in (D:13) together yields:

$$D = \frac{\kappa^*}{(s + \jmath\Delta\beta)} U \Leftrightarrow U = \frac{\kappa}{(s - \jmath\Delta\beta)} D. \tag{D.15}$$

Therefore, we can write $\mathbf{d}(z)$ and $\mathbf{u}(z)$ in terms of a single constant D as

$$\begin{aligned} \mathbf{d}(z) &= D{\cdot}e^{(s+\jmath\Delta\beta)z} \\ \mathbf{u}(z) &= \frac{\kappa}{(s - \jmath\Delta\beta)} D{\cdot}e^{(s-\jmath\Delta\beta)z}. \end{aligned} \tag{D.16}$$

The common solution of these two first order coupled differential equation contains two constants corresponding to s and $-s$, therefore, we can write,

$$\begin{aligned} \mathbf{d}(z) &= D_1{\cdot}e^{(s+\jmath\Delta\beta)z} + D_2{\cdot}e^{(-s+\jmath\Delta\beta)z} \\ \mathbf{u}(z) &= \frac{\kappa}{(s - \jmath\Delta\beta)} D_1{\cdot}e^{(s-\jmath\Delta\beta)z} + \frac{\kappa}{(-s - \jmath\Delta\beta)} D_2{\cdot}e^{(-s-\jmath\Delta\beta)z}. \end{aligned} \tag{D.17}$$

Once the constants D_1 and D_2 are calculated, one can immediately calculate the elements of the scattering matrix $\mathbf{S}$ for the FBG. As the grating physically exists between $z = 0$ and $z = L$, we can apply these boundary conditions to (D:17) to get

$$\begin{aligned} \mathbf{d}(0) &= D_1 + D_2 \\ \mathbf{u}(0) &= \frac{\kappa}{(s - \jmath\Delta\beta)} D_1 + \frac{\kappa}{(-s - \jmath\Delta\beta)} D_2 \\ \mathbf{d}(L) &= D_1{\cdot}e^{(s+\jmath\Delta\beta)L} + D_2{\cdot}e^{(-s+\jmath\Delta\beta)L} \\ \mathbf{u}(L) &= \frac{\kappa}{(s - \jmath\Delta\beta)} D_1{\cdot}e^{(s-\jmath\Delta\beta)L} + \frac{\kappa}{(-s - \jmath\Delta\beta)} D_2{\cdot}e^{(-s-\jmath\Delta\beta)L}. \end{aligned} \tag{D.18}$$

Expression for $\mathbf{d}(0)$ and $\mathbf{u}(L)$ forms the simultaneous equations. These are solved simultaneously to obtain the unknown constants:

$$\begin{aligned} D_1 &= \frac{[\frac{\kappa}{(-s-\jmath\Delta\beta)} e^{(-s-\jmath\Delta\beta)L}] d(0) - u(L)}{\frac{\kappa}{(-s-\jmath\Delta\beta)} e^{(-s-\jmath\Delta\beta)L} - \frac{\kappa}{(s-\jmath\Delta\beta)} e^{(s-\jmath\Delta\beta)L}} \\ D_2 &= \frac{-[\frac{\kappa}{(s-\jmath\Delta\beta)} e^{(s-\jmath\Delta\beta)L}] d(0) + u(L)}{\frac{\kappa}{(-s-\jmath\Delta\beta)} e^{(-s-\jmath\Delta\beta)L} - \frac{\kappa}{(s-\jmath\Delta\beta)} e^{(s-\jmath\Delta\beta)L}}. \end{aligned} \tag{D.19}$$

These recently calculated constants D_1 and D_2 in (D:19) are substituted into the expressions for $\mathbf{u}(0)$ and $\mathbf{d}(L)$. After simplification, we directly get the $\mathbf{S}$-matrix (D:20) for the

FBG.

$$\begin{bmatrix}\mathbf{u}(0)\\ \mathbf{d}(L)\end{bmatrix}=\mathbf{S}\begin{bmatrix}\mathbf{d}(0)\\ \mathbf{u}(L)\end{bmatrix}=\frac{\begin{bmatrix}-\kappa\sinh(sL)e^{-\jmath(\Delta\beta)L} & s\\ s & \kappa^*\sinh(sL)e^{\jmath(\Delta\beta)L}\end{bmatrix}}{(s\cosh(sL)+\jmath\Delta\beta\sinh(sL)e^{-\jmath(\Delta\beta)L}}\begin{bmatrix}\mathbf{d}(0)\\ \mathbf{u}(L)\end{bmatrix} \tag{D.20}$$

If the term $\Delta\beta = 0$ then $s = \pm\kappa = |\kappa|$ and therefore we can write

$$\begin{bmatrix}\mathbf{u}(0)\\ \mathbf{d}(L)\end{bmatrix} = \begin{bmatrix}\frac{-\kappa}{|\kappa|}\tanh(|\kappa|L) & \frac{1}{\cosh(|\kappa|L)}\\ \frac{1}{\cosh(|\kappa|L)} & \frac{\kappa^*}{|\kappa|}\tanh(|\kappa|L)\end{bmatrix}\begin{bmatrix}\mathbf{d}(0)\\ \mathbf{u}(L)\end{bmatrix}. \tag{D.21}$$

We experimentally measured the local reflectivity and hence locally constant κ's at discrete points, n, as a function of 1-D space coordinate z over the whole grating length $L\ (=\mu\Delta z)$ and $\mu = n$. As the increment Δz in z approaches 0, the limit of above scattering matrix $\mathbf{S}$ as $\Delta z\rightarrow 0$ reduces it to

$$\mathbf{S}_\mu = \lim_{\Delta z\rightarrow 0}\mathbf{S} \quad \text{with} \quad \kappa(\mu\Delta z)\Delta z = \kappa_\mu = \text{constant}, \quad \text{and} \tag{D.22}$$

$$\mathbf{S}_\mu = \begin{bmatrix}\frac{-\kappa_\mu}{|\kappa_\mu|}\tanh(|\kappa_\mu|) & \frac{1}{\cosh(|\kappa_\mu|)}\\ \frac{1}{\cosh(|\kappa_\mu|)} & \frac{\kappa_\mu^*}{|\kappa_\mu|}\tanh(|\kappa_\mu|)\end{bmatrix}. \tag{D.23}$$

The local reflectivity ρ_μ equals

$$\rho_\mu = \frac{\kappa_\mu}{|\kappa_\mu|}\tanh(|\kappa_\mu|) \simeq |\kappa_\mu|, \tag{D.24}$$

and the local transmission coefficient τ_μ equals

$$\tau_\mu = \frac{1}{\cosh(|\kappa_\mu|)} = \sqrt{1-\tanh^2(|\kappa_\mu|)} = \sqrt{1-|\kappa_\mu|^2}. \tag{D.25}$$

Therefore, now we can write the locally constant scattering matrix $\mathbf{S}_\mu$ in a simplified form as

$$\mathbf{S}_\mu = \begin{bmatrix}-\kappa_\mu & \tau_\mu\\ \tau_\mu & \kappa_\mu^*\end{bmatrix}. \tag{D.26}$$

From this we can see that the power exchange between the forward and backward propagating modes in the region between the $z = 0$ and $z = L$ where the Bragg grating physically exists is given by

$$\frac{|\kappa|^2\sinh^2(sL)}{s^2\cosh^2(sL)+(\jmath\Delta\beta)^2\sinh^2(sL)}. \tag{D.27}$$

We notice that the fractional power exchange decreases as $\Delta\beta$ increases. A complete power exchange for contradirectional coupling, however, only occurs when the phase matching condition is satisfied ($\Delta\beta = 0$) and L is infinite. This situation is different from that of codirectional coupling, where the complete power is periodically exchanged (back and forth) between the coupled modes as a function of 1-D space coordinate z provided $\Delta\beta = 0$. Fiber Bragg grating is a typical example of contradirectional coupling.

D.3 Down–Up Difference Schemes

Instead of constructing difference schemes in terms of input Dirac impulse unity matrix and the output impulse response matrix, we will use the down and up combinations of propagating waves.

For example, the medium in which the wave travels is specified by a single system parameter, the impedance, Z, as function of 1-D space coordinate z. These waves has a property that they do not interact unless Z changes it's value. $\mathbf{D}(z,\, t)$ and $\mathbf{U}(z,\, t)$ waves are only discontinuous at $z = \mu\Delta z$ where there exists a discontinuity in Z, otherwise they are continuous.

Suppose that $Z(z)$ is piecewise constant, with possible discontinuities only at Δz, $2\Delta z$, $\cdots$ $\mu\Delta z$ etc. Thus, we have,

$$Z(z) = Z_\mu \quad z \in [\mu\Delta,\, (\mu+1)\Delta]. \tag{D.28}$$

Therefore, we need to analyze the waves into two situations:
1. as they travel along a part where $Z = \text{constant}$;
2. as they cross the discontinuity in Z.

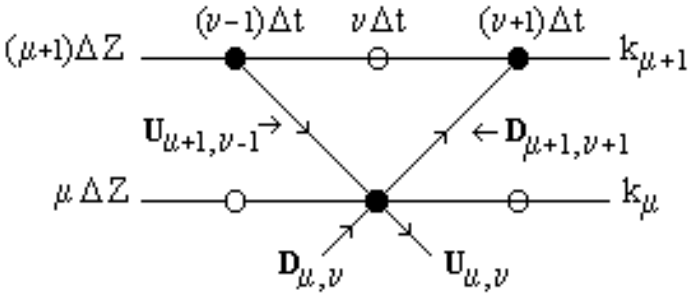

Figure D.1: Calculation of $\mathbf{D}_{\mu,\,\nu}$ and $\mathbf{U}_{\mu,\,\nu}$ for one position step ΔZ

Figure D.1 shows the quantities required to calculate the $\mathbf{D}$ and $\mathbf{U}$ waves for one position step Δz. Suppose $z \in [\mu\Delta,\, (\mu+1)\Delta]$, then $Z = \text{constant}$ and the waves are separated into down-wave (right moving) and up-wave (left moving) and are defined as

$$\begin{aligned} \mathbf{D}(z,\, t) &= f(z-t), \\ \mathbf{U}(z,\, t) &= g(z-t). \end{aligned} \tag{D.29}$$

Figure D.2 shows the down and up waves, $\mathbf{D}$ and $\mathbf{U}$, in a piecewise constant portion of the medium.

Above equations states that down-wave just to the left of the discontinuity at $(\mu+1)\Delta z$ at any given time t must have departed from $\mu\Delta z$ at the instant $t - \Delta$. Since the wave travels without any change of shape, we can write

$$\mathbf{D}[(\mu+1)\Delta z-,\, t] = \mathbf{D}[\mu\Delta z+,\, t-\Delta]. \tag{D.30}$$

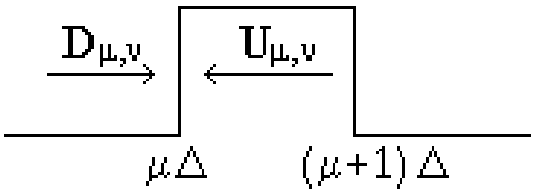

Figure D.2: $\mathbf{D}$ and $\mathbf{U}$ waves in a piecewise constant portion of the medium

This wave on the right hand side of above equation is obtained from the left hand side wave by just operating on it by a delay operator Δ and this Δ has a property such that

$$\Delta f(t) = f(t - \Delta), \tag{D.31}$$

so that we can write equation (D:30) as

$$\mathbf{D}[(\mu + 1)\Delta z-,\, t] = \Delta \mathbf{D}[\mu \Delta z+,\, t]. \tag{D.32}$$

We can also say that the up-wave at $\mu\Delta z+$ and time t must be that which departed from $(\mu + 1)\Delta z-$ at time $t - \Delta$. Thus we can write

$$\mathbf{U}[\mu\Delta z+,\, t] = \mathbf{U}[(\mu + 1)\Delta z-,\, t - \Delta] = \Delta \mathbf{U}[(\mu + 1)\Delta z-,\, t], \tag{D.33}$$

which we may invert it to give,

$$\mathbf{U}[(\mu + 1)\Delta z-,\, t] = \Delta^{-1}\mathbf{U}[\mu\Delta z+,\, t]. \tag{D.34}$$

The last equation must be used with care since it expresses $\mathbf{U}[(\mu + 1)\Delta z-,\, t]$ in terms of $\mathbf{U}[\mu\Delta z+,\, t + \Delta]$, i.e. in terms of an event in the future. It is a non-casual relation and therefore we will work with the previous version of it. We can combine these two equations into one matrix equation

$$\begin{bmatrix} \mathbf{D}[(\mu + 1)\Delta z-,\, t] \\ \mathbf{U}[(\mu + 1)\Delta z-,\, t] \end{bmatrix} = \begin{bmatrix} \Delta & \\ & \Delta^{-1} \end{bmatrix} \begin{bmatrix} \mathbf{D}[\mu\Delta z+,\, t] \\ \mathbf{U}[\mu\Delta z+,\, t] \end{bmatrix}. \tag{D.35}$$

This is the first of two equations that well describes the evolution of waves. It expresses the fact that $\mathbf{D}$, $\mathbf{U}$ wave travel without any change of shape in the parts of the medium where Z is constant. The second evolution equation for $\mathbf{D}$, $\mathbf{U}$ to accompany (D:35), describes how these waves interact as they pass through the discontinuity between Z_μ and $Z_{\mu+1}$ at $(\mu + 1)\Delta z$.

$$\begin{bmatrix} \mathbf{D}[(\mu + 1)\Delta z+,\, t] \\ \mathbf{U}[(\mu + 1)\Delta z+,\, t] \end{bmatrix} = \mathbf{\Theta}_\mu \begin{bmatrix} \mathbf{D}[(\mu + 1)\Delta z-,\, t] \\ \mathbf{U}[(\mu + 1)\Delta z-,\, t] \end{bmatrix}. \tag{D.36}$$

where $\mathbf{\Theta}_\mu$ is given

$$\mathbf{\Theta}_\mu = \frac{Z_\mu + Z_{\mu+1}}{2\sqrt{Z_\mu}\sqrt{Z_{\mu+1}}} \begin{bmatrix} 1 & -\frac{(Z_\mu - Z_{\mu+1})}{(Z_\mu + Z_{\mu+1})} \\ -\frac{(Z_\mu - Z_{\mu+1})}{(Z_\mu + Z_{\mu+1})} & 1 \end{bmatrix}. \tag{D.37}$$

If we define μth local reflection and transmission coefficient as

$$\begin{aligned} \kappa_\mu &= \frac{(Z_\mu - Z_{\mu+1})}{(Z_\mu + Z_{\mu+1})} \\ \tau_\mu &= \frac{Z_\mu + Z_{\mu+1}}{2\sqrt{Z_\mu}\sqrt{Z_{\mu+1}}}, \end{aligned} \tag{D.38}$$

then the matrix $\mathbf{\Theta}_\mu$ becomes

$$\mathbf{\Theta}_\mu = \frac{1}{\tau_\mu} \begin{bmatrix} 1 & -\kappa_\mu \\ -\kappa_\mu & 1 \end{bmatrix}. \tag{D.39}$$

The matrix $\mathbf{\Theta}_\mu$, which describes how the $\mathbf{D}$, $\mathbf{U}$ waves interact as they cross the discontinuity, is called a scattering matrix. The pair of equations (D:35) and (D:36) completely describes the evolution of the waves $\mathbf{D}$ and $\mathbf{U}$. They may be combined into one equation

$$\begin{bmatrix} \mathbf{D}[(\mu+1)\Delta z+,\, t] \\ \mathbf{U}[(\mu+1)\Delta z+,\, t] \end{bmatrix} = \mathbf{\Theta}_\mu \begin{bmatrix} \Delta & \\ & \Delta^{-1} \end{bmatrix} \begin{bmatrix} \mathbf{D}[\mu\Delta z+,\, t] \\ \mathbf{U}[\mu\Delta z+,\, t] \end{bmatrix}. \tag{D.40}$$

Equation (D:40) is easy to use; it expresses the quantities at one discontinuity in terms of those at the previous one (in space). This means that we can obtain quantities at $(\mu + 1)\Delta(z+)$ in terms of quantities at $0+$ simply by multiplying the appropriate operators:

$$\begin{bmatrix} \mathbf{D}[(\mu+1)\Delta z+,\, t] \\ \mathbf{U}[(\mu+1)\Delta z+,\, t] \end{bmatrix} = \mathbf{\Theta}_\mu \begin{bmatrix} \Delta & \\ & \Delta^{-1} \end{bmatrix} \cdots \mathbf{\Theta}_1 \begin{bmatrix} \Delta & \\ & \Delta^{-1} \end{bmatrix} \begin{bmatrix} \mathbf{D}[0+,\, t] \\ \mathbf{U}[0+,\, t] \end{bmatrix}. \tag{D.41}$$

We can call such a composition rule as a natural cascade rule. Second line of (D:40) is a non-casual relation because it expresses $\mathbf{U}[\mu\Delta z-,\, t]$ in terms of $\mathbf{U}[(\mu-1)\Delta z+,\, t+\Delta]$, i.e. in terms of a quantity in future. In order to obtain a casual relationship, we need to rearrange it as follows. We use $t = \nu\Delta$ in (D:40) and drop the suffixes $\Delta z+$ and Δt and rewrite (D:40) as

$$\begin{bmatrix} \mathbf{D}_{\mu+1,\,\nu} \\ \mathbf{U}_{\mu+1,\,\nu} \end{bmatrix} = \mathbf{\Theta}_\mu \begin{bmatrix} \Delta & \\ & \Delta^{-1} \end{bmatrix} \begin{bmatrix} \mathbf{D}_{\mu,\,\nu} \\ \mathbf{U}_{\mu,\,\nu} \end{bmatrix}. \tag{D.42}$$

In full this equation is

$$\begin{aligned} \mathbf{D}_{\mu+1,\,\nu} &= \tau_\mu^{-1}(\Delta\mathbf{D}_{\mu,\,\nu} - \Delta^{-1}\kappa_\mu\mathbf{U}_{\mu,\,\nu}) \\ \mathbf{U}_{\mu+1,\,\nu} &= \tau_\mu^{-1}(-\Delta\kappa_\mu\mathbf{D}_{\mu,\,\nu} + \Delta^{-1}\mathbf{U}_{\mu,\,\nu}) \end{aligned} \tag{D.43}$$

Eliminating $\Delta^{-1}\mathbf{U}_{\mu,\,\nu}$ from (D:40), we get one casual relation as

$$\mathbf{D}_{\mu+1,\,\nu} = \Delta\tau_\mu\mathbf{D}_{\mu,\,\nu} - \kappa_\mu\mathbf{U}_{\mu+1,\,\nu}. \tag{D.44}$$

Similarly solving (D:40) simultaneously for $\Delta^{-1}\mathbf{U}_{\mu,\nu}$, we get second casual relations as

$$\mathbf{U}_{\mu,\nu} = \Delta^2\kappa_\mu\mathbf{D}_{\mu,\nu} + \Delta\tau_\mu\mathbf{U}_{\mu+1,\nu}. \tag{D.45}$$

Equations (D:44) and (D:45) can be written into the matrix form as

$$\begin{bmatrix} \mathbf{D}_{\mu+1,\nu} \\ \mathbf{U}_{\mu,\nu} \end{bmatrix} = \begin{bmatrix} \Delta\tau_\mu & -\kappa_\mu \\ \Delta^2\kappa_\mu & \Delta\tau_\mu \end{bmatrix} \begin{bmatrix} \mathbf{D}_{\mu,\nu} \\ \mathbf{U}_{\mu+1,\nu} \end{bmatrix}. \tag{D.46}$$

The matrix operator in (D:46) may be factorized in the form

$$\begin{bmatrix} \Delta\tau_\mu & -\kappa_\mu \\ \Delta^2\kappa_\mu & \Delta\tau_\mu \end{bmatrix} = \begin{bmatrix} 1 & \\ & \Delta \end{bmatrix} \begin{bmatrix} \tau_\mu & -\kappa_\mu \\ \kappa_\mu & \tau_\mu \end{bmatrix} \begin{bmatrix} \Delta & \\ & 1 \end{bmatrix} \tag{D.47}$$

Therefore we can rewrite (D:46) as

$$\begin{bmatrix} \mathbf{D}_{\mu+1,\nu} \\ \mathbf{U}_{\mu,\nu} \end{bmatrix} = \begin{bmatrix} 1 & \\ & \Delta \end{bmatrix} \begin{bmatrix} \tau_\mu & -\kappa_\mu \\ \kappa_\mu & \tau_\mu \end{bmatrix} \begin{bmatrix} \Delta & \\ & 1 \end{bmatrix} \begin{bmatrix} \mathbf{D}_{\mu,\nu} \\ \mathbf{U}_{\mu+1,\nu} \end{bmatrix}. \tag{D.48}$$

This equation (D:48) fits our intuition. The $\mathbf{D}$ wave moves down so that it will reach $(\mu+1)\Delta z+$ after $\mu\Delta z+$; the $\mathbf{U}$ waves moving up so that it reaches $(\mu+1)\Delta z+$ before $\mu\Delta z+$. Multiply (D:48) on left by the matrix operator

$$\begin{bmatrix} \Delta & \\ & 1 \end{bmatrix}^{-1} = \begin{bmatrix} \Delta^{-1} & \\ & 1 \end{bmatrix} \tag{D.49}$$

to obtain

$$\begin{bmatrix} \Delta^{-1} & \\ & 1 \end{bmatrix} \begin{bmatrix} \mathbf{D}_{\mu+1,\nu} \\ \mathbf{U}_{\mu,\nu} \end{bmatrix} = \begin{bmatrix} 1 & \\ & \Delta \end{bmatrix} \begin{bmatrix} \tau_\mu & -\kappa_\mu \\ \kappa_\mu & \tau_\mu \end{bmatrix} \begin{bmatrix} \mathbf{D}_{\mu,\nu} \\ \mathbf{U}_{\mu+1,\nu} \end{bmatrix}. \tag{D.50}$$

Carrying out the matrix operator multiplication in (D:50) and is rearranged to get

$$\begin{bmatrix} \mathbf{U}_{\mu,\nu} \\ \mathbf{D}_{\mu+1,\nu+1} \end{bmatrix} = \begin{bmatrix} -\kappa_\mu & \tau_\mu \\ \tau_\mu & \kappa_\mu \end{bmatrix} \begin{bmatrix} \mathbf{D}_{\mu,\nu} \\ \mathbf{U}_{\mu+1,\nu-1} \end{bmatrix} = \mathbf{S}_\mu \begin{bmatrix} \mathbf{D}_{\mu,\nu} \\ \mathbf{U}_{\mu+1,\nu-1} \end{bmatrix}. \tag{D.51}$$

$\mathbf{S}_\mu$ is a scattering matrix for FBG as derived in (D:20). In full, the final expression for the inverse problem is

$$\begin{aligned} \mathbf{D}_{\mu+1,\nu+1} &= \tau_\mu\mathbf{D}_{\mu,\nu} + \kappa_\mu\mathbf{U}_{\mu+1,\nu-1} \\ \mathbf{U}_{\mu,\nu} &= -\kappa_\mu\mathbf{D}_{\mu,\nu} + \tau_\mu\mathbf{U}_{\mu+1,\nu-1}. \end{aligned} \tag{D.52}$$

Simplification of (D:52) gives $\mathbf{D}_{\mu,\nu}$ and $\mathbf{U}_{\mu,\nu}$ in terms of $\mathbf{D}_{\mu+1,\nu+1}$ and $\mathbf{U}_{\mu+1,\nu-1}$ as

$$\begin{aligned} \mathbf{U}_{\mu,\nu} &= \tau_\mu^{-1}(-\kappa_\mu\mathbf{D}_{\mu+1,\nu+1} + \mathbf{U}_{\mu+1,\nu-1}) \\ \mathbf{D}_{\mu,\nu} &= \tau_\mu^{-1}(\mathbf{D}_{\mu+1,\nu+1} - \kappa_\mu\mathbf{U}_{\mu+1,\nu-1}). \end{aligned} \tag{D.53}$$

(D:54) can be written in matrix form as

$$\begin{bmatrix} \mathbf{U}_{\mu,\nu} \\ \mathbf{D}_{\mu,\nu} \end{bmatrix} = \frac{1}{\tau_\mu} \begin{bmatrix} 1 & -\kappa_\mu \\ -\kappa_\mu & 1 \end{bmatrix} \begin{bmatrix} \mathbf{D}_{\mu+1,\nu+1} \\ \mathbf{U}_{\mu+1,\nu-1} \end{bmatrix}. \tag{D.54}$$

Therefore, we can write for $\mathbf{D}_{\mu+1,\nu+1}$ and $\mathbf{U}_{\mu+1,\nu-1}$ in terms of $\mathbf{D}_{\mu,\nu}$ and $\mathbf{U}_{\mu,\nu}$ as

$$\begin{bmatrix} \mathbf{D}_{\mu+1,\nu+1} \\ \mathbf{U}_{\mu+1,\nu-1} \end{bmatrix} = \frac{1}{\tau_\mu} \begin{bmatrix} 1 & -\kappa_\mu \\ -\kappa_\mu & 1 \end{bmatrix}^{-1} \begin{bmatrix} \mathbf{U}_{\mu,\nu} \\ \mathbf{D}_{\mu,\nu} \end{bmatrix}. \tag{D.55}$$

Simplification of (D:55) with μ and ν replaced by $\mu-1$ by $\nu-1$ in the first row, and μ and ν replaced by $\mu-1$ and by $\nu+1$ in the second row of the matrix equation (D:48) gives the output waves $\mathbf{D}_{\mu,\nu}$ and $\mathbf{U}_{\mu,\nu}$ (D:49) in terms of input waves at $\mathbf{D}_{\mu-1,\nu-1}$ and $\mathbf{U}_{\mu-1,\nu+1}$.

$$\begin{bmatrix} \mathbf{U}_{\mu,\nu} \\ \mathbf{D}_{\mu,\nu} \end{bmatrix} = \frac{1}{\tau_{\mu-1}} \begin{bmatrix} \kappa_{\mu-1} & 1 \\ 1 & \kappa_{\mu-1} \end{bmatrix} \begin{bmatrix} \mathbf{D}_{\mu-1,\nu-1} \\ \mathbf{U}_{\mu-1,\nu+1} \end{bmatrix}. \tag{D.56}$$

Hence we can write the discrete equations from (D:56) and are used as it is to construct the downward continuation down-up algorithm for the solution of inverse scattering problem (3.13) in chapter 3, which enables us to calculate the coupling matrix $\boldsymbol{\kappa}$ as function of 1-D space coordinate z for FBG under test and as well as the whole casual solutions $\mathbf{D}_{\mu,\nu}$ and $\mathbf{U}_{\mu,\nu}$, where it is assumed that the measured impulse response matrix of FBG under test is as an output if the given input is Dirac impulse unity matrix.

$$\begin{aligned} \mathbf{U}_{\mu,\nu} &= \tau_{\mu-1}^{-1}(\kappa_{\mu-1}\mathbf{D}_{\mu-1,\nu-1} + \mathbf{U}_{\mu-1,\nu+1}) \\ \mathbf{D}_{\mu,\nu} &= \tau_{\mu-1}^{-1}(\mathbf{D}_{\mu-1,\nu-1} + \kappa_{\mu-1}^{*}\mathbf{U}_{\mu-1,\nu+1}). \end{aligned} \tag{D.57}$$

References

[1] S. E. Miller, "Integrated Optics: an introduction", *Bell Syst. Tech. J.* **48** (1969), 2059–2068.

[2] Editor: Teodoer Tamir, *"Guided Wave Optoelectronics"*, volume 26 of *Electronics and Photonics Series*, Springer–Verlag, 2 edition, 1990.

[3] Hiroshi Nishihara, Masamitsu Haruna, and Toshiaki Suhara, *"Optical Integrated Circuits"*, Optical and Electro-optical Engineering Series, McGRAW–Hill Inc., 1985.

[4] Suhas Bhandare, "Design, Fabrication, and Characterization of Ion-exchanged Channel Waveguides and its application to 3 dB Optical Power Splitters in BK-7 Glass", M.Phil. Thesis, University of Pune, India, October 1998.

[5] C. Becker, T. Oesselke, J. Pandavenes, R. Ricken, K. Rochhausen, G. Schreiber, W. Sohler, H. Suche, R. Wessel, S. Balsamo, I. Montrosset, and D. Sciancalepore, "Advanced Ti:Er:$LiNbO_3$ Waveguide Lasers" (invited paper), *IEEE J. of Selec. Topics in Quant. Electron.* **6** (2000), 101–113.

[6] Yitzhak Weissman, *"Optical Network Theory"*, Optoelectronics Library, Artec House, Inc., 1992.

[7] K. O. Hill, B. Malo, F. Bilodeau, D. C. Johnson, and J. Albert, "Bragg gratings fabricated in monomode photosensitive optical fiber by UV exposure through phase mask", *Appl. Phys. Lett.* **62** (1993), 1035–1037.

[8] Andreas Othonos and Kyriacos Kalli, *"Fiber Bragg Gratings: Fundamentals and Applications in Telecommunications and Sensing"*, Optoelectronics Library, Artec House, Inc., 1999.

[9] F. Ouellette, P. A. Krug, T. Stephens, G. Dhosi, and B. Eggeleton, "Broadband and WDM dispersion compensation using chirped sampled fiber Bragg gratings", *IEE Electron. Lett.* **31** (1995), 899–901.

[10] K. Sano, T. Kudou, and T. Ozeki, "Simultaneous measurement of group delay time dispersion and polarization mode dispersion", *Proc. 22nd ECOC Oslo, Norway, TuP.09* (September 1996), 253–256.

[11] P. Lambelet, P. Y. Fonjallaz, H .G. Limberger, R. P. Salath, C. Zimmer, and H. H. Gligen, "Bragg grating characterization by optical low coherence reflectometry", *IEEE Photon. Technolog. Lett.* **5** (1993), 565–567.

[12] S. Barcelos, M. N. Zervas, R. I. Lamming, D. N. Payne, L. Reekie, J. A. Tucknott, R. Kashyap, P. F. McKee, F. Sladen, and B. Wojciechowicz, "High Accuracy Dispersion Measurement of Chirped Fiber Gratings", *IEE Electron. Lett.* **31** (1995), 1280–1282.

[13] E. Brinkmeyer, "Simple algorithm for reconstructing fiber gratings from reflectometric data", *Opt. Lett.* **20** (1995), 810–812.

[14] D. Sandel, R. Noé, G. Heise, and B. Borchert, "Optical Network Analysis and Longitudinal Structure Characterization of Fiber Bragg Gratings", *IEEE J. Light Technol.* **16** (1998), 2435–2442.

[15] D. Sandel and R. Noé, "Chirped Fiber Gratings For Optical Dispersion Compensation: How To Improve Their Fabrication Accuracy", *Proc. ECOC Oslo, Norway* (1996), 233–236.

[16] D. Sandel. *"Meβtechinsche Characteriserierung Optische Bragg-Gitter"*. Ph.D. Thesis, Universität Paderborn, Germany, 1997.

[17] S. Bhandare, D. Sandel, R. Noè, R. Ricken, H. Suche, and W. Sohler, "$LiNbO_3$–based Integrated Optical Network Analyzer for Vectorial Structure Characterization of Fiber Bragg Gratings", *Proc. Int. Conf. on Fiber Optics and Photonics Mumbai, India* (2002), 97.

[18] S. Bhandare, D. Sandel, R. Noè, H. Hermann, H. Suche, and W. Sohler, "Measurement of Differential Group Delay Profiles in Fibers and in $LiNbO_3$ Distributed PMD Compensator", *Tech. Digest: Symposium on Optical Fiber Measurements, NIST (Boulder) Colorado, USA* (2002), 209–212.

[19] R. Noé, D. Sandel, M. Yoshhida-Dierolf, S. Hinz, V. Mirvoda, A. Schöpflin, C. Glingener, E. Gottwald, C. Scheerer, G. Fischer, T. Weyrauch, and W. Hasse, "Polarization Mode Dispersion Compensation at 10, 20, and 40 Gb/s with Various Optical Equalizers", *IEEE J. of Light. Technol.* **17** (1999), 1602–1616.

[20] F. Heismann and R. Ulrich, "Integrated-optical single-sideband modulator and phase shifter", *IEEE J. of Quant. Electron.* **QE-18** (1982), 767–771.

[21] D. Sandel and R. Noé, "Proposal of Distributed Polarization Mode Dispersion Compensator in $LiNbO_3$", *Proc. ECIO Torino, Italy* (1999), 237–240.

[22] R. Noé, D. Sandel, S. Hinz, M. Yoshhida-Dierolf, V. Mirvoda, G. Feise, H. Hermann, R. Ricken, W. Sohler, F. Wehrmann, C. Glingener, A. Schöpflin, A. Färbert and G. Fischer, "Integrated Optical $LiNbO_3$ distributed Polarization Mode Dispersion Compensator in 20 Gbit/s transmission system", *IEE Electron. Lett.* **35** (1999), 652–654.

[23] S. Bhandare and R. Noé, "Optimisation of TE–TM Mode Converters on X–Cut, Y–Propagation $LiNbO_3$ used for PMD Compensation", *Proc. ECIO Paderborn, Germany* (2001), 172–174.

[24] S. Bhandare and R. Noé, "Pushing the distributed PMD Compensator Performance towards highest bit rates using lithium–niobate–tantalate or lithium tantalate crystals", *Proc. ECIO Prague, CZ* (2003), 91–94.

[25] S. K. Sheem, "Optical fiber interferometer with [3x3] directional couplers: Analysis", *Appl. Phys. Lett.* **52** (1981), 3865–3872.

[26] R. G. Priest, "Analysis of fiber interferometers utilizing 3x3 fiber couplers", , *IEEE J. Quantum Electron.* **QE-18** (1982), 1601–1603.

[27] E. Gottwald and J. Pietzsch, "Measurement Method for the determination of opical phase shifts in 3x3 fiber couplers", *IEE Electron. Lett.* **24** (1988), 265–266.

[28] J. Pietzsch, "Scattering matrix analysis of 3x3 fiber couplers", *IEEE J. of Light. Technol.* **7** (1989), 303–307.

[29] A. Donaldson, "Candidate materials and technologies for integrated optics: fast and efficient electrooptic modulation" (review article), *J. Appl. Phys. D* **24** (1991), 785–802.

[30] H. P. Chan, S. Y. Cheng, and P. S. Chung, "Low loss wide-angle symmetric Y-branch waveguide", *IEE Electron. Lett.* **32** (1996), 652–654.

[31] Z. Weissman, E. Marom, and A. Hardy, "Very low loss Y-junction power divider", *Opt. Lett.* **15** (1989), 293–295.

[32] H. B. Lin, R. S. Cheng, and W. S. Wang, "Wide angle low loss single mode symmetric Y junctions", *IEEE Photon. Technol. Lett.* **6** (1994), 825–827.

[33] W. Y. Hung, H. P. Chan, and P. S. Chung, "Novel design of wide angle single mode symmetric Y junctions", *IEE Electron. Lett.* **24** (1988), 1184–1185.

[34] T. Rasmussen and A. Bjarklev, "Scaling laws for integrated optics waveguides", *Appl. Opt.* **33** (1994), 3231–3236.

[35] R. Regener and W. Sohler, "Loss in Low–Finesse Ti:$LiNbO_3$ Optical Waveguide Resonators", *J. Appl. Phys. B* **36** (1985), 143–147.

[36] G. Stock, "Realization of Integrated Optical Polarizers for Ti:$LiNbO_3$ With Au, Al AND Ti Metal Cladding", *IEE Electron. Lett.* **24** (1988), 899–901.

[37] K. Thygarajan, A. N. Kaul, and S. I. Hosain, "Attenuation characteristics of single–mode metal–cladd graded–index waveguides with a dielectric buffer: a simple and accurate numarical method", *Opt. Lett.* **11** (1986), 479–481.

[38] J. Čtyroký and H. Henning, "Thin–Film Polarizer for Ti:$LiNbO_3$ Waveguides at $\lambda = 1.3\ \mu m$", *IEE Electron. Lett.* **22** (1986), 756–758.

[39] C. M. Kim and R. V. Ramaswamy, "Overlap Integral Factors in Integrated Optic Modulators and Switches", *IEEE J. of Light. Technol.* **7** (1989), 1063–1070.

[40] D. Marcuse, "Electrostatic Field of Coplanar Lines Computed with the Point Matching Method", *IEEE J. of Quant. Elect.* **25** (1989), 939–947.

[41] M. Haruna, J. Shimada, and H. Nishihara, "Optical wavelength–independent and damage-free polarization controller in $LiNbO_3$", *Technical Digest OFC'86* (1986).

[42] N. G. Walker, G. R. Walker, and J. Davidson, "Endless Polarization Control Using Integrated Optic Lithium Niobate Device", *IEE Electron. Lett.* **24** (1988), 266–268.

[43] N. G. Walker, G. R. Walker, J. Davidson, D. C. Cunningham, A. R. Beaumont, R. C. Booth, "Lithium Niobate Waveguide Polarization Controller", *IEE Electron. Lett.* **24** (1988), 103–104.

[44] F. Heismann and S. Whalen, "Broadband Reset-Free Automatic Polarization Controller", *IEE Electron. Lett.* **27** (1991), 377–379.

[45] S. Thaniyavarn, "Wavelength independent optical damage immune Z–propagation $LiNbO_3$ waveguide polarization converter", *Appl. Phys. Lett.* **47** (1985), 674–677.

[46] S. Thaniyavarn, "Wavelength–independent, optical–damage–immune $LiNbO_3$ TE–TM mode converter", *Opt. Lett.* **11** (1986), 39–41.

[47] A. Donaldson and K. K. Wang, "Phase–Matched Mode Converter in $LiNbO_3$ Using Near–Z–Axis Propagation", *IEE Electron. Lett.* **23** (1987), 1378–1379.

[48] T. Kawazoe, K. Satoh, I. Hayashi, and H. Mori, "Fabrication of Integrated Optic Polarization Controller Using Z–Propagating Ti–$LiNbO_3$ waveguides", *IEEE J. of Light. Technol.* **12** (1992), 51–55.

[49] Jiří Čtyroký, "Analysis of Polarization Effects in Near–Z–Axis Ti:$LiNbO_3$ Devices", *Opt. Comm.* **14** (1993), 32–38.

[50] D. Sandel, S. Bhandare, R. Noé, "Circular Birefringence in X–Cut, Z–Propagation $LiNbO_3$ Polarization Transformer", *Proc. ECIO Paderborn, Germany* (2001), 193–195.

[51] D. Marcusre, "Coupled–Mode Theory for Anisotropic Optical Waveguides", *Bell Syst. Tech. J.* **54** (1975), 985–995.

[52] S. Bhandare, R. Noé, and D. Sandel, "Origin of reciprocal circular birefringence observed in X-cut, Z-propagation LiNbO3 polarization transformers", *J. Appl. Phys. B: Lasers and Optics* **73** (2001), 549-553.

[53] D. K. W. Lam and B. K. Garside, "Characterization of single-mode optical fiber filters", *Appl. Opt.* **20** (1981), 440-444.

[54] G. M. L. Gladwell, *"Inverse Problems in Scattering : An Introduction"*, volume 23 of *Solid mechanics and its applications*, Kluwer Academic Press, 1993.

[55] Editor: H. P. Baltes, *"Inverse Scattering Problems in Optics"*, volume 9 of *Topics in Current Physics*, Springer–Verlag, 1980.

[56] Editor: Eric Udd, *"Fiber Optic Sensors: An Introduction for Engineers and Scientists"*, Wielly Series in Pure and Applied Optics, John Willey & Sons, Inc., 1991.

[57] K. Kråkenes and K. BlØtekær, "Comparision of Fiber-Optic Sagnac and Mach-Zehnder Interferometers with Respect to Thermal Processes in the Fiber", *IEEE J. Light. Technolo.* **13** (1995), 682-686.

[58] Editor: R. Petit, *"Electromagnetic Theory of Gratings"*, volume 22 of *Topics in Current Physics*, Springer–Verlag, 1980.

[59] S. Bhandare, D. Sandel, R. Noè, R. Ricken, H. Suche, and W. Sohler, "A $LiNbO_3$–based Integrated Optical Network Analyzer for Vectorial Structure Characterization of Fiber Bragg Gratings", *IEE Proc.: Circuits, Devices, and Systems* **150** (2003), 490–494.

[60] S. Bhandare and R. Noé, "Optimisation of TE–TM Mode Converters on X–Cut, Y–Propagation $LiNbO_3$ used for PMD Compensation", *J. Appl. Phys. B: Lasers and Optics* **73** (2001), 481–483.

[61] S. K. Sheem, W. K. Burns, and A. F. Miltion, "Leaky-Mode Propagation in Ti-Diffused $LiNbO_3$ and $LiTiO_3$ Waveguides", *Opt. Lett.* **3** (1978), 76–78.

[62] W. K. Burns, S. K. Sheem, and A. F. Milton, "Approximate Analysis of Leaky-Mode Loss Coefficient for Ti-Diffused $LiNbO_3$ Waveguides", *IEEE J. of Quant. Electron.* **QE–5** (1979), 1282–1289.

[63] D. Xue, K. Betzler, and H. Hesse, "Dielectric Properties of Lithium—Niobate—Tantalate Crystals", *Solid State Comm.* **115** (2000), 581–585.

[64] B. L. Heffner, "Aumated Measurement of Polarization Mode Dispersion Using Jones Matrix Eigenanalysis", *IEEE Photon. Technol. Lett.* **4** (1992), 1066–1069.

[65] B. L. Heffner, "Accurate, Automated Measurement of Differential Group Delay Dispersion and Principle State Variation Using Jones Matrix Eigen Analysis", *IEEE Photon. Technol. Lett.* **1993** (5), 814–817.

[66] L. Möller, "Filter Synthesis for Broad-Band PMD Compensation in WDM Systems", *IEEE J. of Photon. Technol. Lett.* **12** (2000), 1258–1260.

[67] S. E. Harris, E. O. Ammann, and I. C. Chang, "Optical Network Synthesis Using Birefringent Crystals and Synthesis of Lossless Networks of Equal–Length Crystals", *J. of Opt. Soc. of America* **54** (1964), 1267–1279.

[68] A. Eyal and A. Yariv, "Design of Broadband PMD Compensation filters", *IEEE J. of Photon. Technol. Lett.* **14** (2002), 1088–1090.

[69] T. Ozeki, "Optical Equalizers", *Opt. Lett.* **17** (1992), 375–377.

[70] L. E. Nelson, R. M. Jopson, and H. Kogelnik, "Müller Matrix Method for Determining Polarization Mode Dispersion Vectors", *ECOC, Nice, France* **II** (1999), 10-11.

[71] D. Sandel, V. Mirvoda, S. Bhandare, F. Wüst, and R. Noè, "Some Enabling Techniques for Polarization Mode Dispersion Compensation", *IEEE J. of Light. Technol.* **21** (2003), 1198–1210.

[72] G. B. Hocker and W. K. Burns, "Mode dispersion in diffused channel waveguides by the effective index method", *Appl. Opt.* **16** (1977), 113–118.

Acknowledgements

First, I would like to sincerely thank my Prof. Reinhold Noè for offering me a golden opportunity to work in his internationally recognized group in an area of optical communication and high-frequency engineering. He constantly gave encouragement during this work. He also gave a freedom to access and use very expensive tools in the optical communication laboratory. He was very much keen on the technical discussions and gave lot of ideas through out the entire course. Without him, it would never have been possible for me to cross this river.

Second, I would like to thank Prof. Wolfgang Sohler for providing me an opportunity to work in his internationally recognized group in an area of lithium niobate-based integrated optics for characterizing, pigtailing and packaging of the integrated optical circuits in lithium niobate and for helpful technical discussions. He also gave me constant encouragement throughout this work.

Third, I would like to thank Dr. Hubertus Suche and Mr. Raimund Ricken who fabricated the integrated optical circuits in lithium niobate and for useful technical discussions.

Fourth, I would like to thank Dr. David Sandel who generously helped me during the entire course and for very useful mathematical and technical discussions. Here, I would like to thank Mr. Schiff, Head, mechanical workshop of electrical engineering for fabricating the required housing and mechanical jigs for pigtailing and packaging of integrated optical circuits in lithium niobate.

Fifth, I would like to thank Mr. Sebastian Hoffman, Dr. Mrs. Mihoko Yoshida–Dierolf, Mr. Vitali Mirvoda, Dr. Frank Wüst, Mr. Stephan Hinz, Mr. S. K. Ibrahim, Mr. A. Hidayat, Mr. A. Fauzi, Mrs. B. Milivojeic, Mr. Gerhard Wieseler , and Mr. Bernd Bartsch from whom I received enormous help as group members.

Sixth, I would like to sincerely thank Dr. A. D. Shaligram, my M.Phil. supervisor and Prof. K. Thyagarajan, IIT Delhi for their constant encouragement and moral support. I would like to thank Dr. Y.G.K. Patro, Program Director, Optoelectronics Division and Dr. K. Chalapathi, Head, Optoelectronics Division of SAMEER, Mumbai for their constant encouragement and moral support. I also would like to thank Dr. B. K. Das who arranged my initial stay and latter as a family friend during his entire stay in Deutschland.

Last but not the least, I would like to appreciate and thank my dear wife Mrs. Kranti and children Mrunmayi and Saumitra for continuous moral support, in spite of the long periods of my physical and mental absence they had to put with. I also would like to thank my parents and my sister Dr. Sunita Bhandare for giving constant moral support throughout the entire stay in Deutschland.

Paderbron, Germany Suhas Bhandare
June 10, 2003